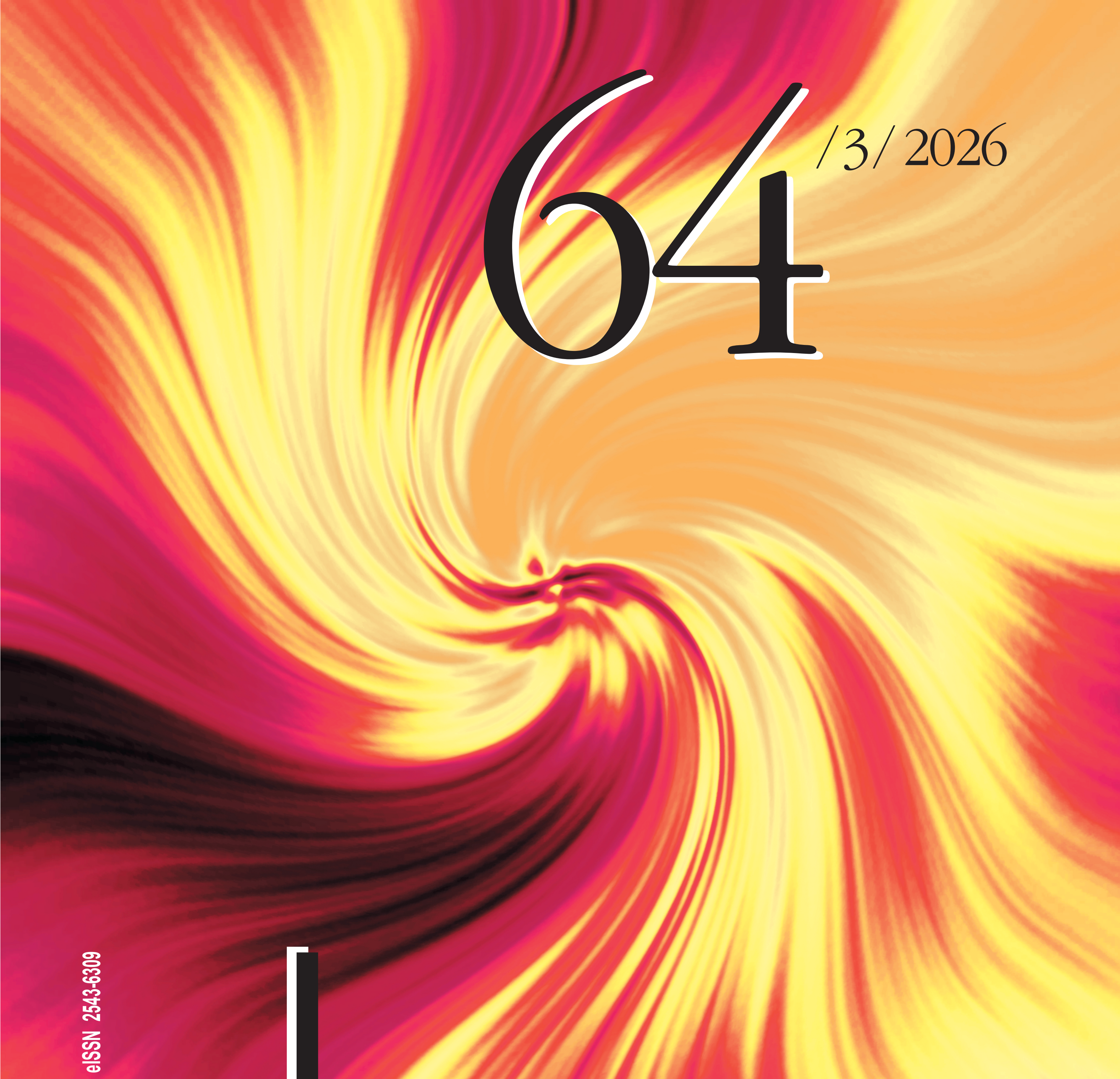

64 /3/ 2026

JOURNAL OF THEORETICAL AND APPLIED MECHANICS

WARSAW 2026, QUARTERLY, VOLUME 64, ISSN 1429-2955 eISSN 2543-6309

POLISH SOCIETY OF THEORETICAL AND APPLIED MECHANICS

POLISH SOCIETY OF THEORETICAL AND APPLIED MECHANICS

JOURNAL OF THEORETICAL AND APPLIED MECHANICS

Vol. 64 • No. 3
Quarterly

WARSAW 2026

JOURNAL OF THEORETICAL AND APPLIED MECHANICS
(until 1997 Mechanika Teoretyczna i Stosowana, ISSN 0079-3701)

Beginning with Vol. 45, No. 1, 2007, *Journal of Theoretical and Applied Mechanics* (JTAM) has been selected for coverage in Thomson Reuters products and custom information services. Now it is indexed and abstracted in the following:

- **Science Citation Index Expanded** (also known as SciSearch®)
- **Journal Citation Reports/Science Edition**

Editorial Office

Al. Armii Ludowej 16, room 650; 00-637 Warsaw, Poland
e-mail: jtam@ptmts.org.pl
www.jtam.pl

The journal content is indexed in Similarity Check, the Crossref initiative to prevent plagiarism.

Ministry of Science and Higher Education
Republic of Poland

WEKTORY NAUKI

This issue has been published with financial support from the Polish Ministry of Science and Higher Education under the "Vectors of Science" programme, project number WNK/SN/0508/2025/01, with project funding of PLN 134,200.00 and total project value of PLN 174,200.00.

JOURNAL OF THEORETICAL
AND APPLIED MECHANICS
64, 3, pp. 185–200, Warsaw 2026
https://doi.org/10.15632/jtam-pl/225472

ANALYTICAL FORMULAE FOR 2D BALLISTIC LIMIT CURVES OVER A RANGE OF MATERIAL THICKNESSES BASED ON THE RECHT–IPSON MODEL AND SYMBOLIC REGRESSION

Tomasz HACHAJ[1], Teresa FRAS[2*]

[1] *Faculty of Electrical Engineering, Automatics, Computer Science and Biomedical Engineering, AGH University, Krakow, Poland*
[2] *French-German Research Institute of Saint-Louis (ISL), Saint-Louis, France*
[*]corresponding author, *teresa.fras@isl.eu*

The study discusses an application of the physics-aware symbolic regression (PASR) paradigm, with the embedded Recht–Ipson (R-I) model, to describe the relationship between the 7.62 mm AP P80 projectile's initial impact and the residual velocities of the S355 steel plates of varying thicknesses. The present approach results in a straightforward analytical "SR R-I" formula, which can be easily applied in engineering practice to determine ballistic limit curves and velocities (BLCs and BLVs). The proposed approach has demonstrated statistical effectiveness that outperforms other machine learning (ML) algorithms in both fitting accuracy and the predictive capability of these terminal ballistic features.

Keywords: terminal ballistics; machine learning; symbolic regression; Recht–Ipson; ballistic limit curves.

1. Introduction

Numerical modelling in terminal ballistics is a well-established approach that has been covered extensively over many decades in numerous papers, books, and surveys (Anderson Jr. & Bodner, 1988; Rosenberg & Dekel, 2012). More recently, machine learning (ML) methods, alongside traditional mathematical modelling using numerical methods – including the finite element method (FEM) – have become an integral part of the researcher's toolkit and engineering practice in materials sciences, particularly in terminal ballistics. ML modelling, especially physics-informed models, (Karniadakis *et al.*, 2021), has been proven successful for predicting high-complexity, high-dimensional problems such as the V50 ballistic limit and the depth of projectile penetration (Rietkerk *et al.*, 2023; Ryan *et al.*, 2024). In (Hachaj & Frąś, 2026), the stochastic physics-based oversampling methods are investigated in order to improve ML-based approximation of 2D ballistic limit curves (BLCs). In that work, we proposed a data-driven ML method to approximate BLCs as functions of material thickness and impact velocity, combining experimental data, finite element simulations, and stochastic physics-based oversampling. A novel oversampling approach is introduced that leverages physical knowledge (via derivatives of fitted ballistic models) to generate more informative training data, thereby improving pre-

Ministry of Science and Higher Education
Republic of Poland
WEKTORY
NAUKI

This publication has been funded by the Polish Ministry of Science and Higher Education under the "Vectors of Science" programme, project number WNK/SN/0508/2025/01, with project funding of PLN 134,200.00 and total project value of PLN 174,200.00.
The content of this article was presented during the 62nd Symposium "Modelowanie w mechanice" (Modelling in Mechanics), Szczyrk, Poland, March 1–4, 2026.

diction accuracy compared to uniform sampling. The results show that deep neural networks trained with this approach can accurately predict both curve shapes and ballistic limit velocities (BLVs) for unseen material thicknesses, reducing the need for costly experiments. ML ballistic modelling for various materials is a relatively new subject of research. It has already been applied to aluminium, titanium, and steel targets (Ryan *et al.*, 2024); initial studies also examine the reverse prediction of impact parameters for 3D woven fabrics subjected to ballistic impact using deep learning methods (Li *et al.*, 2026).

Several studies have applied artificial neural networks (ANNs) to predict residual velocity. Husain *et al.* (2024) used input velocity, shape factor, and target thickness, whereas Deng *et al.* (2025) employed angle, target thickness, and initial velocity. However, neither study evaluated the ability of their models to predict BLV for unknown material thickness, which is among the most important tasks of terminal ballistics.

A major limitation of popular ML approaches, such as neural networks, support vector machines, and classifier and regressor ensembles, is their limited interpretability. In particular, it is often difficult to understand why these models produce specific outputs, how sensitive their predictions are to variations in the training data, and whether their behavior remains stable and consistent across different input conditions. Moreover, these models do not inherently guarantee compliance with known physical laws, which can be critical in scientific and engineering applications. These limitations have driven the rapid development of Explainable Artificial Intelligence (XAI), an important branch of modern machine learning (Dwivedi *et al.*, 2023; Hachaj & Piekarczyk, 2025). The primary objective of XAI is to design models and methodologies whose decision-making processes can be understood, analysed, and trusted by users. This includes providing insights into feature importance, model sensitivity, and the reasoning behind predictions, thereby improving transparency, reliability, and the integration of domain knowledge into data-driven approaches.

Symbolic regression (SR) is a regression algorithm that offers easy-to-interpret results. This technique involves explicit mathematical expressions that best fit a dataset without assuming a predefined model structure. It is often implemented with methods such as genetic programming, which evolve formulas that balance accuracy and simplicity, leading to more intuitive interpretations of the results. SR can also be used to address and interpret terminal ballistic experiments. Levadnyi *et al.* (2024) investigated numerically and experimentally the ballistic performance of thermoplastic polyurethane (TPU)/steel configurations against spherical projectiles and used SR to derive the final equation. Abid *et al.* (2025) and Zou *et al.* (2025) developed an SR-based equation for predicting the depth of penetration for targets under high-velocity projectile impact. Zhang *et al.* (2026) discussed the SR-based impact fracture model. Saifoori *et al.* (2025) linked the impact deformation of elastic-perfectly plastic particles to their material properties and impact velocity using SR.

In this paper, building on our previous work, we propose a method for deriving analytical formulae for 2D BLCs over a range of material thicknesses using SR, enabling the resulting model to be directly interpreted and applied by users. To the best of our knowledge, the application of SR to the problem of 2D limit curves estimation has not yet been published in the literature, and the results we have obtained are pioneering in this field.

2. Problem formulation

The BLC describes the relationship between a projectile's initial velocity and its residual velocity after perforating the target. It is a simplified characterization of both the projectile's penetration capability and the tested material's resistance to ballistic impacts. To approximate the relation between the projectile's velocities and, therefore, to determine the BLC of the impact configuration, the Recht–Ipson (R-I) model is often used (Frąś *et al.*, 2011; Karl *et al.*, 2020; Recht & Ipson, 1963).

$$v_r \approx \text{R-I}(v_i, a, p) = \begin{cases} a \cdot (v_i^p - {v_{bl}}^p)^{1/p} & \text{if} \quad v_i \geq v_{bl}, \\ 0 & \text{if} \quad v_i < v_{bl}, \end{cases} \tag{2.1}$$

where v_i is the initial velocity, v_r is the residual velocity, v_{bl} is the BLV, i.e., the minimum impact velocity required for a projectile to perforate a target (typically determined through impact experiments), parameters a, p are fitted from experimental data by a numeric solver (Deng *et al.*, 2025), for example, non-linear least squares with bounds or the generalized reduced gradient method (Lasdon *et al.*, 1974).

Figure 1a shows the set of BLCs and BLVs obtained experimentally for S355 steel plates with thicknesses of 8 mm and 16 mm. The S355 structural steel is a low-alloy carbon-manganese steel with guaranteed minimum mechanical properties and satisfactory ductility, as shown in Table 1. This steel grade is used in a wide range of construction and structural applications, thanks to its good welding properties and guaranteed strength.

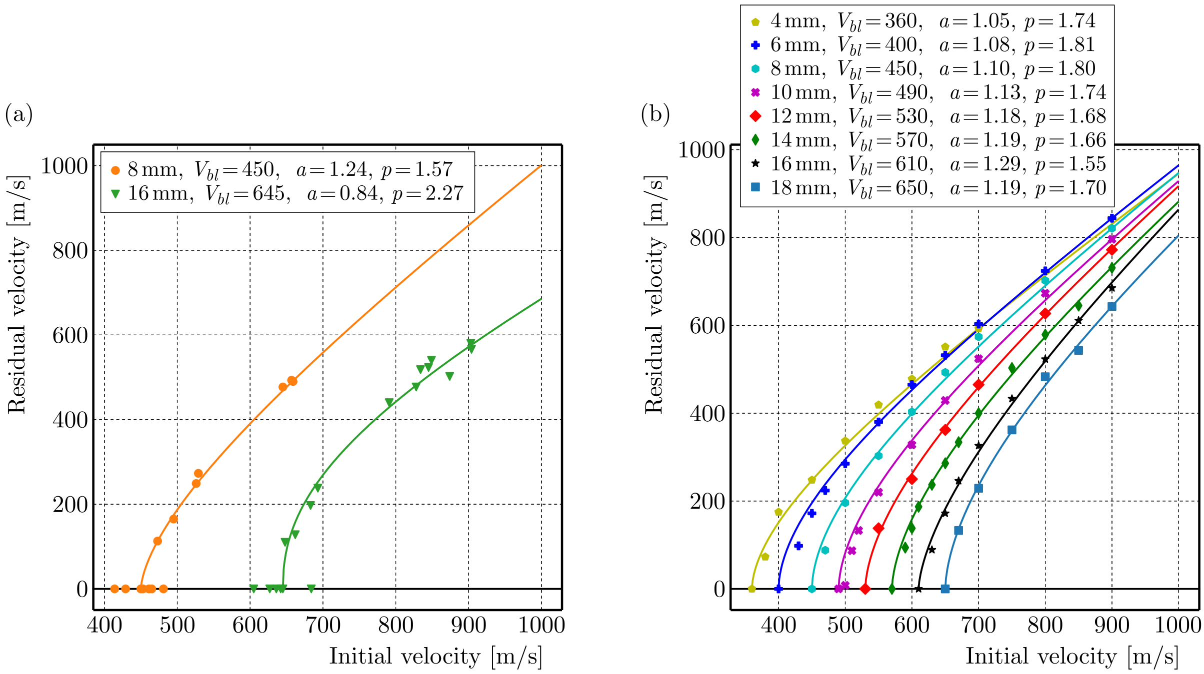

Fig. 1. Our dataset S355 vs. 7.62 mm × 51 mm AP P80 impacts at 0° NATO with BLC fitted to the data: (a) a plot of experimental data; (b) a numeric simulation result. The legends in both plots include parameters of Eq. (2.1).

Table 1. Properties of the S355 structural steel with nominal thickness $t \leq 40$ mm (European Committee for Standardization, 2019).

Property	Value
Density	7850 kg/m^3
Young's modulus	210 GPa
Shear modulus	81 GPa
Poisson's ratio	0.3
Coefficient of linear thermal expansion	12×10^{-6} K^{-1}
Yield strength	355 MPa
Ultimate strength	490 MPa

The S355 steel plates were impacted by 7.62 mm × 51 mm P80 (0.308 Win) armour-piercing rounds. In the cases where the plates were perforated, the projectile cores were not fragmented. The craters left after projectile passage have diameters that closely match the core diameter, i.e., about 5.2 mm to 5.5 mm. Figure 1b presents the numerical approximations of these curves, along with the curves determined numerically for other steel plate thicknesses. The R-I model parameters are shown in the figures. The methodology for establishing the BLCs is detailed in (Hachaj & Frąś, 2026). In the current study, the BLCs' origins and the manner of their numerical representation are not of primary importance. The experimental data were used to fit the numerical experiments, ensuring they reflected the material's actual behaviour. In the legends in both plots, we also list parameters of Eq. (2.1). We have used the standard pyplot library to plot residual velocity against projectile impact velocity, a commonly used approach among researchers (Wei *et al.*, 2024). As a result, many of those plots are very similar in appearance. The parameter-fitting problem was solved using a numerical solver that minimizes the mean-squared error of the residuals from a nonlinear model. When fitting multiple parameters, as in the R-I equation, it is common to obtain solutions with similar errors for different values of the selected parameters. This occurs because the optimization procedure seeks to minimize the error between the observed and predicted values, subject to constraints on the parameter ranges, rather than to ensure the repeatability of the curve parameters, where some of them do not have an individual physical interpretation. In our case, the parameters a and p obtained for the experimental and numerical results have different values, but we did not directly refer to them in the further analysis, taking the R-I equations as the reference, not their individual parameters.

As can be concluded from Fig. 1, the R-I model can be applied only to a single material thickness. Therefore, to obtain BLCs and BLVs over a wider range of target thicknesses, multiple impact experiments must be conducted. As discussed earlier, some studies demonstrate the successful application of ML algorithms to generalize the R-I approximation and to predict data not included in the training dataset. However, there remains a lack of easily interpretable analytical solutions that can be applied directly, without the need for complex software packages that produce results in a black-box manner. In this study, we propose a method for deriving an analytical formula based on the R-I model to describe the performance of S355 steel plates over a wider thickness range under the impact of 7.62 mm AP P80 projectiles.

2.1. Designing optimized formula for SR

Our goal is to obtain an analytic formula for 2D BLCs over a range of material thicknesses, in which residual velocity v_r is a function of input velocity of projectile v_i and material thickness t for a given material. The straightforward approach is to apply SR directly to the dataset and let it fit the training data, imposing constraints on the solution's complexity to prevent overfitting. A major limitation of this approach is that the final solution is likely to be physically inconsistent and very difficult (or even impossible) to interpret using materials science. We will call this unconstrained approach an SR model.

The other approach is to use a physics-aware symbolic regression (PASR) algorithm (El Hasadi & Elghannay, 2026) in which known physics, expressed as symbolic relations, is embedded into the search space. In our case, we want the symbolic solution to have the following form, derived from (2.1):

$$\widehat{v_r}(v_i, t) = \mathscr{a}(t) \cdot \left(v_i^{\mathscr{p}(t)} - v_{\mathscr{bl}}(t)^{\mathscr{p}(t)}\right)^{1/(p(t))}, \qquad v_i \geq v_{\mathscr{bl}}(t), \tag{2.2}$$

where $\mathscr{a}(t)$, $\mathscr{p}(t)$, and $v_{\mathscr{bl}}(t)$ are terms a, b, v_{bl} from the original R-I formula, extended to be functions of material thickness t. By making this assumption, the SR solution will have an intuitive, easy-to-explain form, more closely aligned with known physical models. We will call this algorithm setting an SR R-I model.

In order to find an analytic formula with symbolic regression for both SR and SR R-I in the optimization process, we used a set of binary operators $\circ$ for addition, subtraction, multiplication, division, and exponentiation:

$$x \circ y \in \left\{ x + y,\, x \cdot y,\, x^y,\, \frac{x}{y} \right\}. \tag{2.3}$$

We used unary operators u square, cube, natural logarithm, base-2 logarithm, base-10 logarithm, square root, inverse, and natural logarithm of argument plus one:

$$u(x) = \left\{ x^2, x^3, \ln(x), \log_2(x), \log_{10}(x), \sqrt{x}, \frac{1}{x}, \ln(x+1) \right\}. \tag{2.4}$$

We chose these because they are commonly used operators that allow us to model linear, polynomial, exponential, and logarithmic relationships. Some unary operators can be expressed using binary operators, and some unary operators can be derived from other unary operators; however, to simplify the genetic algorithm's search of the space of potential solutions, we used them directly. We have also added constraints on power values to limit the complexity to 3 (the base of power has no constraint), to avoid overly complex exponential functions. We use the square error loss function. We limited the complexity of the SR solution to 30 terms and the SR R-I to 20 terms. In the SR R-I approach, we provide the genetic algorithm with a significant hint regarding the general form of the final solution. To avoid generating overly complex solutions, we arbitrarily limited the search to 20 terms. In contrast, an SR algorithm without such a preliminary hint would be highly unlikely to find a solution as well-suited to the data as SR R-I when restricted to just 20 terms. Therefore, for this comparison, we set the maximum allowed solution length to 30 terms. Both the base-2 logarithm and the base-10 logarithm can be replaced by the quotient of the corresponding natural logarithms; however, we have deliberately defined these two additional logarithms as base functions in Eq. (2.4). This is due to the fact that the genetic algorithm, which is the main mechanism on which SR is based, "does not know" these formulas for conversion, and changing the logarithm base always requires the use of three operations in the final formula in the solution: division and the addition of the appropriate logarithmic operation in both the numerator and the denominator. This increases the solution's complexity, and since we use the Pareto front, we want the solutions to be as accurate as possible while remaining as simple as possible (with a small number of components). It is also very unlikely that a formula for converting logarithm bases would be found precisely by a genetic algorithm. For this reason, we decided to explicitly define logarithms with three commonly used bases.

We generated a training dataset using stochastic physics-based oversampling with cumulative distribution function (CDF), which is defined with equations (Hachaj & Frąś, 2026):

$$F_{v_i}(y) = P(v_i \le y) = \frac{\displaystyle\int_{b_1}^{y} g(v_i)_{[b_1,b_2]} dv_i}{\displaystyle\int_{b_1}^{b_2} g(v_i)_{[b_1,b_2]} dv_i}, \tag{2.5}$$

$$g(v_i)_{[b_1,b_2]} = c_1 + c_2 \cdot \left| \frac{\partial v_r(v_i)}{\partial v_i} \right| + c_3 \cdot \left| \frac{\partial^2 v_r(v_i)}{\partial v_i^2} \right|, \tag{2.6}$$

where $v_i \in [b_1, b_2] \wedge\ c_1 + c_2 + c_3 = 1 \wedge\ c_1, c_2, c_3 \in [0, 1]$, and $||$ is the absolute value.

In our case $[b_1, b_2] = [v_{bl}(t), 1000]$, which is a relevant range of speeds [m/s] for our dataset. $v_{bl}(t)$ is the BLV for a given material thickness. In both the experiments and the FEM simulations, these values correspond to the minimum impact velocity at which a 7.62 mm P80 projectile perforated the tested targets. Moreover, 100 data points were generated for each thickness to produce a uniquely defined ballistic-limit curve. $[c_1, c_2, c_3] = [0, 0.25, 0.75]$. v_r were previously fitted to experimental and numerical data as explained in Section 2. In Fig. 2, we present four

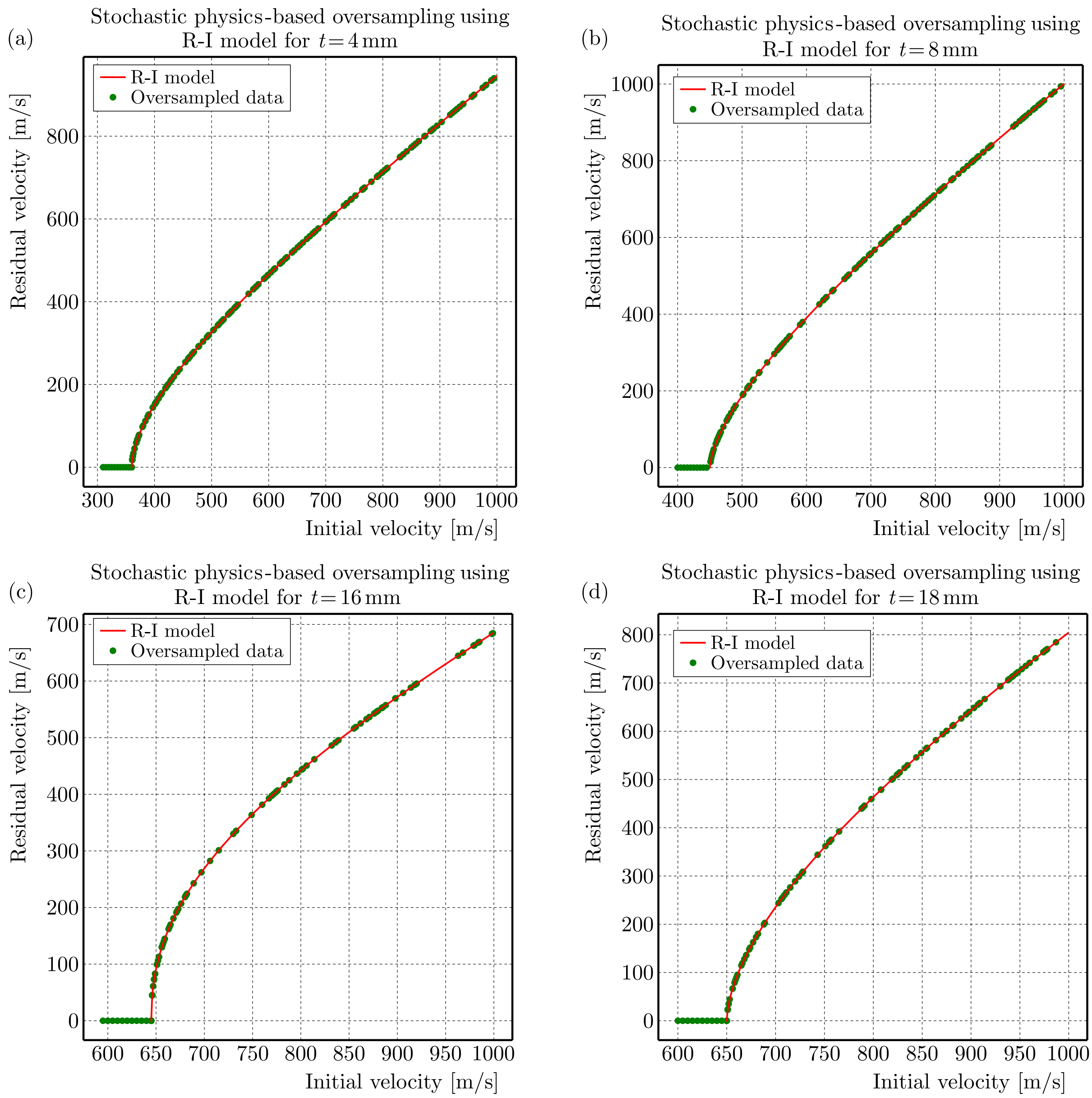

Fig. 2. Four example data series generated according to Eq. (2.5) on our dataset with the setup described in Subsection 2.1. Red line represents the reference R-I model; green points are random samples used during the training of all ML models.

example data series generated according to Eq. (2.5) from our dataset. The validation (test) dataset consists of original data points from experiments and numerical simulations (see Fig. 1). The exact validation procedure will be discussed in Section 3.

2.2. Comparison with other machine learning models

Several other ML models have been successfully used in materials science tasks, particularly for solving ballistic problems. Among them are extreme gradient boosting (XGBoost) and random forest (RF), which were used for predicting the outcome of terminal ballistics events, namely ballistic limit and penetration depth, as mentioned in (Abid *et al.*, 2025; Ryan *et al.*, 2024). Those two models are robust ensemble methods that incorporate many "weak" decision tree regressors. However, they apply different training strategies: XGBoost uses boosting, while RF applies bagging. The main issue with these two methods is the low level of explainability of the resulting models (XAI) due to the large number of decision trees in each model. Since these are state-of-the-art, "out of the box" methods that do not require a complicated setup for tasks of this type, we also trained these models on an oversampled dataset (the same as in the case of SR and SR R-I). We compared the results with those obtained from SRs.

3. Results

To validate our approach, we have implemented the methodology described in Section 2 and executed it on the dataset described in the same section. Implementation was done in Python 3.12. Among the most important packages we used were PySR 1.5.9 (Cranmer, 2023) for SR, scikit-learn 1.8.0 for RF regression, XGBoost 3.2.0 for XGBoost regression, SciPy 1.17.1 for statistical evaluation, and NumPy 2.4.2 for general-purpose algebra. Hyperparameters for all ML methods were determined experimentally, and we will not discuss them here due to paper space limitations. The source code was executed on a PC with an Intel i7-9700 3.00 GHz CPU, 64 GB RAM, an NVIDIA GeForce RTX 2060 6 GB, and Windows OS[1]. The hyperparameters of all the ML methods used are available (see the footnote). The SR training for each leave-one-out case lasts about 10 minutes on our hardware, while RF and XGBoost take about several seconds. We have evaluated SR ("basic" algorithm without assuming constraints on final solution besides those mentioned in Subsection 2.1), SR R-I with constraints on solution represented by Eq. (2.2) (see Subsection 2.1), XGBoost, and RF (see Subsection 2.2).

To evaluate the obtained results, we used the following error functions:

– absolute error:
$$\mathrm{AE}(y_i, \widehat{y_i}) = \left| y_i - \widehat{y_i} \right|, \tag{3.1}$$

– relative error:
$$\mathrm{RE}(y_i, \widehat{y_i}) = \left| \frac{y_i - \widehat{y_i}}{y_i + \epsilon} \right|, \tag{3.2}$$

where ϵ is the small value that prevents division by zero (in our case, condition $y_i \geq 0$ is always true),

– root mean square error:
$$\mathrm{RMSE}(Y, \widehat{Y}) = \sqrt{\frac{1}{n} \sum_{i=1}^{n} (y_i - \widehat{y_i})^2}, \tag{3.3}$$

– mean absolute error:
$$\mathrm{MAE}(Y, \widehat{Y}) = \frac{1}{n} \sum_{i=1}^{n} \left| y_i - \widehat{y_i} \right|, \tag{3.4}$$

– the R^2 score (coefficient of determination):
$$R^2(Y, \widehat{Y}) = 1 - \frac{\sum_{i=1}^{n} (y_i - \widehat{y_i})^2}{\sum_{i=1}^{n} (y_i - \overline{y})^2}, \tag{3.5}$$

– mean relative error:
$$\mathrm{MRE}(Y, \widehat{Y}) = \frac{1}{n} \sum_{i=1}^{n} \left| \frac{y_i - \widehat{y_i}}{y_i + \epsilon} \right|. \tag{3.6}$$

[1]Source codes for our research can be downloaded from https://github.com/browarsoftware/symbolic_ballistic_recht_ipson (accessed March 4, 2026).

We used leave-one-out cross-validation, in which each thickness was used as the training dataset and the remaining thickness as the validation dataset. Due to this, there were 8 folds, for $t \in \{4, 6, 8, 10, 12, 14, 16, 18\}$ mm. For each of these solutions, we have evaluated how well the obtained curves approximate unknown data (generalization ability). The averaged results plus-minus standard deviations are presented in Table 2. For curves, we did not evaluate MRE because the experimental data near BLV had a near-stochastic character, and the relative error results there might be misleading. We have also checked how well the model approximates BLV for unknown data, which is also a generalization ability test. The results are presented in Table 3. Because we only have a single data series (a single BLV estimate for each thickness), the standard deviation is calculated only for MRE.

Table 2. Evaluation results of the models – how well curves approximate unknown data (generalization ability).

Metric	Model			
	SR	SR R-I	RF	XGBoost
RMSE	51.656 ±38.218	52.504 ±47.586	93.856 ±41.229	94.952 ±40.59
MAE	47.071 ±37.509	46.248 ±44.058	82.269 ±43.867	83.264 ±42.965
R^2	0.908 ±0.116	0.894 ±0.176	0.770 ±0.216	0.768 ±0.212

Table 3. Evaluation results of the models – how well the models approximate BLV for unknown data (generalization ability).

Metric	Model			
	SR	SR R-I	RF	XGBoost
MRE	0.043 ±0.055	0.028 ±0.029	0.094 ±0.020	0.08 ±0.034
RMSE	32.697	25.678	50.061	42.702
MAE	20.375	16.641	47.875	39.000
R^2	0.894	0.934	0.751	0.819

To check whether the approximated results differ statistically, we have used a non-parametric Wilcoxon test, which does not assume that the results follow a normal distribution. We have tested whether the distribution of errors for one examined ML method is stochastically less than that of a second ML method. If $p < 0.05$, we have concluded that the error groups differ significantly. Because there is a high variance in the error groups visible in Table 2 and Table 3 that are mainly present in extrapolated curves, to ensure the reliability of the test, we have removed the single largest error value (possible outlier) and the corresponding error value from the other data series used for comparison. For this reason, the set of errors being compared was reduced by one value if the maximum error occurred at the same positions in both series, or by two values if it occurred at different positions. In Table 4, Table 5, Table 6, and Table 7, we present the p-values of the Wilcoxon test for RMSE and MAE (see Table 2) and for RE and AE (see Table 3).

In Fig. 3, we present an approximation of BLCs of all four ML methods trained on all but one thickness from our dataset that predict the shape BLC for the thickness that was not present in the dataset. We chose thicknesses of 8 mm and 16 mm because they predict the experimental data, and 4 mm and 18 mm because, in this setting, they visualize the extrapolation ability of algorithms. Red lines correspond to the reference R-I model curve fitted to data marked as red stars, and green lines are the ML model approximation.

In Fig. 4, we present visualizations of $\widehat{v_r}(v_i, t)$ from Eq. (2.2) as a surface plot. As mentioned, ML methods were trained on all but one thickness in our dataset to predict the shape BLC for

Table 4. p-values of the Wilcoxon test for RMSE (see Table 2). Boldface indicates $p < 0.05$, corresponding to statistically significant differences between the error distributions.

Model 1	Model 2			
	SR	SR R-I	RF	XGBoost
SR	1.000	0.578	**0.039**	**0.039**
SR R-I	0.500	1.000	**0.016**	**0.016**
RF	0.977	1.00	1.000	0.469
XGBoost	0.977	1.000	0.594	1.000

Table 5. p-values of the Wilcoxon test for MAE (see Table 2). Boldface indicates $p < 0.05$, corresponding to statistically significant differences between the error distributions.

Model 1	Model 2			
	SR	SR R-I	RF	XGBoost
SR	1.000	0.578	0.148	0.148
SR R-I	0.500	1.000	**0.016**	**0.016**
RF	0.891	1.000	1.000	0.406
XGBoost	0.891	1.000	0.656	1.000

Table 6. p-values of the Wilcoxon test for RE (see Table 3). Boldface indicates $p < 0.05$, corresponding to statistically significant differences between the error distributions.

Model 1	Model 2			
	SR	SR R-I	RF	XGBoost
SR	1.000	0.781	**0.008**	**0.008**
SR R-I	0.281	1.000	**0.016**	**0.016**
RF	1.000	1.000	1.000	1.000
XGBoost	1.000	1.000	1.000	1.000

Table 7. p-values of the Wilcoxon test for AE (see Table 3). Boldface indicates $p < 0.05$, corresponding to statistically significant differences between the error distributions.

Model 1	Model 2			
	SR	SR R-I	RF	XGBoost
SR	1.000	0.719	**0.031**	**0.031**
SR R-I	0.344	1.000	**0.016**	**0.016**
RF	0.984	1.000	1.000	1.000
XGBoost	0.984	1.000	1.000	1.000

the missing thickness. We have chosen to show the training results for the unknown $t = 8$ mm (experimental data).

SR algorithms return a set of potential solutions rather than a single one. Among them, we have selected the simplest (lowest-complexity) solutions, which, in the case of SR, incorporate both t and v_i with a loss value at most $2 \cdot 10^3$. This loss value was selected empirically. In the case of SR R-I, we have selected the simplest solutions (with lowest complexity), which incorporated t in either $\mathscr{a}(t)$ or $\mathscr{p}(t)$ and obligatorily in $v_{\mathscr{bl}}(t)$ with loss value at most $2 \cdot 10^3$. Further, we present ones that are representative of our data, have the correct (expected) curvature, and minimize the error functions well.

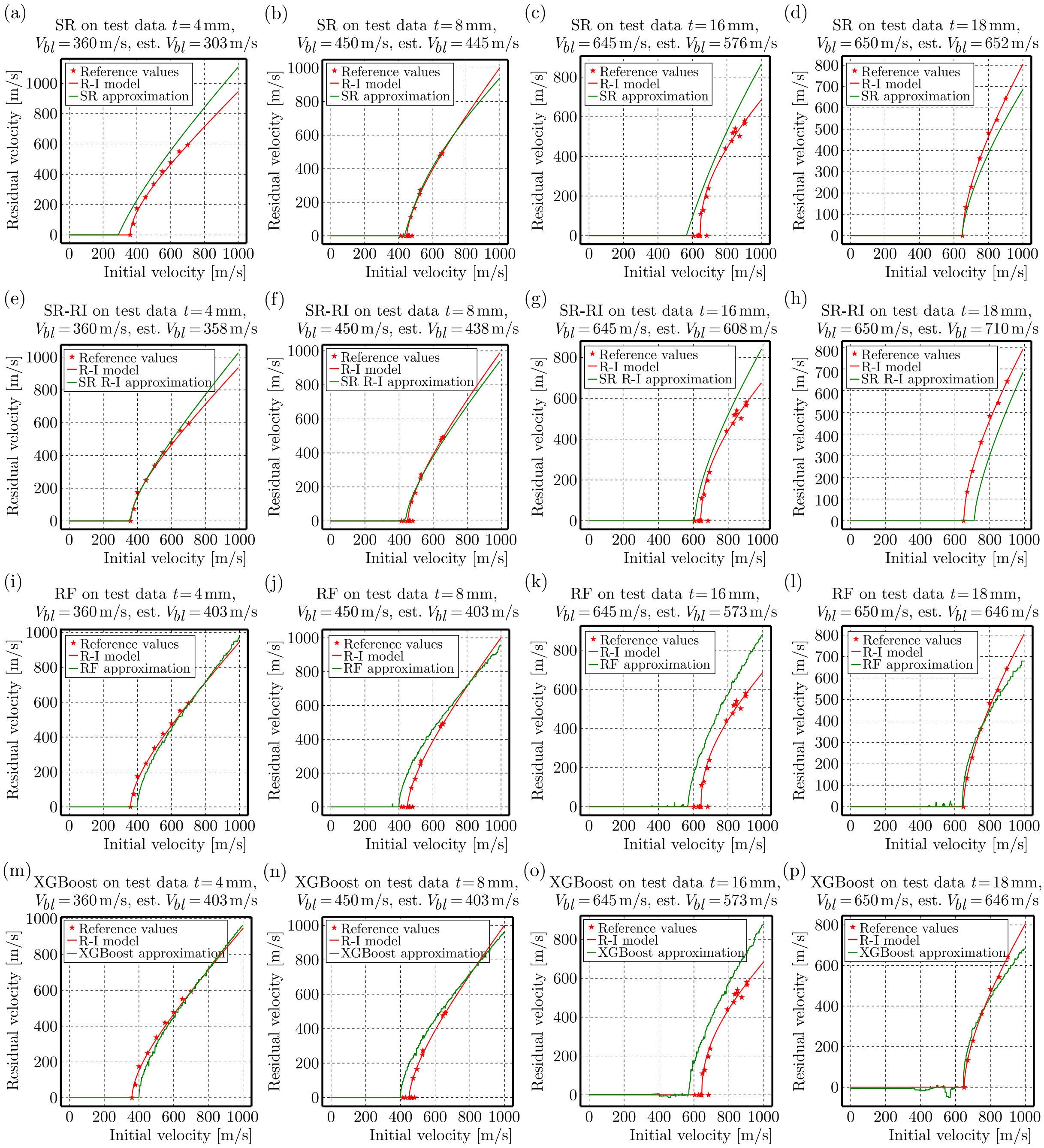

Fig. 3. Approximation of BLCs of all four ML methods trained on all but one thickness from our dataset that predict the shape BLC for the thickness that was not present in the dataset: (a)–(d) example results for SR; (e)–(h) for SR R-I; (i)–(l) for RF regressor, and (m)–(p) for XGBoost regressor. Red lines indicate the reference R-I model curve fitted to data marked as red stars, and green lines are the ML model approximation.

The equation approximated with SR for unknown $t = 8$ mm with RMSE $= 17.674$ on validation dataset for S355 steel valid in range $t \in [4, 18]$ mm is

$$h_{\mathrm{SR}}(v_i,t) = \left(\left(106.931^{\frac{215.235}{v_i}} - 1.566\right) \cdot \left(5.784^{(\log_{10}(t))^2}\right) \cdot (-12.323)\right) + v_i, \qquad t > 0,\ v_i \neq 0, \tag{3.7}$$

$$\widehat{v_r}(v_i,t)_{\mathrm{SR}} = \begin{cases} h_{\mathrm{SR}}(v_i,t) & \text{if} \quad h_{\mathrm{SR}}(v_i,t) \geq 0, \\ 0 & \text{else}. \end{cases} \tag{3.8}$$

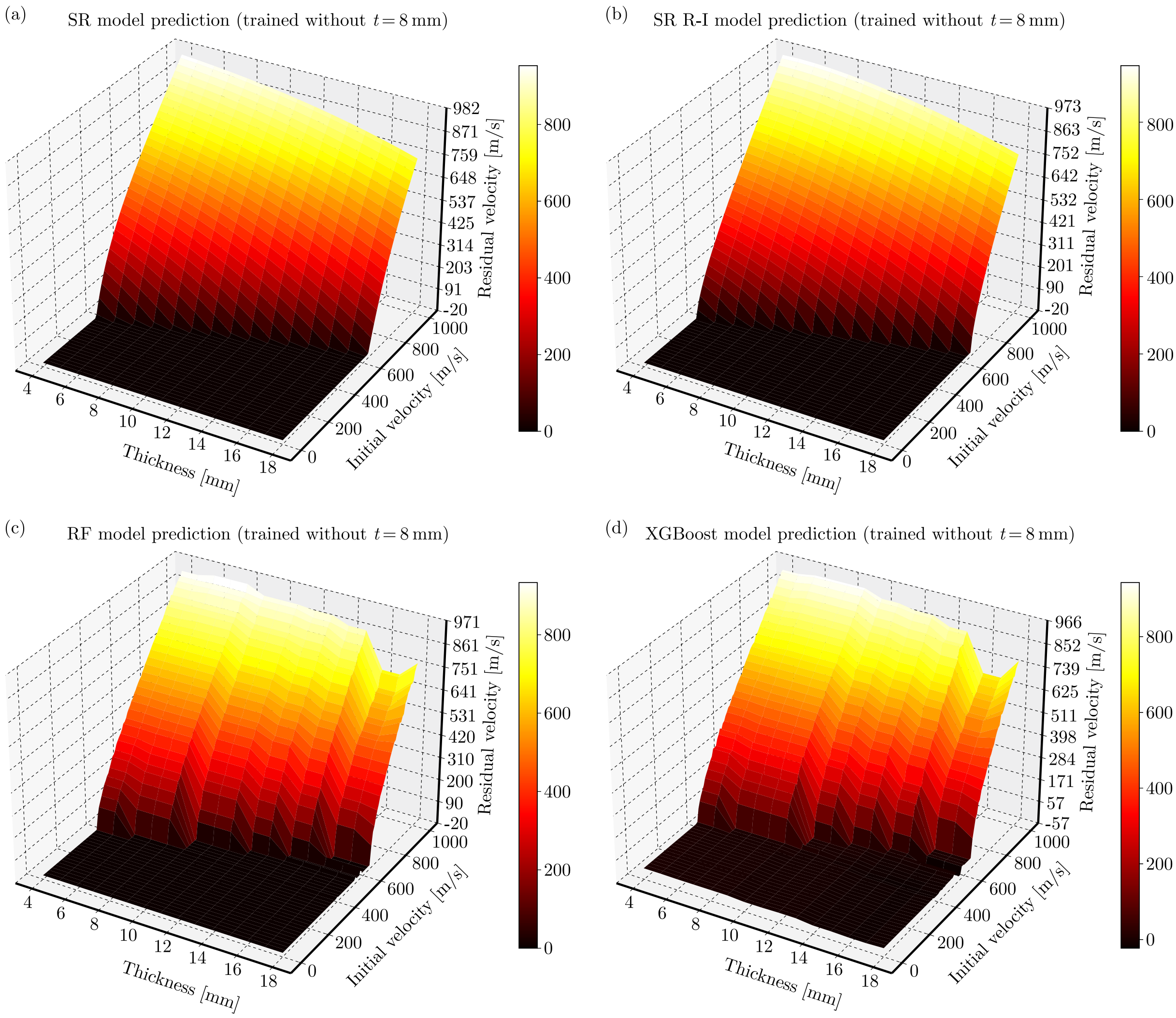

Fig. 4. Visualisations of $\widehat{v_r}(v_i, t)$ from Eq. (2.2) in the form of the surface plot: (a) is surface obtained with Eq. (3.8), (b) with Eq. (3.10), (c) with a RF regressor, (d) with an XGBoost regressor.

Note that this is a raw, not a physically meaningful, decomposition from SR.

In order to estimate BLV for a given t, one can use a heuristic that takes into consideration local monotonicity of $\widehat{v_r}$, a positive value of the first derivative, and a certain threshold (see (Hachaj & Frąś, 2026) for more details). The same heuristic was used for RF and XGBoost.

The equation approximated with SR R-I for unknown $t = 8$ mm with RMSE $= 26.153$ on the validation dataset for the steel S355 valid in the range $t \in [4, 18]$ mm is

$$\begin{cases} \mathcal{a}(t) = t^{0.08}, \quad t \geq 0, \\ \mathcal{p}(t) = 1.534, \\ v_{\mathcal{bl}}(t) = (t + 12.697) \cdot 21.175, \end{cases} \tag{3.9}$$

and after applying Eq. (3.9) to Eq. (2.2) becomes:

$$\widehat{v_r}(v_i, t)_{\text{SR R-I}} = \\ \begin{cases} t^{0.08} \cdot (v_i^{1.534} - ((t + 12.697) \cdot 21.175)^{1.534})^{\frac{1}{1.534}} & \text{if} \quad v_i^{1.534} \geq ((t + 12.697) \cdot 21.175)^{1.534}, \\ 0 & \text{else}. \end{cases} \tag{3.10}$$

In order to estimate BLV for a given t one can directly use $v_{b\ell}(t)$ from Eq. (3.9). Note that the SR-derived function represents a smooth approximation (regularization effect) rather than a direct physical law. The primary objective is the accurate reconstruction of BLC/BLV rather than preserving parameter-level physical interpretation. Also, fixing $p(t)$ to a constant 1.534 removes a degree of freedom that the data clearly support. This might surely cause a loss of fit in the SR R-I compared to the situation in which p is allowed to depend on t.

4. Discussion

Based on the results presented in Table 2 and Table 3 and plots in Fig. 3, it may be observed that all evaluated ML methods generated the expected shapes of BLC. Those curves have relatively low error on experimental and numerical simulation data in leave-one-out cross-validation. It should be noted that in each case, validation data consist only of thicknesses that were not used in the training. Hence, a low error value indicates a strong generalization capability of the ML algorithms. We observe that SR algorithms (SR and SR R-I) perform very similarly, and decision tree-based algorithms (RF and XGBoost) also yield nearly identical errors. The lowest value of RMSE (51.656 $\pm$38.218) in the curve approximation task was achieved by SR, in the case of MAE (46.248 $\pm$44.058) by SR R-I, and in the case of R^2 by SR (0.908 $\pm$0.116). However, as shown in Table 4 and Table 5, the Wilcoxon test indicates that the difference between SR and SR R-I is not statistically significant. The RF and XGBoost perform significantly worse than SR, and there is no significant difference between the two decision tree-based methods. A similar conclusion can be drawn from evaluating how well models approximate BLV. Again, the SR R-I algorithm yielded the lowest error values: the MRE was 0.028 $\pm$0.029 (only 3% $\pm$2% of the reference values compared to other methods), RMSE was 25.678, MAE was 20.375, and R^2 was 0.934. However, according to Table 6 and Table 7, there are no significant statistical differences in RE and AE between SR methods, and they are statistically better than RF and XGBoost. Since our statistical tests approximate their resolution limit, their statistical power is modest, and the SR vs SR R-I comparison may be underpowered rather than truly null.

It should be noted that for the cases visualized in Fig. 3a and Fig. 3e, the SR approximation and SR R–I model seem to provide a nonphysical response, i.e., the residual velocity is higher than the initial velocity. This is evident at the ends of the interval under consideration, at the maximum value of the velocity v_i. This was likely because the model extrapolated the results to 4 mm. In contrast, the RF and XGBoost approaches exhibit nonphysical responses (lack of monotonicity), especially at the plateau near v_{bl}. This error stemmed from the nature of these models, which are aggregations of "weak" predictors.

The shapes of BLC generated by SR that are plotted in Fig. 3 indicate the monotonicity of the obtained solutions. In the case of RF and XGBoost, there are some fluctuations (characteristic steps in the plots) that are typical of decision tree-based algorithms. We can also observe those patterns in surface plots in Fig. 4. Equation (3.10) calculated by SR R-I is far more intuitive and easier to understand than Eqs. (3.7) and (3.8) done by SR. What is more, using Eq. (3.9), we can estimate BLV directly, which is not possible in other methods without the proposed heuristics. In summary, thanks to the SR R-I approach, we were able to compute analytical formulae for 2D BLCs over the range of material thickness for S355 Steel in ballistic events with 7.62 mm AP P80, which can be applied in engineering practice. When applying the Pareto front, the solution complexity is a trade-off for its accuracy. Often, a more complex solution containing more terms fits the dataset better than a simpler one. However, they might become less interpretable (see, for example, Eqs. (3.7) and (3.9)).

The application of a reliable, correctly fitted SR solution offers significant benefits over deep learning black-box models such as ANNs and larger language models (LLMs). The most important advantage is the full interpretability of the resulting solution, along with the ability to trace the process by which the result was obtained – something that is practically impossible in the case of deep learning. Furthermore, the resulting numerical function can be subjected to standard mathematical analysis to verify its consistency with physical assumptions, which is also practically impossible (or at least very difficult) for deep models with thousands or even millions of parameters. For this reason, interpretable knowledge distillation (Shmuel *et al.*, 2026) via SR ML is becoming an increasingly common practice in physical sciences (Varughese *et al.*, 2026).

There are several limitations of the proposed analytical solution. Equation (2.2) (and Eqs. (3.9) and (3.10)) takes into account the R-I model only through the term t, which corresponds to material thickness. Other parameters that might be interesting for this type of model include projectile type (the shape of the BLC curve also depends on the projectile's shape (Fonseca *et al.*, 2025)), target material properties, and the angle of impact. To include those parameters in the model, a series of experiments must be performed that covers all the variables. This is a necessary procedure for any ML-based model. We can anticipate that the modified, enhanced solution (Eq. (2.2)) that takes into account all those parameters should be in the form:

$$\begin{aligned}\widehat{v_r}(v_i, t, \alpha, \mathscr{P}, \mathscr{M}) &= \mathscr{a}(t, \alpha, \mathscr{P}, \mathscr{M}) \cdot \left(v_i^{\mathscr{p}(t,\alpha,\mathscr{P},\mathscr{M})} - v_{\mathscr{bl}}(t, \alpha, \mathscr{P}, \mathscr{M})^{\mathscr{p}(t,\alpha,\mathscr{P},\mathscr{M})}\right)^{\frac{1}{\mathscr{p}(t,\alpha,\mathscr{P},\mathscr{M})}}, \\ v_i &\geq v_{\mathscr{bl}}(t, \alpha, \mathscr{P}, \mathscr{M}),\end{aligned} \tag{4.1}$$

where α is an angle of impact (numerical value), $\mathscr{P}$, $\mathscr{M}$ are projectile and material properties (categorical values). It should be noted that the final solution will represent the $\mathscr{P}$, $\mathscr{M}$ as tabular-like categories rather than numerical values. We believe that the properties of materials and projectiles are too complex to be represented as single numerical values. Also, while applying the symbolic solution, it is not recommended to have more than four to five variables, because this is the border value above which the genetic algorithm can struggle to explore the search space effectively. With all these considerations taken into account, the model might become reliable for a wide range of materials and projectile types beyond S355 vs 7.62 mm × 51 mm AP P80 impacts at 0° NATO.

The main objective of this study was to investigate whether the R-I model can be generalized using SR methods. A particularly interesting research question is the minimum number of cross-sections required to obtain a stable (repeatable) solution with a given level of generalization and point-fit accuracy. In our case, we limited our tests to seven cross-sections in a leave-one-out evaluation, since conducting ballistic experiments is costly and simulating them using FEM requires significant computational resources over a relatively long period of time. To answer the question of how many cross-sections are necessary to estimate the function's variability, it depends on the form of the surface equation we expect. SR-based approximation differs fundamentally from, for example, polynomial interpolation, because in SR, we cannot state that to fit an n-th-degree polynomial, we need exactly $n+1$ points. Additionally, RL allows the use of various binary and unary operators, which can be treated as types of basis functions, significantly complicating the estimation of the required number of points. Based on our observations, seven curves appear to be sufficient to derive a model with satisfactory accuracy and low complexity for an approximately linear relationship. However, this number may prove insufficient for other materials or when additional parameters are included in the model (see Eq. (4.1)).

5. Conclusions

By applying SR, which embedded the R-I model within the PASR paradigm, we have obtained an intuitive and accurate solution which extends the original well-known equation. The SR R-I model performs with statistically proven effectiveness as SR and outperforms state-of-the-art RF and XGBoost approaches in both overall BLC fits and in predicting BLVs for unknown thicknesses. The obtained results confirmed the findings of our previous study (Hachaj & Frąś, 2026) that the application of stochastic physics-based oversampling enables us to generate a dataset large enough to train the repressor, providing sufficient points in a very narrow region near the BLV, which is critical for precise ML fit and prognostic ability of limit velocity values for unknown thicknesses. The proposed SR R–I model provides accurate interpolation within the training thickness range, with graceful degradation near boundary conditions. The results indicate that it is possible to use SR in selected terminal ballistic problems involving 355 steel targets penetrated by 7.62 mm AP P80, and to obtain explainable, interpretable solutions. The results may prove significant from scientific, cognitive, and practical engineering perspectives.

The SR R-I methodology we presented in this research is not limited to this specific material only, but can also be applied to other ballistic targets, and it is possible to find more general analytical formulae for many materials by applying parametric expressions to constraints. The other very promising research goal is to combine SR with LLMs. The initial research demonstrates that LLM integration consistently improves the reconstruction of physical dynamics from data, enhancing the robustness of SR models to noise and complexity (Fras & Pawlowski, 2026; Shen *et al.*, 2024; Taskin *et al.*, 2026). There are already publications on predicting the depth of the resulting crater following an impact. Rietkerk *et al.* (2023) and Ryan *et al.* (2024) modelled the impact of a long rod projectile at a given initial velocity into a semi-infinite target block using various ML approaches like XGBoost, ANN, support vector regression (SVR), Gaussian process regression, and physics-informed ML. As this represents a different experimental setup from that considered in the present study, we did not investigate it. Nevertheless, we consider it an interesting direction for future research.

References

1. Abid, K.A., Syed, S.A., & Khan, M. (2026). Interpretable machine learning models for predicting penetration depth in ultra-high-performance concrete under ballistic impact. *Structural Concrete*. https://doi.org/10.1002/suco.70462

2. Anderson Jr., C.E., & Bodner, S.R. (1988). Ballistic impact: The status of analytical and numerical modeling. *International Journal of Impact Engineering*, *7*(1), 9–35. https://doi.org/10.1016/0734-743X(88)90010-3

3. Cranmer, M. (2023). Interpretable machine learning for science with PySR and symbolic regression.jl. *arXiv*. https://doi.org/10.48550/arXiv.2305.01582

4. Deng, Y., Lv, Y., Yang, X., Du, C., & Huang, X. (2025). Determination of residual velocity model of finite thickness material based on Artificial Neural Network. *Thin-Walled Structures*, *216*(Part B), Article 113685. https://doi.org/10.1016/j.tws.2025.113685

5. Dwivedi, R., Dave, D., Naik, H., Singhal, S., Omer, R., Patel, P., Qian, B., Wen, Z., Shah, T., Morgan, G., & Ranjan, R. (2023). Explainable AI (XAI): Core ideas, techniques, and solutions. *ACM Computing Surveys*, *55*(9), Article 194. https://doi.org/10.1145/3561048

6. El Hasadi, Y.M.F., & Elghannay, H.A. (2026). A physics aware symbolic regression formula for the wall effects on a sphere moving inside a cylindrical tube. *International Journal of Multiphase Flow*, *198*, Article 105640. https://doi.org/10.1016/j.ijmultiphaseflow.2026.105640

7. European Committee for Standardization. (2019). *Hot rolled products of structural steels – Technical delivery conditions for non-alloy structural steels* (EN 10025-2:2019).

8. Fonseca, L.C., Peixoto, F.C., & Nichele, J. (2025). *Yaw-induced transitions in ballistic limit and fracture mechanisms in steel plate perforation* (version 1). Research Square. https://doi.org/10.21203/rs.3.rs-7767315/v1

9. Fras, T., & Pawlowski, P. (2026). On the applicability of generative artificial intelligence in modelling the dynamic behaviour of materials–potentials and pitfalls. *Journal of Dynamic Behavior of Materials*. https://doi.org/10.1007/s40870-025-00506-5

10. Frąś, T., Nowak, Z., Perzyna, P., & Pęcherski, R.B. (2011). Identification of the model describing viscoplastic behaviour of high strength metals. *Inverse Problems in Science and Engineering*, *19*(1), 17–30. https://doi.org/10.1080/17415977.2010.531474

11. Hachaj, T., & Frąś, T. (2026). Approximation of two-dimensional ballistic limit curves in the range of material thickness with stochastic physical-based oversampling. *Bulletin of the Polish Academy of Sciences Technical Sciences*, *74*(3), Article e158297. https://doi.org/10.24425/bpasts.2026.158297

12. Hachaj, T., & Piekarczyk, M. (2025). On explainability of reinforcement learning-based machine learning agents trained with proximal policy optimization that utilizes visual sensor data. *Applied Sciences*, *15*(2), Article 538. https://doi.org/10.3390/app15020538

13. Husain, A., Danish, M., Khan, S.H., & Mourad, A.-H.I. (2024). Predicting projectile residual velocities using an advanced artificial neural network model. *Heliyon*, *10*(11), Article e32149. https://doi.org/10.1016/j.heliyon.2024.e32149

14. Karl, J., Kirsch, F., Faderl, N., Perko, L., & Fras, T. (2020). Optimizing viscoelastic properties of rubber compounds for ballistic applications. *Applied Sciences*, *10*(21), Article 7840. https://doi.org/10.3390/app10217840

15. Karniadakis, G.E., Kevrekidis, I.G., Lu, L., Perdikaris, P., Wang, S., & Yang, L. (2021). Physics-informed machine learning. *Nature Reviews Physics*, *3*(6), 422–440. https://doi.org/10.1038/s42254-021-00314-5

16. Lasdon, L.S., Fox, R.L., & Ratner, M.W. (1974). Nonlinear optimization using the generalized reduced gradient method. *R.A.I.R.O. Recherche opérationnelle*, *8*(V3), 73–103. https://doi.org/10.1051/ro/197408V300731

17. Levadnyi, I., Liu, F., & Gu, Y. (2024). Ballistic performance of TPU/steel configurations against spherical projectiles. *AIP Advances*, *14*(11), Article 115321. https://doi.org/10.1063/5.0239540

18. Li, W., Bian, Z., Chen, T., Mao, C., & Zhang, C. (2026). Reverse prediction of impact parameters for 3D woven fabrics subjected to ballistic impact using deep learning methods. *Mechanics of Advanced Materials and Structures*, *33*(1), Article 2569075. https://doi.org/10.1080/15376494.2025.2569075

19. Recht, R.F., & Ipson, T.W. (1963). Ballistic perforation dynamics. *Journal of Applied Mechanics*, *30*(3), 384–390. https://doi.org/10.1115/1.3636566

20. Rietkerk, R., Heine, A., & Riedel, W. (2023). Physics-informed machine learning model for prediction of long-rod penetration depth in a semi-infinite target. *International Journal of Impact Engineering*, *173*, Article 104465. https://doi.org/10.1016/j.ijimpeng.2022.104465

21. Rosenberg, Z., & Dekel, E. (2012). *Terminal ballistics*. Springer. https://doi.org/10.1007/978-3-642-25305-8

22. Ryan, S., Sushma, N.M., Kumar AV, A., Berk, J., Hashem, T., Rana, S., & Venkatesh, S. (2024). Machine learning for predicting the outcome of terminal ballistics events. *Defence Technology*, *31*, 14–26. https://doi.org/10.1016/j.dt.2023.07.010

23. Saifoori, S., Hosseinhashemi, S., Alasossi, M., Schilde, C., Nezamabadi, S., & Ghadiri, M. (2025). AI-assisted prediction of particle impact deformation simulated by material point method. *Powder Technology*, *459*, Article 121018. https://doi.org/10.1016/j.powtec.2025.121018

24. Shen, J., Tenenholtz, N., Hall, J.B., Alvarez-Melis, D., & Fusi, N. (2024). Tag-LLM: Repurposing general-purpose LLMs for specialized domains. *Proceedings of the 41st International Conference on Machine Learning*, *235*, 44759–44773.

25. Shmuel, A., Koren, N., Glickman, O., & Lazebnik, T. (2026). Interpretable knowledge distillation via symbolic regression for feedforward neural networks. *Neural Computing and Applications*, *38*(7), Article 243. https://doi.org/10.1007/s00521-026-12067-2

26. Taskin, B., Xie, W., & Lazebnik, T. (2026). Knowledge integration for physics-informed symbolic regression using pre-trained large language models. *Scientific Reports*, *16*, Article 1614. https://doi.org/10.1038/s41598-026-35327-6

27. Varughese, B., Loeffler, T.D., Banik, S., Koneru, A., Manna, S., Balasubramanian, K., Batra, R., Cherukara, M.J., Yildiz, O., Peterka, T., Sumpter, B.G., & Sankaranarayanan, S.K.R.S. (2026). Physically interpretable interatomic potentials via symbolic regression and reinforcement learning. *npj Computational Materials*, *12*, Article 84. https://doi.org/10.1038/s41524-025-01952-4

28. Wei, Q., Chen, J., Liu, Y., & Zhang, H. (2024). Numerical analysis of ballistic performance in hybrid structures of triaxial and plain fabrics. *Journal of Materials Science*, *59*(45), 21069–21086. https://doi.org/10.1007/s10853-024-10445-6

29. Zhang, L., Zhang, Z., Zhang, Y., Chen, L., Li, S., Zhu, L., Ye, Y., Chen, R., & Bai, S. (2026). Machine learning driven impact fracture understanding and end-to-end design of energetic multi-principal-element alloys. *Defence Technology*, *59*, 217–230. https://doi.org/10.1016/j.dt.2025.11.026

30. Zou, D., Thoti, D., & Bao, Z. (2025). Study on the application of discrepancy-guided symbolic regression algorithm in analyzing the impact resistance of UHP-SFRC target against high velocity projectile impact. *International Journal of Impact Engineering*, *201*, Article 105276. https://doi.org/10.1016/j.ijimpeng.2025.105276

Manuscript received March 26, 2026; accepted for publication July 4, 2026; published online August 17, 2026.

JOURNAL OF THEORETICAL
AND APPLIED MECHANICS
64, 3, pp. 201–216, Warsaw 2026
https://doi.org/10.15632/jtam-pl/225473

PASSIVE SUSPENSION SYSTEM OF A CHILD SAFETY SEAT – OPTIMIZATION AND ANALYSIS OF VIBRATION ISOLATION EFFECTIVENESS

Natalia Justyna FLOREK*, Igor MACIEJEWSKI, Tomasz KRZYŻYŃSKI

Faculty of Mechanical and Energy Engineering, Koszalin University of Technology, Koszalin, Poland
*corresponding author, *natalia.florek@s.tu.koszalin.pl*

The aim of the study is to analyze the vibration damping properties of a passive suspension system for a child car seat that is designed to reduce the impact of vertical accelerations on the child's body during vehicle travel. The motivation for undertaking this research is the absence of vibration isolation solutions dedicated to this group of users, despite the well-documented sensitivity of children to vibrations in the frequency range of 4 Hz to 10 Hz. A physical and mathematical model of the suspension system was developed in the MATLAB/Simulink environment, incorporating springs, hydraulic dampers, bump stops, and nonlinear friction forces. To evaluate vibration isolation performance, acceleration signals were analyzed using the power spectral density (PSD), the root mean square (RMS) value, and the Seat Effective Amplitude Transmissibility (SEAT) factor. In the study, the influence of key structural parameters such as spring stiffness, damping characteristics, and end-stop elements on the effectiveness of vibration reduction was analyzed. Subsequently, a multi-objective optimization procedure was applied to determine the optimal parameters of the suspension system, aiming to minimize the accelerations transmitted to the child seat while maintaining the required design constraints. Simulation results demonstrated that the proposed passive system significantly reduces vibration amplitudes within the low-frequency range and improves the value of the SEAT factor. The results confirm the potential of passive vibration isolation systems for child safety seats and provide a basis for further experimental validation.

Keywords: vibration isolation; child car seat; passive suspension system; SEAT factor; power spectral density (PSD).

1. Introduction

The primary motivation for undertaking this research is the evident gap in the literature concerning the influence of mechanical vibrations on children traveling in automotive child safety seats. Despite numerous studies addressing vibration isolation systems for driver and adult passenger seats, there is a noticeable lack of investigations that consider the biomechanical specificity of children and their increased susceptibility to vertical vibrations. Table 1 presents the natural frequency ranges of various body parts in children, which differ significantly from the characteristic values reported for adults. These data were compiled, among others, on the basis of studies by Gromadowski and Więckowski (2012), who analyzed the effects of mechanical vibrations on the human body using literature data and industry standards, including ISO 2631, which defines

Ministry of Science and Higher Education
Republic of Poland
WEKTORY NAUKI

This publication has been funded by the Polish Ministry of Science and Higher Education under the "Vectors of Science" programme, project number WNK/SN/0508/2025/01, with project funding of PLN 134,200.00 and total project value of PLN 174,200.00.
The content of this article was presented during the 62nd Symposium "Modelowanie w mechanice" (Modelling in Mechanics), Szczyrk, Poland, March 1–4, 2026.

Table 1. Natural frequency ranges of selected human body parts (Gromadowski & Więckowski, 2012).

Body part	Natural frequency range [Hz]	Effects of vibration exposure	Group
Head	4–5	Headaches, dizziness, discomfort	Child
Thorax (chest)	5–7	Chest pressure, shallow breathing, pain	
Abdomen	4–8	Muscle tension	
Limbs	6–8	Numbness	
Spine	4–9	Pain	
Whole body	4–10	Fatigue, nausea, general weakness	
Vestibular system (balance)	<6	Balance disturbances, disorientation	
Head	2–3	Headache, reduced concentration	Adult
Thorax (chest)	5–7	Respiratory disturbances	
Pelvis / spine	6–8	Lower back pain, discomfort	

comfort limits and permissible levels of vibration exposure. The conclusions drawn from these studies clearly indicate that due to their lower body mass, different anatomical structure, and immature musculoskeletal system, children exhibit significantly higher sensitivity to vibrations, particularly in the vertical direction. The range of frequencies considered harmful to children extends from 4 Hz to 10 Hz, implying that they are exposed to a broader and more intense vibration impact than adults (Wicher & Więckowski, 2010).

The child safety seat suspension system designed within the scope of this study constitutes an innovative solution aimed at reducing the transmission of mechanical vibrations to the user during vehicle operation. The primary objective of developing the passive system was to achieve the highest possible vibration isolation effectiveness while maintaining structural simplicity and operational reliability resulting from the absence of active components. The proposed system is intended to attenuate vibrations within the frequency range characteristic of excitations generated by road surface irregularities and vehicle body dynamics, while simultaneously minimizing accelerations acting on the child's body (Florek & Maciejewski, 2025). The effectiveness of vibration isolation is evaluated using vibration comfort indicators, such as the root mean square (RMS) value of accelerations and the Seat Effective Amplitude Transmissibility (SEAT) factor. As part of the literature review, scientific publications addressing the effects of mechanical vibrations on the human body and the effectiveness of various vibration isolation solutions were analyzed. Based on a critical assessment of the available studies, it can be concluded that children exhibit a biomechanical response to vibration that differs significantly from that of adults, which makes the application of general comfort assessment standards, such as ISO 2631, insufficient for the evaluation of vibration exposure in young passengers (Giacomin, 2005). It has been demonstrated that standard child safety seats do not provide effective vibration isolation; in many cases, amplification of vibration amplitudes is observed within the frequency range of 1.5 Hz to 60 Hz, particularly in the absence of dedicated damping elements (Giacomin, 2000; Bai *et al.*, 2017). An important factor influencing vibration transmission between the vehicle and the child's body is the method of seat installation. The ISOFIX system, in contrast to traditional seatbelt-based mounting, enables a significant reduction in transmitted vibration amplitudes and increases the repeatability and stability of the connection (Wicher & Więckowski, 2010; Gromadowski & Więckowski, 2012). The literature also emphasizes that significant sources of vibrational disturbances may include external factors such as road surface irregularities, wheel imbalance, and wear of vehicle suspension components (Frej & Grabski, 2019; Frej, 2018).

In addition to studies focused directly on child safety seats, broader research on dynamic systems and vibration response has also been conducted. In particular, the analysis of mechanical systems subjected to random and transport-induced excitations has gained significant attention in recent years. Numerous studies have addressed the analysis and modeling of dynamic systems subjected to vibration excitation, including transport-related vibrations and random loading conditions. Research conducted by Duda *et al.* (2020), Hryciów *et al.* (2021), and Łagoda (2001) highlights the importance of accurate modeling of dynamic responses and energy transfer mechanisms in systems exposed to stochastic excitations. These approaches provide a valuable background for the analysis and optimization of vibration isolation systems. Finite element modeling has also been widely used in seat-structure and human–seat interaction analyses. Zhang *et al.* (2015) developed an FE model of a car seat with an occupant to predict vertical vibration transmissibility, while Alawneh *et al.* (2022) reviewed FE approaches for human–seat interaction. These studies confirm the importance of numerical modeling in seating comfort analyses, although the present work adopts a lumped-parameter model to enable efficient multi-variant optimization.

The literature review clearly indicates that, despite numerous studies addressing vibration comfort in adult vehicle occupants, passive systems dedicated specifically to child safety seats remain lacking. Existing designs do not account for the biomechanical specificity of young children, which results in increased transmission of vibrations to the user's body. The suspension system developed within the scope of this study addresses this research gap by focusing on a passive solution with optimized damping and stiffness characteristics tailored to the vibration sensitivity of children. Current vibration comfort assessment standards, such as ISO 2631 (International Organization for Standardization, 1997; 2001; 2018), were developed primarily for adult users and do not account for the biomechanical specificity of children or the distinct natural frequencies of individual body segments. Based on an analysis of recent scientific studies, it can be unequivocally stated that children exhibit a markedly different biomechanical response to mechanical vibrations compared to adults. Giacomin (2005) demonstrated that standard child seat vehicle systems transmit vibrations of significantly higher amplitude to the child's body, particularly in low-frequency bands. Furthermore, in studies on the so-called *apparent mass* of children, Giacomin (2004) confirmed that their biodynamic response to vibration differs substantially from that of adults. Bai *et al.* (2017) analyzed the effects of vibration on different segments of the spine and showed that the sensitivity of the lumbar vertebrae in children to specific vibration frequencies is considerably higher than in adults. Consequently, numerous studies question the adequacy of applying general standards such as ISO 2631 to the assessment of vibration comfort in children traveling in vehicles. Nilsson (2005) and Florek and Maciejewski (2025) argue that although these standards are widely used in analyses of adult vibration exposure, they do not account for the physiological and biomechanical differences present in children, which may lead to an incorrect assessment of health-related risks. A similar position is presented by Zuska *et al.* (2021), who suggest the need to revise existing standards or to develop child-specific counterparts.

Another important conclusion, confirmed by multiple studies, concerns the ineffectiveness of standard child safety seats in isolating vibrations. Giacomin (2005) and Frej and Grabski (2023) demonstrated that, rather than attenuating vibrations, many commercially available child seats amplify vibration amplitudes. Wicher and Więckowski (2010) and Gromadowski and Więckowski (2012) further indicate that the absence of damping elements in a child safety seat may lead to resonance effects and increased transmission of vibrations to the child's body. The effectiveness of vibration attenuation is also strongly influenced by the method of seat installation. Improved stability and repeatability of installation were also reported, which translates into reduced exposure of the child to unwanted vibrations. The literature additionally highlights external sources of vibration, such as road surface irregularities, wheel imbalance, and wear of vehicle suspension components. Frej (2018) demonstrated that the technical condition of the vehicle has a direct impact on the level of vibrations transmitted to the cabin interior and indirectly to the child. Against the background of these findings, a clear research gap emerges in the area of dedicated passive vibration protection systems for the youngest vehicle occupants. Addressing this deficiency may be achieved through the development of a passive damping system with properties tailored to the biomechanical characteristics of children, which constitutes the objective of the engineering solution proposed in this study. In response to these limitations, the development of a dedicated suspension system for child safety seats is proposed, with the primary goal of reducing the transmission of vertical vibrations to the child's body (Florek & Maciejewski, 2025). As part of the research, both a physical and a mathematical model of the system were developed in the MATLAB/Simulink environment, incorporating excitation forces generated by road surface irregularities as well as the dynamic response of the suspension system. The model was calibrated for the frequency range characteristic of children aged 0–6 years, enabling an assessment of vibration attenuation effectiveness under simulation conditions.

2. Physical and mathematical model of the passive system

2.1. Physical model

Figure 1 presents a simplified physical model of the passive suspension system of a child safety seat. The model consists of a single lumped mass m_1, representing the combined system of the child safety seat and the child's body:

$$m_1 q_{1z} = -F_{sz} - F_{bz} - F_{dz} - F_{fz}. \tag{2.1}$$

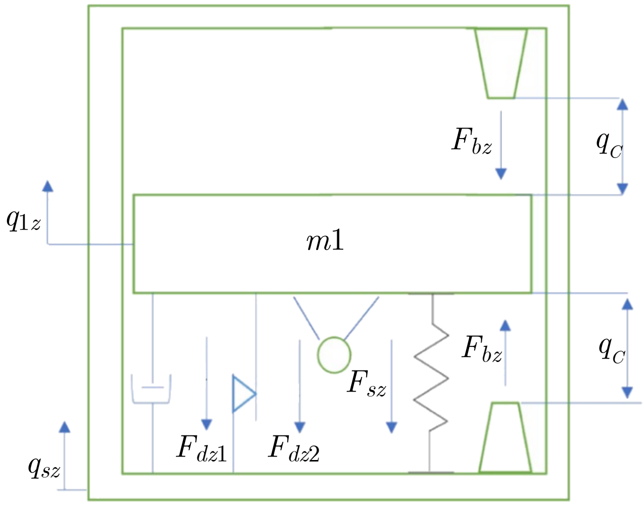

Fig. 1. Physical model of the passive suspension system of a child safety seat (Maciejewski *et al.*, 2020).

The lumped mass m_1 is subjected to passive forces acting within the system: F_{sz}, the spring force, responsible for storing elastic energy in the system and defining its stiffness; F_{dz1}, the damping force generated by fluid flow in the hydraulic damper during the relative motion between the child seat and the base; F_{bz}, the force produced by the end stops (elastic bumpers), which limit the maximum displacement of the mass and prevent impacts at extreme positions; and F_{fz}, the friction force resulting from the contact and guidance of moving components, providing a stabilizing effect at low relative velocities. The variable q_{1z} denotes the vertical displacement of the mass m_1, while q_{sz} refers to the displacement of the suspension base. The difference $q_{1z} - q_{sz}$ defines the relative displacement of the system and constitutes the basis for calculating the elastic and damping forces. In the contact region with the end stops, an additional variable q_C is introduced, representing the activation threshold of the bumper, beyond which the nonlinear force characteristic F_{bz} becomes effective. The model assumes a single degree of freedom, which enables a precise analysis of vertical vibrations of the vibration isolation system in response to base excitation $q_{sz(t)}$.

2.2. Mathematical model

The mathematical description of the passive system comprises four main force components responsible for its dynamic properties: elasticity, damping, displacement limitation, and friction.

2.2.1. Spring force

The relationship between the relative displacement of the system $(q_{1z} - q_{sz})$ and the elastic force is expressed by the following relation:

$$F_{sz} = \frac{G_s\, d_s^4}{8\, n_s\, D_s^3}(q_{1z} - q_{sz}), \tag{2.2}$$

where G_s denotes the shear modulus of the spring material, d_s is the spring wire diameter, D_s is the mean coil diameter, and n_s represents the number of active coils. This relationship describes the classical linear model of a helical spring, in which the force is proportional to the spring deflection. The geometric parameters of the wire and the coil have a crucial influence on the effective stiffness of the system, which in the subsequent part of this study constituted the basis for the structural optimization process (Krzyzynski *et al.*, 2019).

2.2.2. End-stop bumper force

The end-stop bumper force was formulated as a piecewise function of the relative displacement between the suspended mass and the system base, enabling the representation of successive operating phases: no contact, a linear response, and a nonlinear behavior at large deflections:

$$\begin{aligned}
&F_{bz} = 0 && \text{for} \quad |r| \leq q_C + \delta,\\
&F_{bz} = \operatorname{sgn}(r)\, c_{b1}(|r| - q_C - \delta) && \text{for} \quad q_C + \delta < |r| \leq q_T,\\
&F_{bz} = \operatorname{sgn}(r)\, c_{b3}(|r| - q_T - \delta)^3 + c_{b1}(|r| - q_C - \delta)] && \text{for} \quad |r| > q_T + \delta,
\end{aligned} \tag{2.3}$$

$$F_{nr} = c_{b3}(q_{1z} - q_{sz} - q_T - \delta) + c_{b1}(q_{1z} - q_{sz} - q_C - \delta), \tag{2.4}$$

$$F_{lr} = c_{b1}(q_{1z} - q_{sz} - q_C - \delta), \tag{2.5}$$

where $r = q_{1z} - q_{sz}$.

The force generated by the end-stop bumper, which serves as a suspension travel limiter, is described by Eq. (2.3). Its magnitude depends on the relative displacement between the suspended mass and the system base, denoted as $(q_{1z} - q_{sz})$. In the model, it is assumed that for small displacement values satisfying the condition $| q_{1z} - q_{sz} | \leq q_C + \delta$, the bumper does not generate any reaction force, which corresponds to the absence of contact between the bumper and the moving platform. Once the threshold value $(q_C + \delta)$ is exceeded, the bumper enters a linear operating region. In this range, the force increases proportionally with displacement and is described by $F_{bz} = c_{b1}(q_{1z} - q_{sz} - q_C - \delta)$. The linear elastic model applied in this region represents the behavior of a pre-compressed elastomer or rubber stop, which begins to transmit mechanical loads only after the assembly clearance has been eliminated. With further increase in deflection, when the condition $| q_{1z} - q_{sz} | > q_T + \delta$ is satisfied, the element enters a nonlinear operating region. The bumper characteristic then assumes a cubic form and is expressed as $F_{bz} = c_{b3}(q_{1z} - q_{sz} - q_T - \delta)^3 + c_{b1}(q_{1z} - q_{sz} - q_C - \delta)$. The inclusion of the nonlinear term enables an accurate representation of the rapid stiffness increase characteristic of rubber and polyurethane bumpers in the final stage of deformation. Additionally, for situations involving dynamic impact against the travel limiter, an impact reaction force F_{nr} was introduced and is described by Eq. (2.4). This term accounts for the elastic rebound effect occurring during rapid contact with the travel limit and enables the representation of an asymmetric force characteristic during the separation phase of the bumper from the mating surface (Krzyzynski *et al.*, 2019).

2.2.3. Damper force

The damping force generated by the hydraulic damper is described using a model based on flow losses of the working fluid through a throttling orifice. The value of the damping force F_{dz} depends on the direction of flow (chamber $B \to A$ or $A \to B$) as well as on the relative velocity of the piston with respect to the base, which corresponds to the forced oil flow velocity inside the damper. It is assumed that for a positive relative velocity $\dot{q}_{1z} - \dot{q}_{sz} > 0$, the fluid flows from chamber B to chamber A, whereas for $\dot{q}_{1z} - \dot{q}_{sz} < 0$, the flow occurs from chamber A to chamber B. The damper force is expressed by the following relationship:

$$\begin{aligned} F_{dz} &= \zeta_{B\to A} \cdot \rho_0/2 \cdot (A_B v/A_0)^2 \cdot A_B && \text{for} \quad v > 0, \\ F_{dz} &= -\zeta_{A\to B} \cdot \rho_0/2 \cdot (A_A v/A_0)^2 \cdot A_A && \text{for} \quad v < 0, \end{aligned} \tag{2.6}$$

where $v = \dot{q}_{1z} - \dot{q}_{sz}$ and the minus sign in the second case ensures that the damping force acts in the direction opposite to the motion, i.e., the force always acts as a resistance to the flow of kinetic energy in the system:

$$\begin{aligned} -\zeta_{(B\to A)} &= 64/\mathrm{Re}_{(B\to A)} \cdot (\alpha_o + l_o/d_o) && \text{for} \quad 64/\mathrm{Re}_{(B\to A)} \cdot (\alpha_o + l_o/d_o) > 1.8, \\ -\zeta_{(B\to A)} &= 1.8 && \text{for} \quad 64/\mathrm{Re}_{(B\to A)} \cdot (\alpha_o + l_o/d_o) \le 1.8, \\ -\zeta_{(A\to B)} &= 64/\mathrm{Re}_{(A\to B)} \cdot (\alpha_o + l_o/d_o) && \text{for} \quad 64/\mathrm{Re}_{(A\to B)} \cdot (\alpha_o + l_o/d_o) > 1.8, \\ -\zeta_{(A\to B)} &= 1.8 && \text{for} \quad 64/\mathrm{Re}_{(A\to B)} \cdot (\alpha_o + l_o/d_o) \le 1.8. \end{aligned} \tag{2.7}$$

The coefficients $\zeta_{(B\to A)}$ and $\zeta_{(A\to B)}$ describe flow losses depending on the flow regime (laminar or turbulent) and are expressed as functions of the Reynolds number. In the model, a Reynolds-number-dependent formulation was adopted with a lower bound of $\zeta = 1.8$, which ensures numerical stability and represents the minimum level of flow losses. The Reynolds numbers for both flow directions were determined using the following relations:

$$\mathrm{Re}_{(B->A)} = \frac{4[A_B(\dot{q}_{1z} - \dot{q}_{sz})]}{d_o \pi v_o}, \qquad \mathrm{Re}_{(A->B)} = \frac{4[A_A(\dot{q}_{1z} - \dot{q}_{sz})]}{d_o \pi v_o}. \tag{2.8}$$

The adopted formulation enables the inclusion of the nonlinear dependence of the damping force on the relative velocity (quadratic velocity term in the dynamic component) as well as the influence of flow regime transitions through the function $\zeta(\mathrm{Re})$. Consequently, the model reproduces the typical behavior of hydraulic dampers, characterized by relatively low damping forces at small velocities and a rapidly increasing flow resistance at higher velocities, which is particularly important for the attenuation of vibrations with higher dynamic intensity (Krzyzynski *et al.*, 2019).

2.2.4. Friction force

Friction phenomena in the system were described using an extended Stribeck model with a Coulomb friction term, which enables a smooth transition from static to dynamic friction and eliminates discontinuities at velocities close to zero:

$$F_{fz} = \sqrt{2\mathrm{e}(F_{brk} - F_c)} \cdot \exp\left(-\left(\frac{q_{1z} - q_{sz}}{V_{\mathrm{st}}}\right)2\right) \cdot \frac{q_{1z} - q_{sz}}{V_{\mathrm{st}}} + F_c \cdot \tanh\left(\frac{q_{1z} - q_{sz}}{V_{\mathrm{coul}}}\right), \tag{2.9}$$

where F_{brk} denotes the maximum static friction force, F_c represents the dynamic (Coulomb) friction force, and V_{st} and V_{coul} are characteristic velocities describing the transition between static and dynamic friction states. The application of this model enables an accurate representation of micro-scale friction phenomena occurring in the guides and articulated joints of the child safety seat, which has a significant influence on the attenuation of low-amplitude vibrations (Krzyzynski *et al.*, 2019).

3. Influence of selected model parameters on changes in the viscoelastic characteristics of the suspension system

As a part of the conducted analyses, the influence of key structural parameters of passive components on the viscoelastic characteristics of the passive suspension system of a child safety seat was investigated. For this purpose, four decision variables were defined as follows: the spring wire diameter $d_s = 0.5\,\text{mm}$ to $3\,\text{mm}$, the bumper activation parameter $\delta = -15\,\text{mm}$ to $5\,\text{mm}$, the damper orifice diameter $d_o = 0.5\,\text{mm}$ to $5\,\text{mm}$, and the dynamic friction force $F_c = 12\,\text{N}$ to $50\,\text{N}$. For each of these parameters, force–displacement or force–velocity characteristics were generated (Fig. 2 to Fig. 5), which enabled an assessment of their influence on the dynamic properties of the system and the identification of parameters with the greatest significance for vibration isolation effectiveness.

The analysis of the first parameter (Fig. 2), namely the spring wire diameter $d_s = 0.5\,\text{mm}$ to $3\,\text{mm}$, has shown that variations in this dimension have a pronounced effect on the stiffness characteristic. In accordance with helical spring theory, the stiffness increases proportionally to the fourth power of the wire diameter, which is clearly reflected in the obtained results. With increasing d_s, a monotonic increase in the slope of the force–displacement characteristic is observed, corresponding to a substantial increase in spring stiffness. This leads to a reduction in the relative displacement of the suspended mass. However, it simultaneously results in increased transmission of low-frequency vibrations. Lower values of the spring wire diameter d_s improve vibration comfort by increasing the system's ability to reduce acceleration levels. However, this improvement is achieved at the expense of a higher risk of reaching the allowable limits of relative displacement. Therefore, the range $d_s = 0.5\,\text{mm}$ to $3\,\text{mm}$ was selected as a decision variable in the optimization process, enabling precise tuning of the system stiffness.

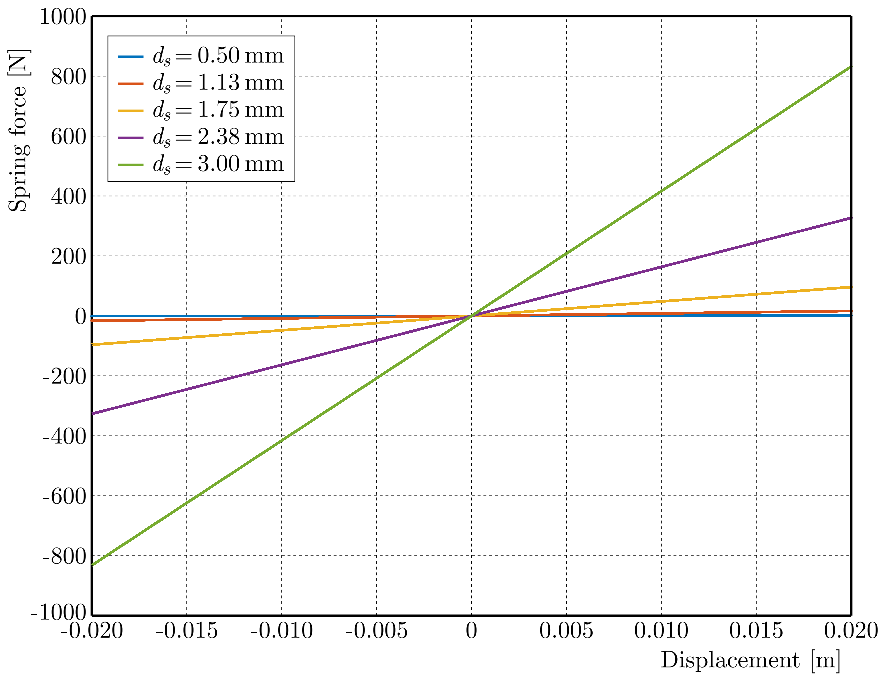

Fig. 2. Spring characteristic for different d_s.

The next analyzed component was the end-stop bumper (Fig. 3), for which the influence of the activation parameter $\delta = -15\,\text{mm}$ to $5\,\text{mm}$, governing the onset of contact between the suspended mass and the travel limiter, was evaluated. The bumper characteristic consists of a no-contact region, a linear force growth region, and a dynamically increasing nonlinear region. The analysis has confirmed that more negative values of δ delay the onset of force generation by

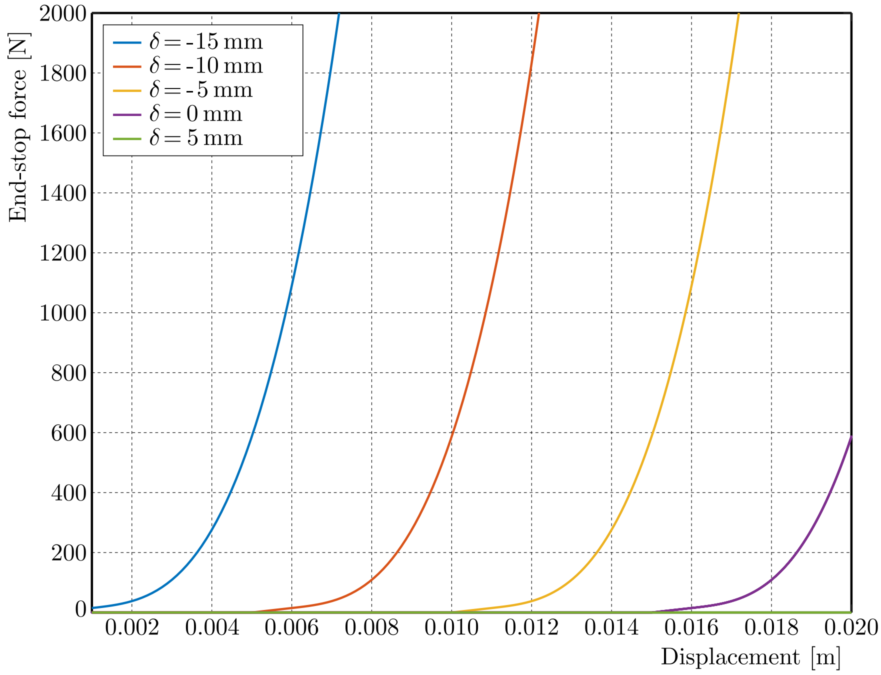

Fig. 3. End-stop bumper characteristic for different δ.

the bumper, thereby increasing the effective linear operating range of the entire suspension system. As a result, the system becomes more compliant for small displacements, which improves its vibration isolation properties in the low-frequency range. Once the activation threshold determined by $\delta = -15$ mm to 5 mm is exceeded, a rapid increase in stiffness is observed, providing protection against excessive deflection and contact with structural constraints. This behavior is consistent with that of real elastomeric bumpers, in which an intentional initial assembly clearance is commonly applied.

The influence of the damper orifice diameter $d_o = 0.5$ mm to 5 mm (Fig. 4) was analyzed with respect to the hydraulic damper characteristics. The obtained force–velocity curves clearly

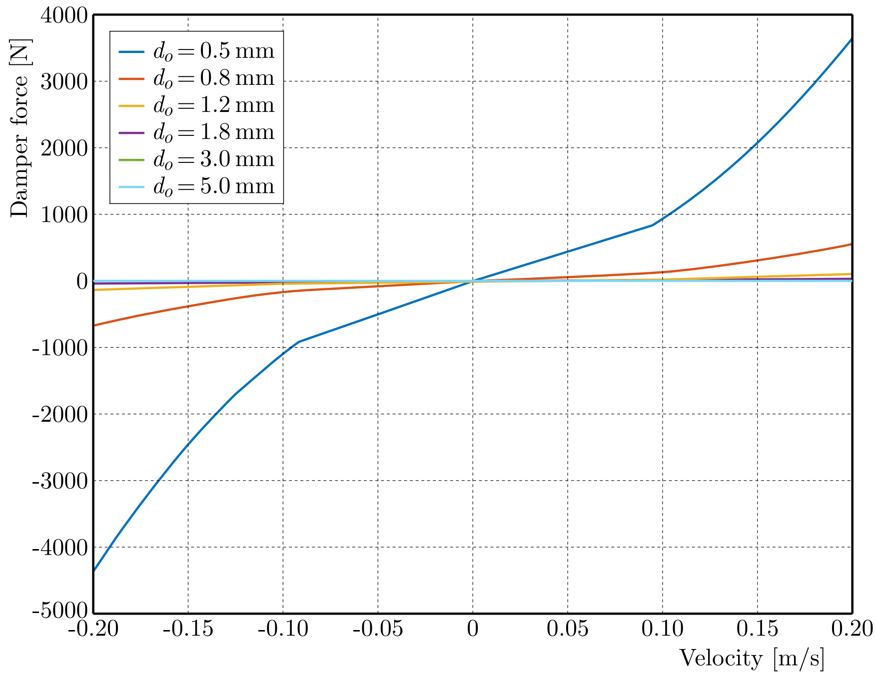

Fig. 4. Damper characteristic for different d_o.

indicate a strong nonlinear dependence of the damping force on the relative piston velocity. A reduction in d_o leads to a significant increase in fluid flow resistance and, consequently, to higher damping forces, particularly in the velocity range corresponding to the transition from laminar to turbulent flow. This behavior confirms the correct representation of the damper in the mathematical model, as real hydraulic dampers exhibit a similar increase in force as a function of velocity. Higher damping forces improve the attenuation of vibrations in the medium- and high-frequency ranges. However, an excessive flow resistance resulting from small orifice diameters within the range $d_o = 0.5$ mm to 5 mm leads to an increase in the dynamic stiffness of the system, which may deteriorate comfort under large-amplitude excitations.

The final analyzed parameter was the dynamic friction force (Fig. 5), $F_c = 12$ N to 50 N, describing friction characteristics in the system guides and modeled using the extended Stribeck formulation. The force–velocity relationship showed that increasing F_c enhances low-velocity damping, which plays an important role in stabilizing motion under small excitations. Higher values of F_c, including the range $F_c = 12$ N to 50 N considered in the analysis, reduce the amplitude of free oscillations and limit vibrations occurring near the static equilibrium position. At the same time, excessive friction promotes the occurrence of stick-slip phenomena, leading to abrupt displacement changes and increased vibration transmission within certain frequency bands. For this reason, the selection of F_c constituted a key stage of the subsequent optimization process, enabling a compromise between motion stabilization and smooth system operation.

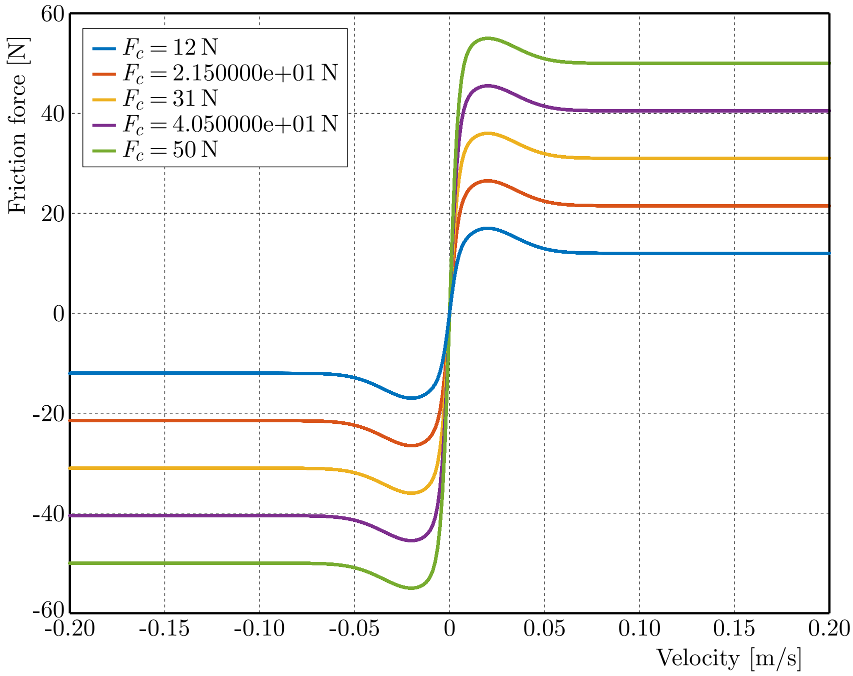

Fig. 5. Friction force characteristic as a function of velocity for different F_c.

The analysis of the four model parameters has clearly demonstrated that each of them has a significant influence on the resulting dynamic properties of the passive system. The spring wire diameter d_s determines the fundamental stiffness of the system, the parameter δ controls the transition to the nonlinear operating regime of the end stop, the orifice diameter d_o governs the viscous damping characteristics, while the friction force F_c is responsible for low-velocity damping and motion stability. Understanding the interaction of these parameters provides the basis for the appropriate selection of passive component properties and enables an effective optimization of the system with respect to minimizing the SEAT factor and limiting the relative displacement RS (relative stroke).

4. Excitation signals and evaluation criteria

To evaluate the effectiveness of the proposed passive system, it was necessary to apply excitation signals representative of the real operating conditions of a child safety seat in a vehicle. In the numerical analyses, a time-domain signal with characteristics close to white noise in the frequency range from 0.5 Hz to 10 Hz was used, corresponding to the typical frequency band encountered during vehicle operation on uneven road surfaces. The spectrum of the signal, obtained from the power spectral density (PSD), confirms the broadband nature of the excitation and a relatively uniform loading of the system over the entire analyzed frequency range. The applied excitation signal corresponds to conditions commonly used in laboratory testing of child safety seats as well as in field experiments, while simultaneously enabling the identification of changes in the dynamic characteristics of the system resulting from variations in structural parameters (Fig. 6). Such a signal provides a good approximation of real random vertical vibrations and is widely used in the analysis of vibration isolation systems due to the absence of dominant frequencies that could bias the assessment of vibration transmissibility.

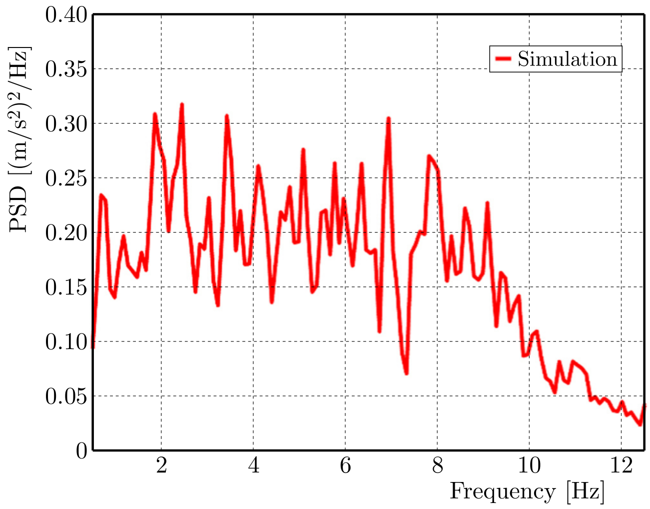

Fig. 6. Power spectral density of the excitation signal inducing vibratory motion.

The damping performance of the proposed system was evaluated using two indicators: the SEAT coefficient and the maximum relative displacement RS:

$$\mathrm{SEAT} = \frac{(q_{1z})_{\mathrm{RMS}}}{(q_{sz})_{\mathrm{RMS}}}. \tag{4.1}$$

The SEAT factor is a measure of the effective transmission of vibrations through the system and is defined as the ratio of the RMS value of the weighted acceleration on the isolated side to the corresponding value on the excitation side. The frequency weighting was selected in accordance with the recommendations of ISO 2631, enabling the consideration of the varying sensitivity of the human body to vibrations across different frequency bands. The SEAT index enables a direct assessment of vibration reduction in terms closely related to user comfort and is a standard analytical tool in studies of vibration isolation systems. Values of SEAT < 1 indicate an isolating effect of the system, whereas SEAT > 1 signify vibration amplification within specific frequency ranges. The second indicator used to evaluate system performance was the relative displacement RS, defined as the maximum positional difference between the isolated mass (the child safety seat and the child) and the excitation base:

$$\mathrm{RS} = \max_{t\in[0,tk]}\big(q_{1z(t)} - q_{sz(t)}\big) - \min_{t\in[0,tk]}\big(q_{1z(t)} - q_{sz(t)}\big). \tag{4.2}$$

The relative displacement RS was used as a structural safety indicator, defining the suspension travel required to avoid excessive loading of the end stops or contact with structural limits. The combined use of SEAT and RS enables the simultaneous evaluation of vibration comfort and safe operating range, which is essential in the optimization of passive vibration isolation systems.

5. Optimization of vibration isolation performance of the passive system and optimal characteristics of passive components

The optimization of the vibration isolation performance of the passive system was carried out using a deterministic full factorial parametric search. Four decision variables were considered: the spring wire diameter d_s, the bumper activation parameter δ, the hydraulic damper orifice diameter d_o, and the dynamic friction force F_c. Each variable was discretized into 15 equally spaced values within the adopted design range: $d_s = 0.5\,\text{mm}$ to $3\,\text{mm}$, $\delta = -15\,\text{mm}$ to $5\,\text{mm}$, $d_o = 0.5\,\text{mm}$ to $5\,\text{mm}$, and $F_c = 12\,\text{N}$ to $50\,\text{N}$. Consequently, 50 625 combinations of passive component parameters were analyzed.

For each parameter combination, a numerical simulation of the passive suspension system was performed in MATLAB/Simulink. The SEAT coefficient and the RS were calculated and stored as the evaluation criteria. The optimization problem was formulated as the simultaneous minimization of the SEAT coefficient, representing vibration transmission to the child's body, and the RS, representing the suspension travel required for safe operation. Since a deterministic full factorial search was used, no stochastic convergence criterion was required; the procedure was completed after all predefined parameter combinations had been evaluated. The Pareto-optimal solutions were selected from the complete set of admissible results. First, the solutions corresponding to the minimum SEAT value and the minimum RS value were identified. Then, ten constraint levels of RS were defined between these limiting cases. For each RS constraint, the solution with the lowest SEAT value was selected. This procedure resulted in a set of ten Pareto-optimal solutions representing different compromises between vibration isolation effectiveness and suspension travel limitation. The resulting Pareto-optimal solutions in the SEAT–RS evaluation criteria space are presented in Fig. 9. The spring characteristics obtained as a result of the optimization process (Fig. 7) indicate the necessity of achieving a compromise between

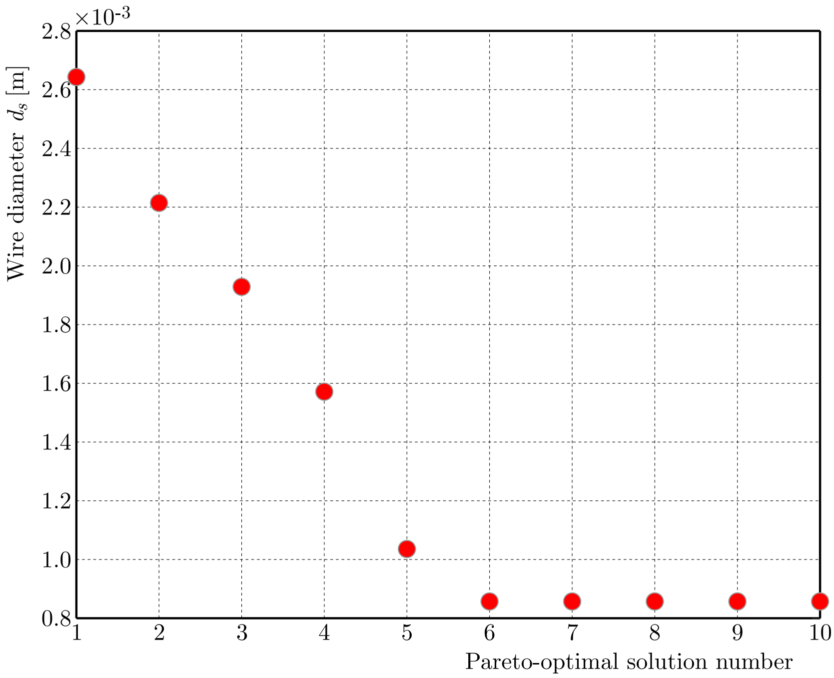

Fig. 7. Optimal characteristics of passive components – spring.

sufficiently low stiffness, which promotes the reduction of low-frequency vibrations, and adequate global system stiffness, which limits excessive relative displacements. In the case of the hydraulic damper (Fig. 11), the optimal parameter values lead to a nonlinear increase in the damping force with increasing relative motion velocity. This behavior is particularly advantageous, as it enables effective dissipation of vibration energy in the medium- and high-frequency ranges without causing excessive system stiffening during slow position changes. The optimized end-stop bumper characteristic (Fig. 10) allows for a delayed activation of the nonlinear portion of the limiter response, ensuring high compliance of the system in the range of small deflections. Only at larger displacements does the reaction force increase rapidly, effectively protecting the

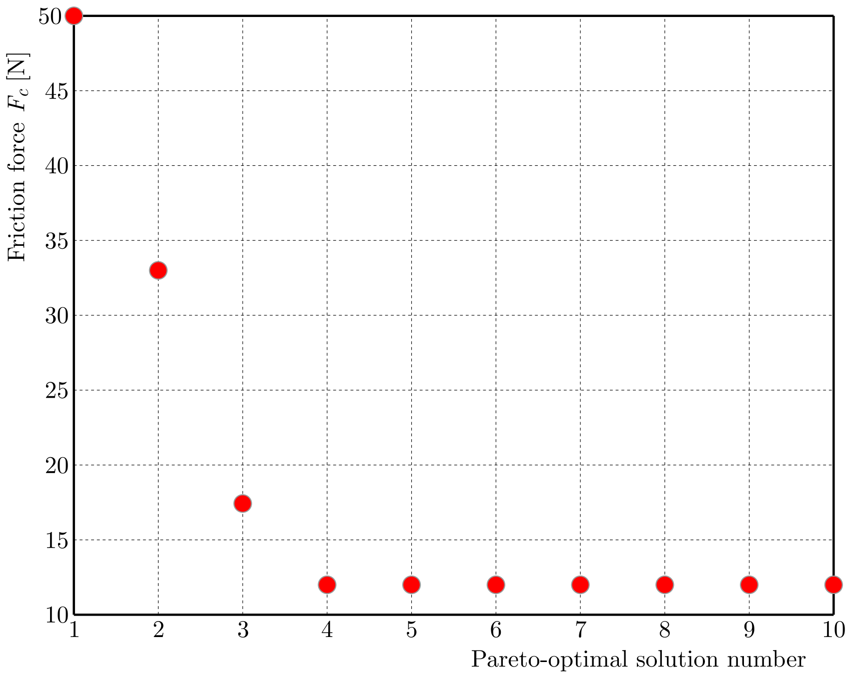

Fig. 8. Optimal characteristics of passive components – friction.

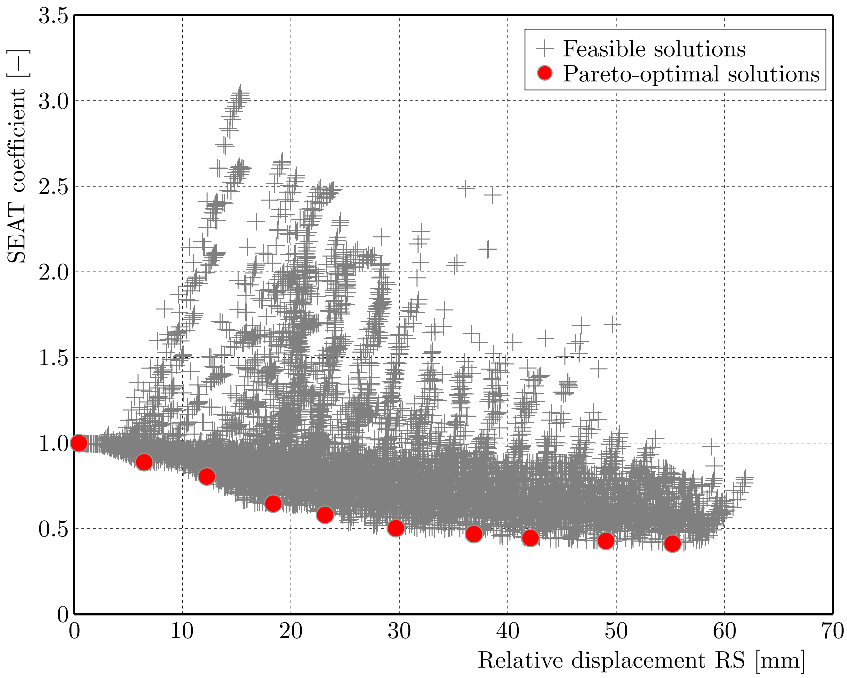

Fig. 9. Optimal characteristics of passive components – evaluation criteria space.

system against exceeding the allowable suspension travel. In turn, the appropriately selected value of the dynamic friction force (Fig. 8) provides motion stabilization at low velocities while simultaneously limiting the risk of stick-slip phenomena and the associated abrupt displacement changes. Such a friction damping characteristic supports effective attenuation in the low-velocity range and enhances the overall stability of the system. The frequency-domain results (Fig. 12) indicate a reduction in vibration transmissibility in the range of approximately 1 Hz to 10 Hz, which is particularly relevant for child comfort. For the selected optimal passive configuration, the SEAT coefficient was reduced to 0.47, while the RS remained equal to 36.8 mm. These values

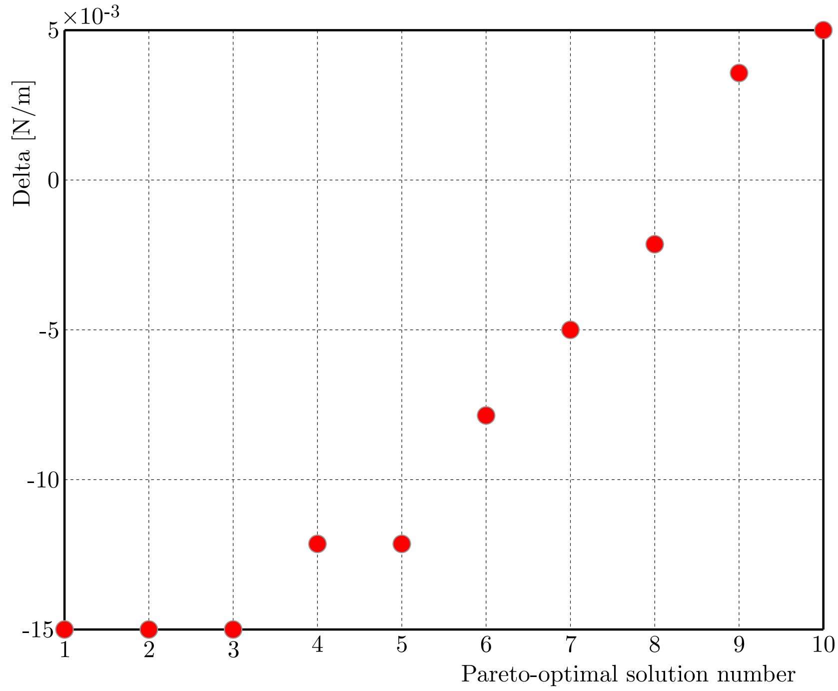

Fig. 10. Optimal characteristics of passive components – end-stop bumpers.

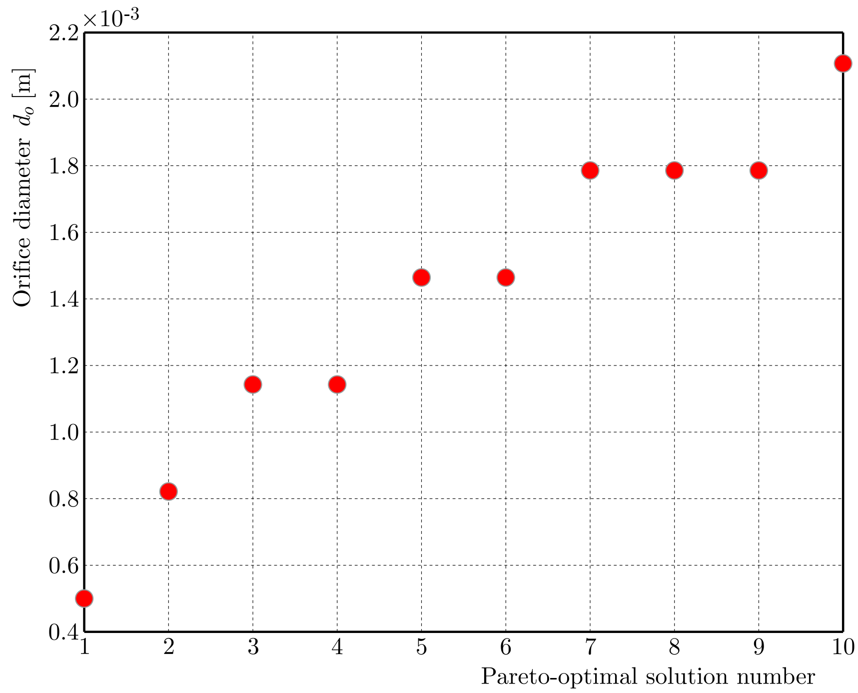

Fig. 11. Optimal characteristics of passive components – damper.

confirm that the optimized passive suspension system provides effective vibration attenuation while maintaining the required suspension travel within the admissible operating range. The resulting parameter set may serve as a reference point for further experimental validation and comparison with semi-active and active systems.

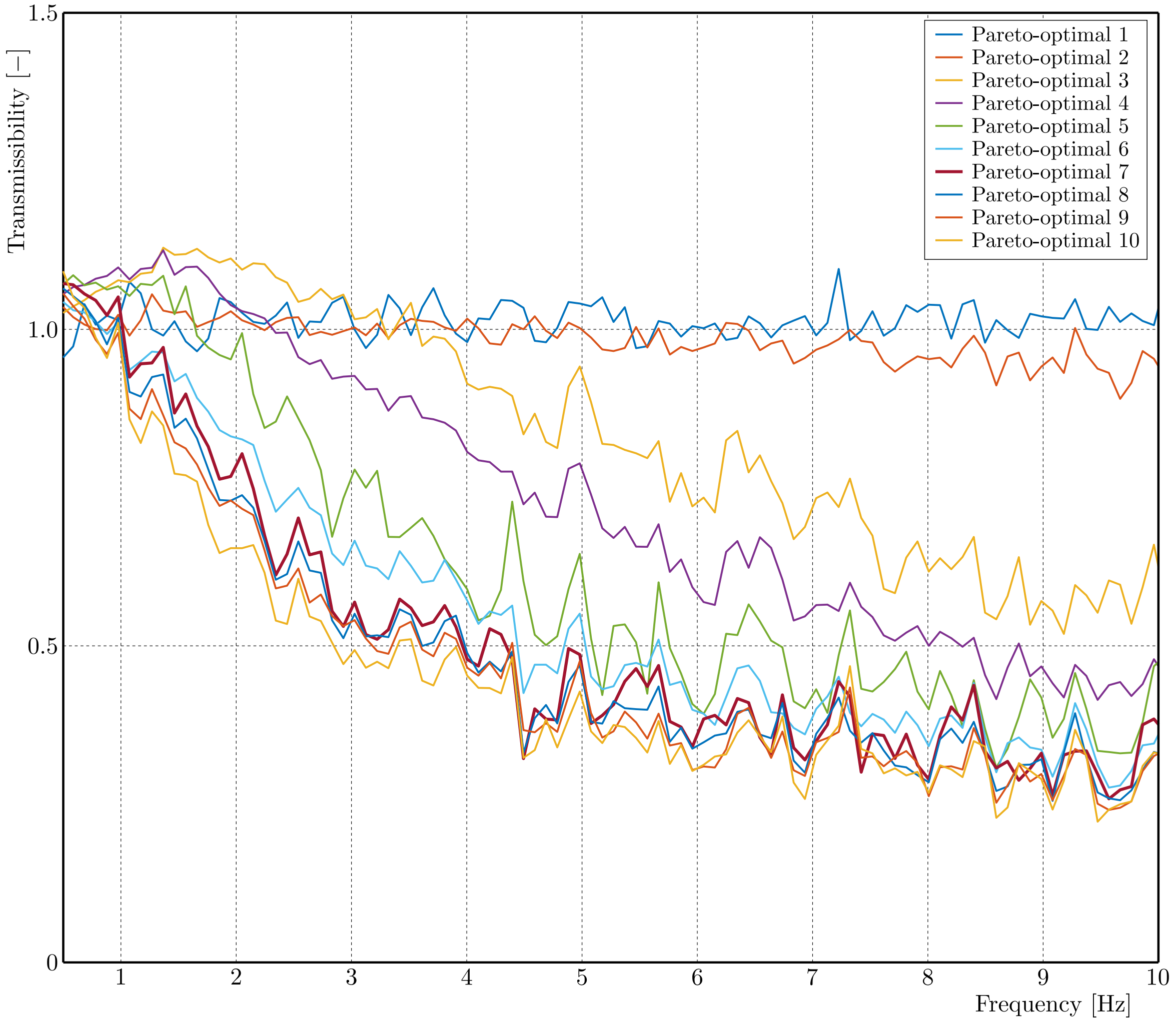

Fig. 12. Vibration transmissibility functions of selected Pareto-optimal solutions.

6. Conclusions

The conducted studies have confirmed that the dynamic response of the passive suspension system of a child safety seat depends mainly on the parameters related to elasticity, damping, and friction. The numerical model reproduced the behavior of elastic, damping, friction, and end-stop components, and the obtained force–displacement and force–velocity characteristics were consistent with the physical properties of these elements. The optimization of passive parameters resulted in a measurable improvement in vibration isolation performance. For the selected optimal passive configuration, the SEAT coefficient reached 0.47, while the RS was 36.8 mm. This confirms that the optimized passive system can reduce vibration transmission while maintaining the displacement of the suspended mass within a safe operating range. The present study was limited to numerical modeling, sensitivity analysis, and optimization. Future work will include field tests using an anthropomorphic dummy equipped with acceleration sensors to compare the numerical predictions with experimental measurements and to support the development of semi-active and active vibration isolation systems for child safety seats.

References

1. Alawneh, O., Zhong, X., Faieghi, R., & Xi, F. (2022). Finite element methods for modeling the pressure distribution in human body–seat interactions: A systematic review. *Applied Sciences*, *12*(12), Article 6160. https://doi.org/10.3390/app12126160

2. Bai, X.-X., Xu, S.-X., Cheng, W., & Qian, L.-J. (2017). On 4-degree-of-freedom biodynamic models of seated occupants: Lumped-parameter modeling. *Journal of Sound and Vibration*, *402*, 122–141. https://doi.org/10.1016/j.jsv.2017.05.018

3. Duda, S., Dudek, O., Gembalczyk, G., & Machoczek, T. (2020). Developing a test site for testing the suspension of vehicles with omnidirectional wheels. *Vibrations in Physical Systems*, *31*(3), 2020304-1–2020304-8. https://doi.org/10.21008/j.0860-6897.2020.3.04

4. Florek, N.J., & Maciejewski, I. (2025). The impact of vibrations on the comfort and safety of children in car seats: A review of current knowledge. *Vibrations in Physical Systems*, *36*(2), 2025211-1–2025211-8. https://doi.org/10.21008/j.0860-6897.2025.2.11

5. Frej, D. (2018). Influence of wheel imbalance on driver's vibration comfort – front and rear axle (in Polish). In M. Bogusz, M. Wojcieszak, & P. Rachwał (Eds.), *Poszerzamy Horyzonty* (Vol. IX, pp. 531–553). https://www.konferencjenaukowe.com.pl/monografia9.pdf

6. Frej, D., & Grabski, P. (2019). The impact of the unbalanced rear wheel on the vibrating comfort of the child seat. *Transportation Research Procedia*, *40*, 678–685. https://doi.org/10.1016/j.trpro.2019.07.096

7. Frej, D., & Grabski, P. (2023). Trends in choosing the right child seat – survey research. *Transportation Research Procedia*, *74*, 1308–1317. https://doi.org/10.1016/j.trpro.2023.11.276

8. Giacomin, J. (2000). Some observations regarding the vibrational environment in child safety seats. *Applied Ergonomics*, *31*(2), 207–215. https://doi.org/10.1016/s0003-6870(99)00034-4

9. Giacomin, J. (2004). Apparent mass of small children: experimental measurements. *Ergonomics*, *47*(13), 1454–1474. https://doi.org/10.1080/00140130412331290817

10. Giacomin, J. (2005). Absorbed power of small children. *Clinical Biomechanics*, *20*(4), 372–380. https://doi.org/10.1016/j.clinbiomech.2004.12.001

11. Gromadowski, T., & Więckowski, D. (2012). Analysis of vertical vibration affecting the child in a car with the use of the white noise signal input (in Polish). *Postępy Nauki i Techniki*, *14*, 83–94.

12. Hryciów, Z., Małachowski, J., Rybak, P., & Wiśniewski, A. (2021). Research of vibrations of an armoured personnel carrier hull with FE implementation. *Materials*, *14*(22), Article 6807. https://doi.org/10.3390/ma14226807

13. International Organization for Standardization. (1997). *Mechanical vibration and shock – Evaluation of human exposure to whole-body vibration. Part 1: General requirements* (ISO Standard No. 2631-1:1997). https://www.iso.org/standard/7612.html

14. International Organization for Standardization. (2001). *Mechanical vibration and shock – Evaluation of human exposure to whole-body vibration. Part 4: Guidelines for the evaluation of the effects of vibration and rotational motion on passenger and crew comfort in fixed-guideway transport systems* (ISO Standard No. 2631-4:2001). https://www.iso.org/standard/32178.html

15. International Organization for Standardization. (2018). *Mechanical vibration and shock – Evaluation of human exposure to whole-body vibration. Part 5: Method for evaluation of vibration containing multiple shocks* (ISO Standard No. 2631-5:2018). https://www.iso.org/standard/50905.html

16. Krzyzynski, T., Maciejewski, I., Meyer, L., & Meyer, H. (2019). *Modelling and control design of vibration reduction systems. Methods and procedures of selecting vibro-isolation properties.* Springer. https://doi.org/10.1007/978-3-030-03047-6

17. Łagoda, T. (2001). Energy models for fatigue life estimation under uniaxial random loading. Part I: The model elaboration. *International Journal of Fatigue*, *23*(6), 467–480. https://doi.org/10.1016/S0142-1123(01)00016-0

18. Maciejewski, I., Zlobinski, M., Krzyzynski, T., & Glowinski, S. (2020). Vibration control of an active horizontal seat suspension with a permanent magnet synchronous motor. *Journal of Sound and Vibration*, *488*, Article 115655. https://doi.org/10.1016/j.jsv.2020.115655

19. Nilsson, M. (2005). Health risk aspects and comfort for infants in infant seats for cars. *VTI Notat 24-2005. Swedish National Road and Transport Research Institute (VTI).*

20. Wicher, J., & Więckowski, D. (2010). Influence of vibrations of the child seat on the comfort of child's ride in a car. *Eksploatacja i Niezawodność – Maintenance and Reliability*, *4*, 102–110.

21. Zhang, X., Qiu, Y., & Griffin, M.J. (2015). Developing a simplified finite element model of a car seat with occupant for predicting vibration transmissibility in the vertical direction. *Ergonomics*, *58*(7), 1220–1231. https://doi.org/10.1080/00140139.2015.1005165

22. Zuska, A., Szumska, E., & Frej, D. (2021). Laboratory tests of the control of the child seats using method for the vibration comfort of children transported in them. *Communications – Scientific Letters of the University of Zilina*, *23*(3), B187–B199. https://doi.org/10.26552/com.C.2021.3.B187-B199

Manuscript received April 1, 2026; accepted for publication July 4, 2026;
published online September 1, 2026.

JOURNAL OF THEORETICAL
AND APPLIED MECHANICS
64, 3, pp. 217–229, Warsaw 2026
https://doi.org/10.15632/jtam-pl/225130

HYDROMECHANICAL DEGRADATION AND FATIGUE-LIKE DAMAGE MECHANISM OF SATURATED RED SANDSTONE SUBJECTED TO CYCLIC PORE-WATER PRESSURE

Wenjun ZHONG[1], Junzhe XU[2*], Ningbo HE[1]

[1] *China Anergy Group Third Engineering Bureau Co. Ltd., Chengdu, China*
[2] *School of Civil and Hydraulic Engineering, Chongqing University of Science and Technology, Chongqing, China*
[*]corresponding author, *2024206032@cqust.edu.cn*

Triaxial tests under 2 MPa confinement investigated saturated red sandstone degradation under cyclic pore-water pressure. A 0.3 MPa cyclic pressure reduces peak strength by 18.3 %. Deformation remains stable below 70 % of peak strength. Conversely, unstable fatigue damage accelerates post-eight cycles at 80 % stress. These results elucidate hydromechanical fatigue mechanisms, improving reservoir slope stability evaluations.

Keywords: saturated red sandstone; cyclic pore-water pressure; hydromechanical coupling; fatigue-like damage; energy dissipation.

1. Introduction

The long-term stability of reservoir bank slopes is a critical determinant for the safety of large-scale hydraulic infrastructure, such as the Three Gorges Reservoir (TGR) area in China (Yang *et al.*, 2025; He *et al.*, 2020). Unlike typical engineered slopes, reservoir banks are subjected to periodic water-level fluctuations driven by seasonal regulation and flood control operations. These fluctuations inevitably induce cyclic variations in the pore-water pressure within the submerged rock mass (Liao *et al.*, 2025). According to the principle of effective stress (Terzaghi, 1943), such hydraulic perturbations dynamically alter the stress state of the rock framework, acting as a recurring internal load. Distinct from external mechanical cyclic loading, this process is now recognized as a primary driver of hydraulic fatigue (Li *et al.*, 2023; Hu *et al.*, 2023). Such progressive deterioration continuously threatens the structural durability of bank slope rock masses.

Extensive research has established that water weakens sandstone through physical and chemical processes, such as the reduction of cementation strength, alteration of mineral surfaces, and promotion of subcritical crack growth (Wang *et al.*, 2026; Li *et al.*, 2025; Xu *et al.*, 2022). However, most existing studies have focused on two specific conditions:

1) monotonic water-weakening (Xuan *et al.*, 2025; Liang *et al.*, 2024), in which the degradation is time-dependent under constant hydraulic conditions,
2) dry-wet cycling (Wang *et al.*, 2023; Taheri *et al.*, 2016), which simulates the long-term weathering process over months or years.

While these studies explain long-term softening, they fail to capture the short-term, fatigue-like damage induced by frequent, transient pore-pressure pulses occurring within the rock mass while it sustains high gravitational shear stresses.

Recent investigations into hydraulic fracturing and deep-earth engineering have touched upon the effects of cyclic hydraulic pressure. For instance, Kendrick *et al.* (2024) and Chang *et al.* (2022) reported that cyclic pressurization accelerates microcrack initiation and alters failure modes. Similarly, energy-based analyses have highlighted that water–rock interaction enhances energy dissipation and localization during cyclic loading (Sun *et al.*, 2024; Li *et al.*, 2020). Nevertheless, a critical gap remains in the context of reservoir slope engineering. Most prior experiments utilized extremely high hydraulic pressures (aimed at fracturing) or focused on permeability evolution alone. The mechanisms by which low amplitude cyclic pore pressure couples with high static axial stress to induce fatigue failure remain systematically unexplored. These low amplitude cycles accurately reflect realistic reservoir fluctuations. Furthermore, the critical stress threshold governing the transition from stable deformation to unstable hydraulic damage requires deeper investigation (Sawicki & Mierczyński, 2015).

To bridge this gap, this study investigates the hydromechanical degradation of saturated red sandstone from the TGR area. The experimental design strictly mimics the in situ stress and hydraulic conditions of shallow landslides in the TGR: a constant confining pressure of 2 MPa (simulating the overburden stress of a shallow sliding mass) and a cyclic pore-water pressure amplitude of 0.3 MPa (corresponding to the 30 m annual water-level regulation). By conducting triaxial compression tests combined with 20-cycle pore-pressure loading, this work aims to:

1) quantify the short-term strength reduction induced by reservoir-scale hydraulic fluctuations,
2) characterize the transition of deformation behaviors from stable hysteresis to nonlinear accumulation,
3) establish a residual-strain-based damage variable to elucidate the stress-dependent evolution mechanism.

The findings provide new theoretical insights into the “hydraulic fatigue” of reservoir rocks and offer a rigorous basis for evaluating the stability of bank slopes under complex hydromechanical coupling.

2. Materials and methods

2.1. Specimen preparation

The red sandstone blocks utilized in this study were collected from the hydro-fluctuation belt of the TGR area. The natural rock is characterized by a massive structure and a uniform dark red texture. All test specimens were cored from a single intact rock block to maximize initial material consistency. These cores were subsequently processed into standard cylinders with a diameter of 50 mm and a height of 100 mm (as shown in Fig. 1). This preparation strictly adhered to the guidelines established by the International Society for Rock Mechanics (ISRM) (Ulusay & Hudson, 2007). The machining precision was rigorously controlled to restrict diameter

Fig. 1. Red sandstone specimens processed into standard cylinders (50 mm × 100 mm) (He *et al.*, 2026).

deviation within 0.3 mm and limit end face non-parallelism to under 0.05 mm. Prior to testing, all specimens were oven-dried at 105 °C for 24 h to eliminate initial moisture content. Subsequently, the saturation process was conducted using the boiling-water saturation method for 48 h to ensure full saturation. Ultrasonic P wave velocity measurements and bulk density evaluations were conducted on all prepared dry specimens. Only those specimens exhibiting a P wave velocity deviation of less than three percent and nearly identical bulk densities were selected for the final testing phase. A subsequent boiling water saturation method was applied for 48 h to ensure complete fluid saturation before the triaxial loading.

2.2. Testing apparatus

Hydromechanical coupling tests were performed using the TFD-2000 microcomputer servo-controlled rock triaxial testing system. This high-stiffness apparatus is capable of independently controlling axial stress, confining pressure, and pore-water pressure. It has a maximum axial load capacity of 2000 kN and a maximum confining pressure of 140 MPa. The control precision is ±0.5 % for axial load and ±0.1 % for pore-water pressure. A high-speed data acquisition system recorded the axial stress, strain, and pore-water pressure synchronously at a sampling rate of 10 Hz, ensuring sufficient resolution to capture the deformation response during rapid hydraulic loading phases.

2.3. Experimental procedure

The testing protocol was designed to simulate the in situ stress conditions of reservoir bank slopes subjected to water-level fluctuations. The cyclic water pressure amplitude was set to 0.3–0 MPa, corresponding to the 30 m seasonal water-level regulation (175 m to 145 m) in the TGR. The specific testing stages were as follows (see Fig. 2):

1) A hydrostatic confining pressure σ_3 of 2 MPa was applied at a rate of 5 MPa/min to simulate the overburden pressure of a shallow landslide mass.
2) With the confining pressure held constant, the axial stress (σ_1) was loaded at 5 MPa/min to a target level. Three target stress levels were selected: 27.41 MPa, 31.98 MPa, and 36.55 MPa, corresponding to 60 %, 70 %, and 80 % of the saturated peak strength $\sigma_{\text{peak}}^{\text{sat}} =$ 45.69 MPa determined under a constant pore pressure of 0.3 MPa.
3) Under constant axial and confining stresses, a triangular waveform was employed to alternate the water pressure between 0 Mpa and 0.3 MPa at a rate of 0.01 MPa/min, simulating the water level dropping from 175 m to 145 m and then recovering to 175 m. This cycle was repeated 20 times for each specimen to evaluate fatigue-like degradation behavior.

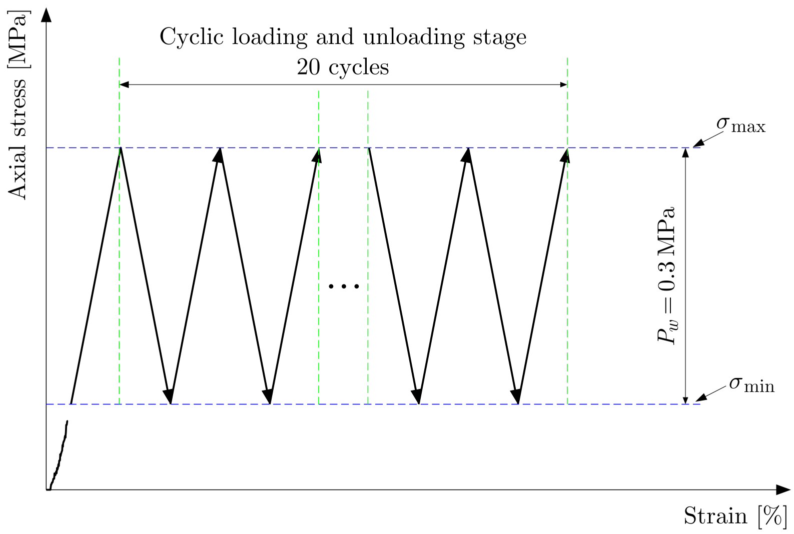

Fig. 2. Schematic diagram of the stress path and cyclic water pressure loading scheme.

3. Test results and analysis

3.1. Degradation of short-term mechanical properties

To establish a baseline for cyclic testing, the mechanical response of the red sandstone was first evaluated under monotonic triaxial compression at a confining pressure of 2 MPa. Figure 3 compares the stress-strain behavior between the dry ($P_w = 0$ MPa) and saturated-pressurized ($P_w = 0.3$ MPa) states.

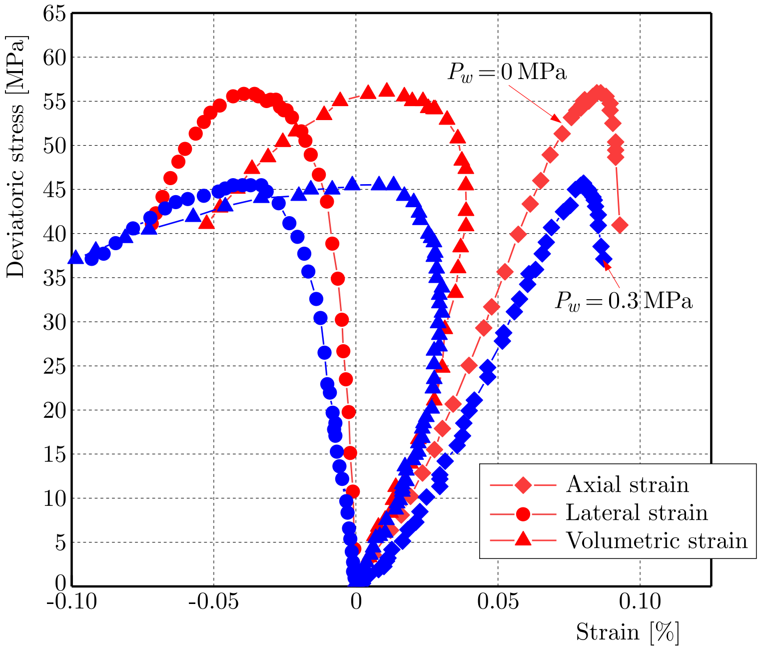

Fig. 3. Comparison of stress–strain curves for red sandstone under dry state ($P_w = 0$ MPa) and saturated-pressurized state ($P_w = 0.3$ MPa) (He *et al.*, 2026).

The intrusion of 0.3 MPa pore water pressure significantly degrades the mechanical competence of the rock. The peak compressive strength declines from 55.94 MPa to 45.69 MPa representing an 18.3 % reduction. Following the effective stress principle, the applied pore pressure counteracts the confining pressure. This interaction reduces the effective normal stress on potential failure planes and lowers the frictional resistance against shear sliding. Furthermore, the elastic modulus decreases by approximately 19 % from 22.5 GPa to 18.2 GPa. The softening indicates that water infiltration weakens the intergranular clay cementation and lubricates the grain boundaries. Additionally, the onset of dilatancy shifts from approximately 40 MPa down to 32 MPa. This critical threshold marks the initiation of unstable microcrack propagation. Consequently, the reduction significantly narrows the safe stress window for the rock mass under hydromechanical coupling.

3.2. Deformation evolution under cyclic hydraulic loading

Based on the hysteresis loops (Fig. 4) and cumulative residual strain curves (Fig. 5), the axial deformation under cyclic pore-water pressure exhibits three distinct, stress-dependent regimes:

1) Elastic shakedown regime (60 % σ_{sat}, 27.41 MPa): at this lower stress level, internal microcracks remain in a stable "breathing" state. The near-zero cumulative residual strain confirms that a 0.3 MPa hydraulic perturbation cannot overcome the frictional resistance provided by the 2 MPa confinement.
2) Plastic shakedown regime (70 % σ_{sat}, 31.98 MPa): deformation enters a self-limiting phase. The initial rapid strain accumulation (due to internal pore compaction) transitions

into a stable plateau (Fig. 5). The confining matrix effectively arrests subsequent crack propagation, leading to decreasing hysteresis loop widths (Fig. 4) as the microstructure stabilizes.

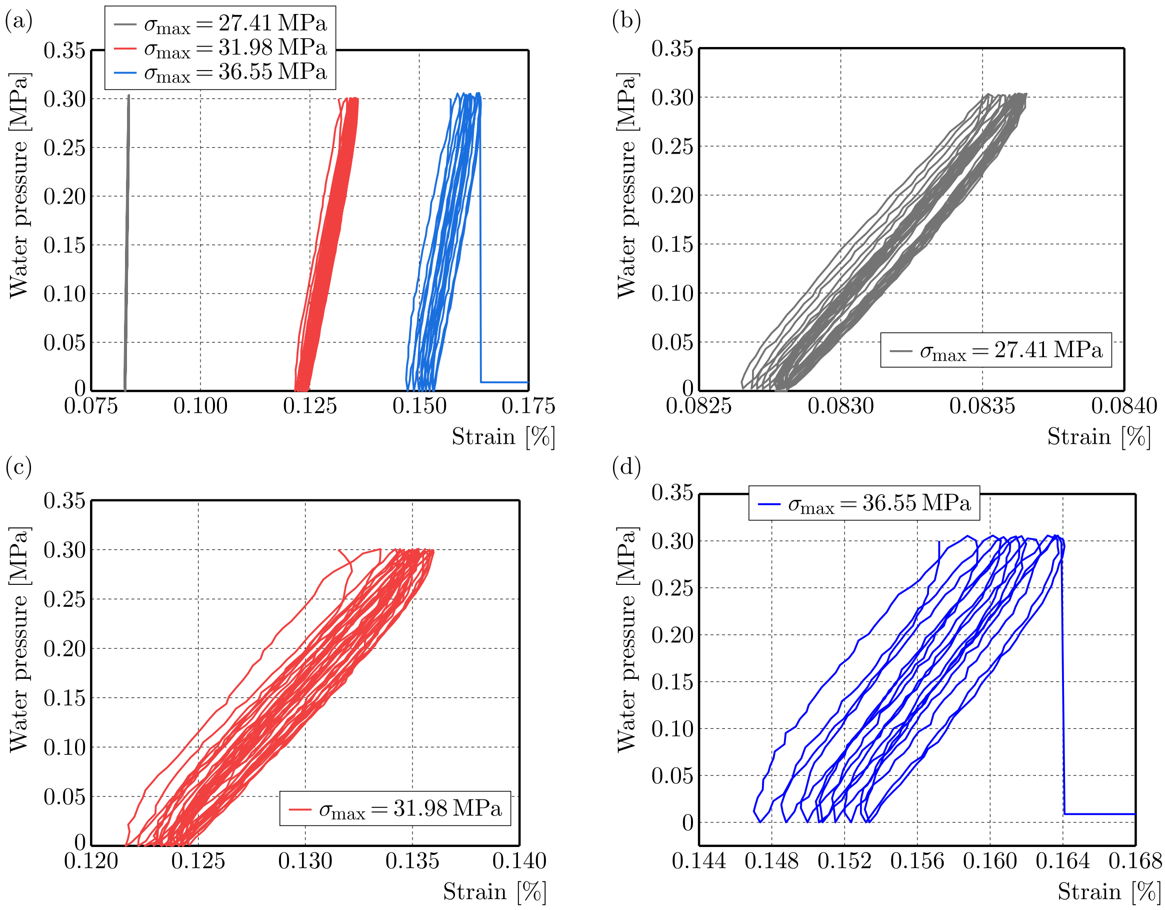

Fig. 4. Axial strain and water pressure hysteresis loops under different static axial stress levels: (a) comparative hysteresis loops; (b) 60 % of saturated peak strength 27.41 MPa; (c) 70 % of saturated peak strength 31.98 MPa; (d) 80 % of saturated peak strength 36.55 MPa.

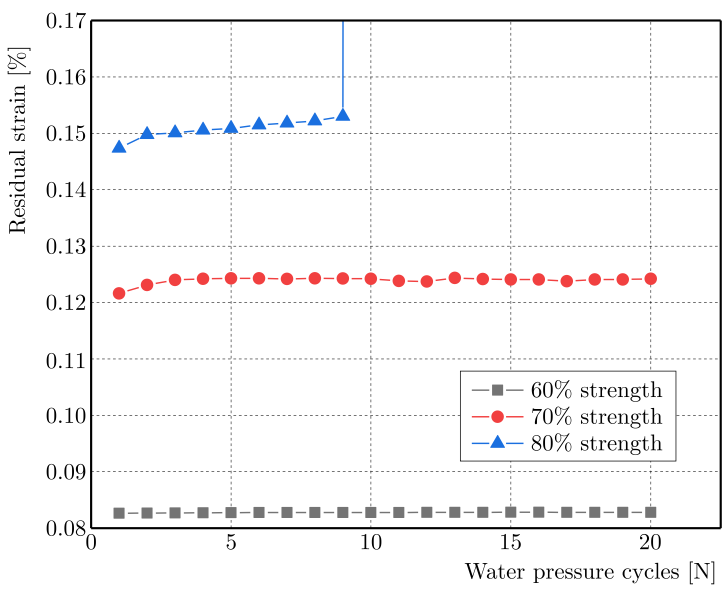

Fig. 5. Accumulation evolution of residual axial strain versus the number of pore-water pressure cycles.

3) Ratcheting and acceleration regime (80 % σ_{sat}, 36.55 MPa): approaching the dilatancy boundary, the rock transitions toward a runaway failure mode dominated by ratcheting. Hysteresis loops progressively widen and shift continuously (Fig. 4). The residual strain follows a classic three-stage fatigue trajectory, experiencing a sharp nonlinear acceleration after a critical threshold (cycles 8–10), ultimately reaching over twice the magnitude observed at the 60 % stress level by the 12th cycle.

To facilitate a clear comparison, the key experimental parameters and corresponding deformation regimes under various static stress levels are quantitatively summarized in Table 1.

Table 1. Summary of hydromechanical test parameters and resultant deformation regimes.

Axial stress level	Absolute axial stress [MPa]	Hydraulic cyclic amplitude [MPa]	Confining pressure [MPa]	Critical cycle to acceleration	Dominant deformation regime
60 % σ_{sat}	27.41	0↔0.3	2	N/A (stable)	Elastic shakedown
70 % σ_{sat}	31.98	0↔0.3	2	N/A (plateau)	Plastic shakedown
80 % σ_{sat}	36.55	0↔0.3	2	Cycles 8–10	Ratcheting

4. Energy dissipation characteristics

4.1. Calculation of energy components

Rock deformation under cyclic loading is thermodynamically an irreversible process involving energy input, accumulation, and dissipation. Based on the principle of energy conservation, the total input energy density (U) during a single loading-unloading cycle can be decomposed into elastic strain energy density (U^e) and dissipated energy density (U^d):

$$U = U^e + U^d. \tag{4.1}$$

As illustrated in Fig. 6, U corresponds to the area under the loading curve (area ABCF $= \text{S}_1 + \text{S}_2 + \text{S}_3$), representing the total work done by the external stress field. U^e corresponds to the area under the unloading curve (area EDCF $= \text{S}_2$), representing the recoverable elastic potential energy stored in the rock matrix. Consequently, the dissipated energy density U^d, which accounts for irreversible damage (e.g., microcrack propagation and frictional sliding), is calculated as the area of the hysteresis loop (area ABCDE $= \text{S}_1 + \text{S}_3$).

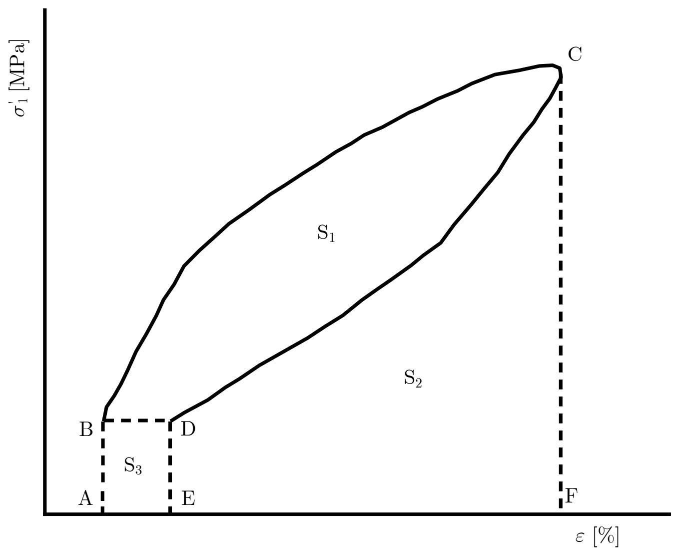

Fig. 6. Schematic diagram illustrating the calculation of elastic energy density (U^e) and dissipated energy density (U^d) from the hysteresis loop (Zhao *et al.*, 2020).

4.2. Evolution patterns of dissipated energy

The evolution of dissipated energy density (U^d) versus cycle number (Fig. 7) is strictly governed by the applied stress level, displaying a transition from two-stage to three-stage behavior:

1) Phase I: rapid adaptation (all stress levels): cycles 1–5 show a sudden drop in U^d due to a hydromechanical compaction effect, where initial pore-pressure cycles close pre-existing voids and stiffen the rock skeleton.
2) Phase II: stable dissipation (all stress levels): following initial decay, energy dissipation stabilizes. For $\sigma \leq \sigma_{\text{sat}}$, U^d remains low and constant, consumed purely by reversible friction along closed crack surfaces without new macroscopic damage.
3) Phase III: accelerated damage (only for 80% σ_{sat}): after the 8th–10th cycle, the U^d curve uniquely turns upward at the 80% stress level. This "U-shaped" surge indicates that energy input now exceeds the frictional dissipation capacity, driving irreversible microcrack coalescence and progressive fatigue failure.

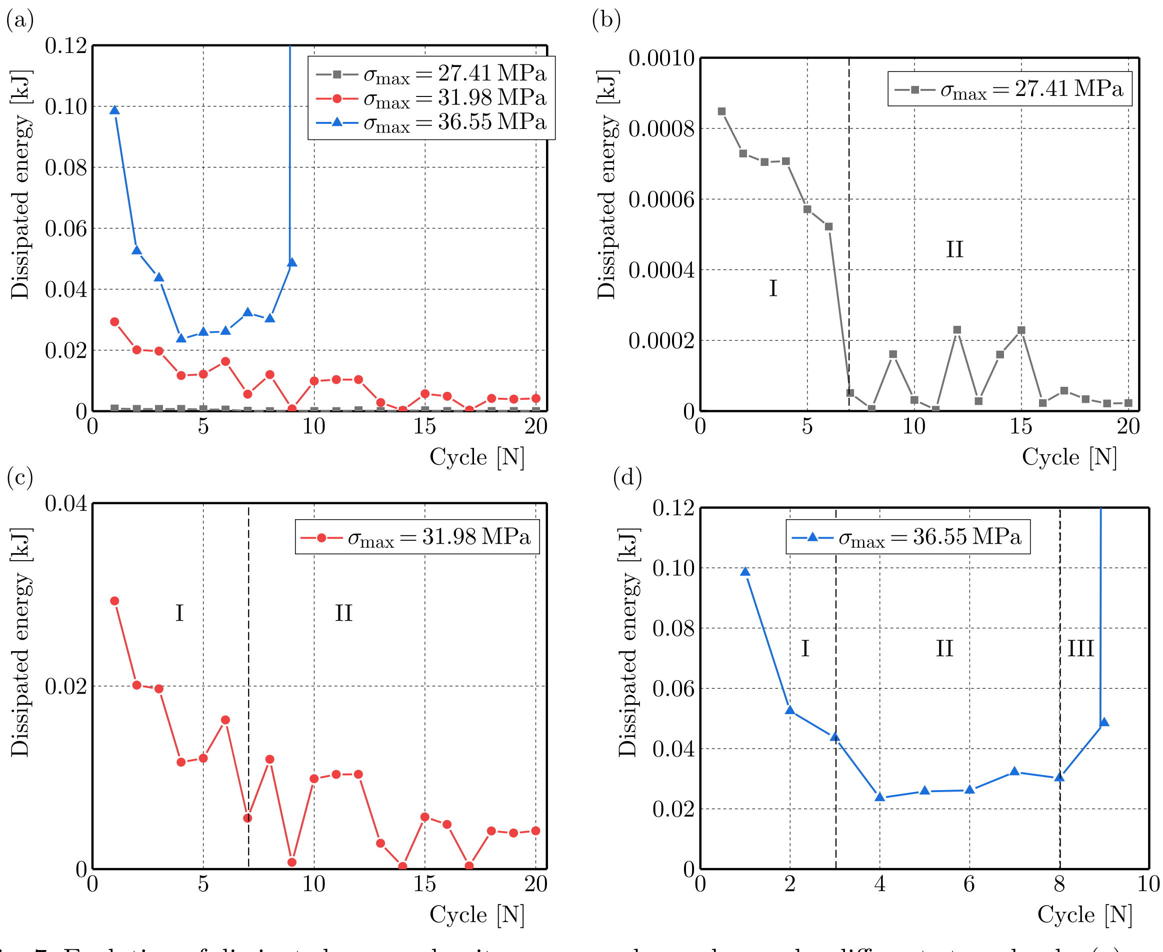

Fig. 7. Evolution of dissipated energy density versus cycle number under different stress levels: (a) comparative evolution trends; (b) 60% of saturated peak strength (27.41 MPa); (c) 70% of saturated peak strength (31.98 MPa); (d) 80% of saturated peak strength (36.55 MPa).

5. Damage evolution model

5.1. Formulation of damage variable

To quantitatively characterize the hydromechanical deterioration of the saturated red sandstone, a damage variable (D) is established based on the accumulation of residual strain. According to the strain equivalence hypothesis in continuum damage mechanics (Lemaitre, 1996), the constitutive behavior of a damaged material can be represented by that of an undamaged material subjected to an effective stress. This approach is conceptually similar to Kachanov's creep rupture theory (Kachanov, 1958), where damage accumulation is intrinsically linked to the evolution of irreversible deformation. The damage variable D is typically defined as the reduction in the effective load-bearing area, which macroscopically manifests as the degradation of the elastic modulus:

$$E = E_0(1 - D), \tag{5.1}$$

where E_0 is the initial elastic modulus of the undamaged rock ($E_0 = 22.5\,\mathrm{GPa}$, derived from the monotonic test), and E is the secant modulus of the damaged rock. Under cyclic pore-water pressure loading, the total axial strain ($\varepsilon_{\mathrm{total}}$) at the peak of each cycle consists of the initial elastic strain of the rock matrix (ε_{e0}), and the cumulative irreversible strain (ε_r) resulting from internal defect propagation:

$$\varepsilon_{\mathrm{total}} = \varepsilon_{e0} + \varepsilon_r. \tag{5.2}$$

Assuming that the damaged material obeys the following constitutive relation, the total strain can be expressed as:

$$\varepsilon_{\mathrm{total}} = \frac{\sigma}{E} = \frac{\sigma}{E_0(1 - D)}. \tag{5.3}$$

For the undamaged matrix, the initial elastic strain is given by:

$$\varepsilon_{e0} = \frac{\sigma}{E_0}. \tag{5.4}$$

Substituting Eqs. (5.3) and (5.4) into Eq. (5.2) yields the relationship between residual strain and damage:

$$\varepsilon_r = \frac{\sigma}{E_0(1 - D)} - \frac{\sigma}{E_0} = \frac{\sigma}{E_0}\left(\frac{1}{1 - D} - 1\right). \tag{5.5}$$

Solving for D, we derive a practical damage quantification formula expressed solely in terms of experimentally measurable parameters (residual strain ε_r, peak stress σ, and initial modulus E_0):

$$D = \frac{\varepsilon_r E_0}{\varepsilon_r E_0 + \sigma}. \tag{5.6}$$

This result indicates that residual strain reflects the macroscopic manifestation of microscopic void growth. When $\varepsilon_r = 0$, $D = 0$ (intact state); as $\varepsilon_r \to \infty$, $D \to 1$ (failure state).

5.2. Stress-dependent damage evolution laws

The evolution of the calculated damage variable D versus cycle number N is plotted in Fig. 8. The damage trajectories reveal a distinct dependence on the applied stress ratio, demonstrating that the extent of hydromechanical deterioration is strictly controlled by the proximity of the axial stress to the rock's yield strength.

1) Stable damage state ($\sigma \leq 60\,\%\ \sigma_{\mathrm{sat}}$): at the stress level of 27.41 MPa, the damage variable remains nearly constant at a low baseline level (≈ 0.35) throughout the 20 cycles. This stable plateau indicates that the hydraulic cycling at this intensity only induces reversible elastic deformation without triggering new defects. The microcracks undergo stable opening and closure ("breathing") without propagation. This behavior represents a "safe" hydromechanical state where the rock structure effectively accommodates the pore pressure fluctuations.

2) Self-limiting damage state ($\sigma = 70\%\ \sigma_{\text{sat}}$): at the intermediate stress level of 31.98 MPa, the damage curve exhibits a "step-like" increase in the first 5 cycles, rising from 0.409 to 0.414, before stabilizing. This distinct pattern suggests a self-limiting mechanism: the initial hydraulic pulses trigger local micro-adjustments and the compaction of existing voids, but the confining rock matrix provides sufficient constraint to arrest further crack extension. Consequently, the damage accumulation saturates quickly after the initial adaptation, preventing the development of macroscopic structural failure.
3) Runaway damage state ($\sigma = 80\,\%\ \sigma_{\text{sat}}$): at the high stress level of 36.55 MPa, the damage evolution undergoes a fundamental shift, following a three-stage "fatigue-creep" pattern similar to tertiary creep failure. It begins with a decelerating stage ($N = 1-2$) corresponding to initial adaptation, followed by a steady stage ($N = 2 - 10$) characterized by linear, slow damage accumulation (from 0.46 to 0.465). Crucially, an accelerating stage emerges after a critical threshold ($N > 10$), where the damage variable surges abruptly, surpassing 0.96. This sudden jump corresponds to the coalescence of distributed microcracks into a macroscopic failure plane, confirming that 80 % of the saturated strength serves as the critical stress threshold for hydraulic fatigue failure.

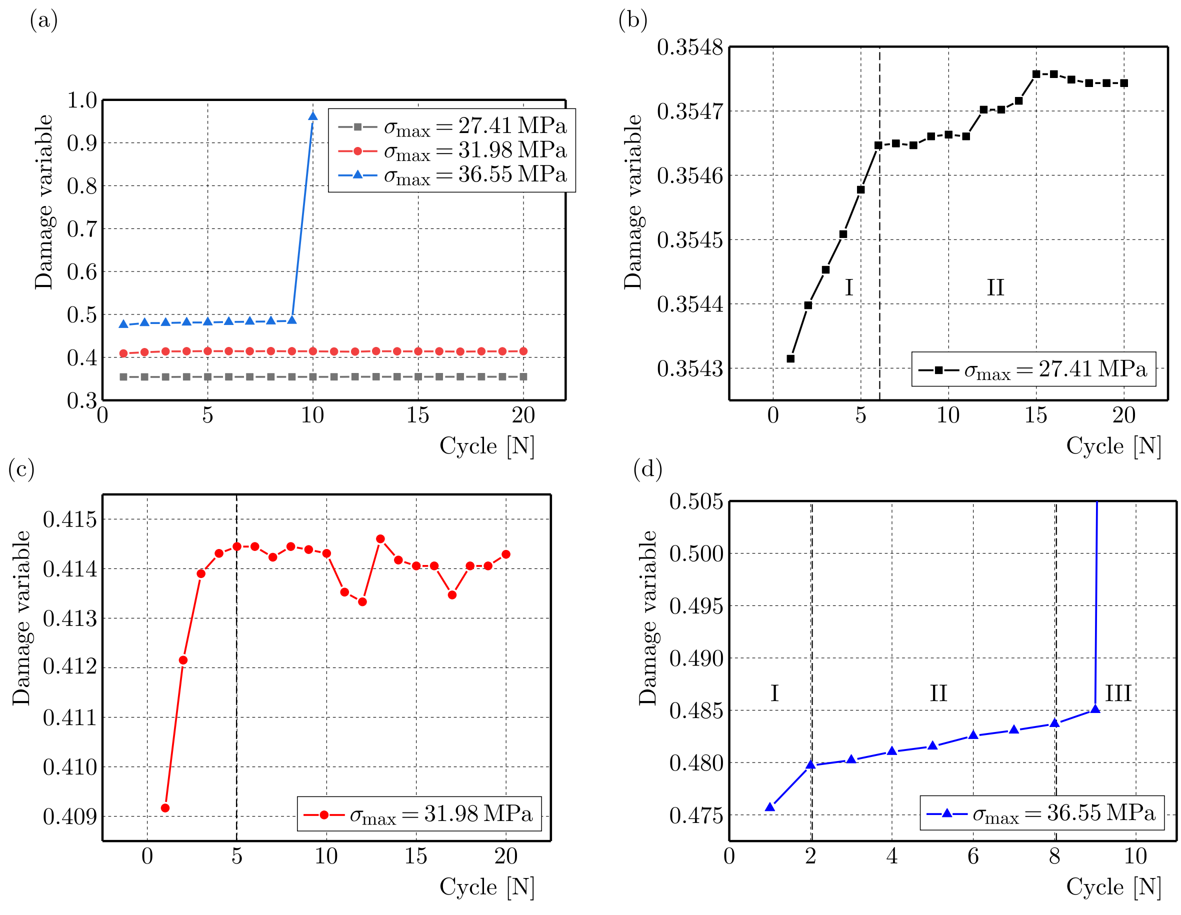

Fig. 8. Evolution of the damage variable (D) derived from residual strain under cyclic hydraulic loading: (a) comparative damage trajectories; (b) stable damage state ($\sigma = 60\%\ \sigma_{\text{sat}}$); (c) self-limiting damage state ($\sigma = 70\%\ \sigma_{\text{sat}}$); (d) runaway damage state ($\sigma = 80\%\ \sigma_{\text{sat}}$).

It is worth noting that the sudden surge in the damage variable D at the accelerating stage (Fig. 8d) aligns perfectly with the "U-shaped" upturn of dissipated energy (Fig. 7d). This consistency confirms that the derived damage model is physically grounded in the thermodynamic irreversibility of microcrack evolution.

5.3. Comparison with previous studies

The hydromechanical fatigue behavior observed in this study offers new insights distinct from traditional water-weakening protocols. To highlight the unique contribution of the current work, a comparison with existing research regarding loading paths and damage mechanisms is as follows:

1) Contrast with monotonic water-weakening: while classic static studies on water-rock interaction typically report a 15 %–30 % continuous strength degradation over long-term soaking for similar sandstones (Xuan *et al.*, 2025), our coupled dynamic tests reveal a more severe short-term degradation, recording an 18.3 % peak strength reduction upon saturation. More importantly, under monotonic loading, progressive damage only occurs with increasing shear stress. In contrast, our cyclic tests demonstrate that an extremely low dynamic fluctuation of merely 0.3 MPa can drive failure under a constant shear stress, provided the rock is held at the 80 % (σ_{sat}) threshold. This dynamic pumping effect of pore water induces fatigue damage far deeper than mere static soaking. Such a coupled mechanism significantly alters the internal pore structure and permeability evolution typically observed in similar sandstones (Wang *et al.*, 2024).
2) Distinction from high-pressure hydraulic fracturing: recent deep-earth engineering studies investigating cyclic hydraulic effects often utilize high-amplitude pressures exceeding 5 MPa to initiate new fractures (Kendrick *et al.*, 2024; Chang *et al.*, 2022). The pore pressure of 0.3 MPa applied in our study is significantly lower than the 2 MPa confinement, rendering it physically incapable of inducing hydraulic fracturing independently. Our quantitative novelty lies in establishing that this low-amplitude perturbation lowers the effective frictional resistance just enough to induce failure when the static stress is near the 70 %–80 % dilatancy boundary, which differs fundamentally from high pressure dynamic loading (Tan *et al.*, 2025) or uniaxial cyclic fatigue (Bagde & Petroš, 2005). This low amplitude fluctuation acts as a fatigue trigger rather than the primary cause of failure. It lowers the effective frictional resistance just enough to facilitate continuous slippage when the rock is already stressed near its dilatancy boundary.
3) Temporal difference from dry-wet cycling: while dry-wet cycling represents a well documented cause of reservoir bank deterioration (Yang *et al.*, 2025), it constitutes a long-term weathering process driven primarily by chemical dissolution and clay swelling over seasonal scales. The fatigue damage observed in this study operates on a much shorter meso-scale temporal domain. The rapid increase in dissipated energy and residual strain within just twenty cycles at the 80 % stress level demonstrates that intense hydraulic fluctuations during rapid reservoir regulation events can induce acute structural damage. This specific failure mode aligns with fatigue characteristics under confining pressure (Faradonbeh *et al.*, 2022) and progressive failure mechanisms reported in recent hydromechanical coupling studies (Huang *et al.*, 2025). Nevertheless, it remains fundamentally different from the slow deterioration associated with long-term weathering.

5.4. Hydromechanical fatigue mechanism

Based on the experimental data and theoretical analysis, the fatigue-like damage mechanism is summarized in Fig. 9. The cyclic pore-water pressure acts as a “hydraulic wedge” that periodically reduces the effective normal stress on crack surfaces. When coupled with the lubricating effect of water, this dynamic perturbation triggers a stress-dependent response: below the 70 % threshold, the microstructure undergoes reversible “breathing” (shakedown); whereas above the 80 % threshold, the reduced frictional resistance fails to counteract the high shear stress, leading to irreversible slip and progressive crack coalescence (ratcheting).

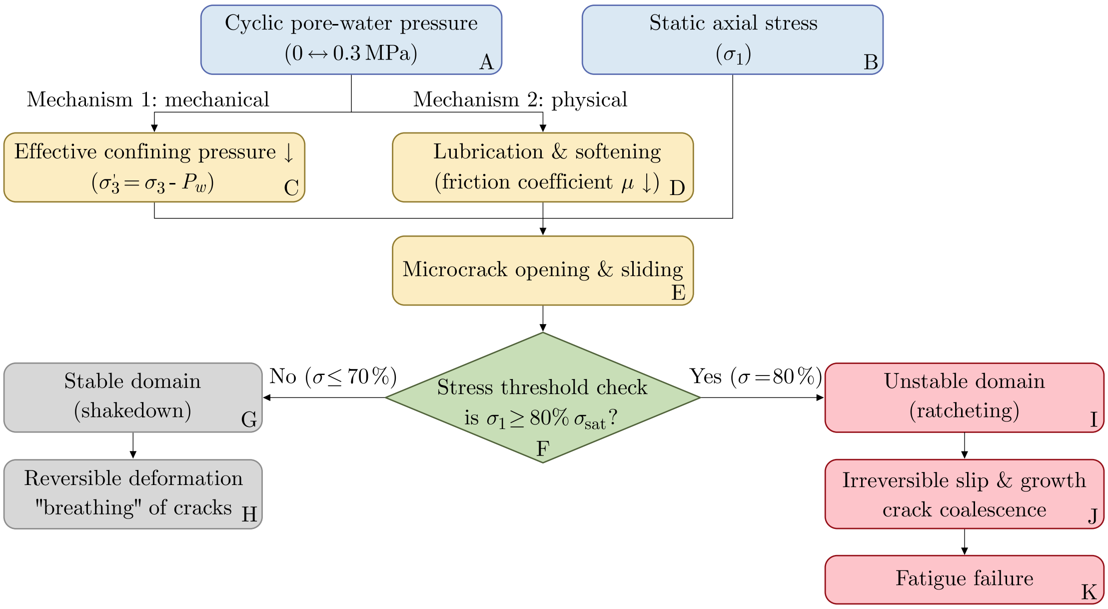

Fig. 9. Schematic diagram of the hydromechanical fatigue damage mechanism and stress-dependent threshold behaviors in saturated sandstone.

6. Conclusion

This study investigated the hydromechanical degradation and fatigue-like damage evolution of saturated red sandstone under cyclic pore-water pressure. Based on the experimental results and the derived damage model, the following conclusions are drawn:

1) The intrusion of a 0.3 MPa pore water pressure significantly weakens the mechanical competence of the red sandstone. The saturated rock exhibits an 18.3 % reduction in peak strength. This strength falls from 55.94 MPa to 45.69 MPa. The rock also shows a 19 % decline in elastic modulus compared to the dry state. This mechanical degradation stems from the dual mechanisms of effective confining pressure reduction and the physical softening of intergranular cementation. These coupled processes advance the onset of dilatancy and severely narrow the stable stress window of the rock mass.
2) The deformation response under cyclic hydraulic loading is strictly governed by the axial stress level, revealing a distinct transition from stability to failure. Specifically, within the stable domain below 32 MPa, the rock exhibits an elastic shakedown behavior. This state features stabilized damage following an initial hydromechanical adaptation. Such behavior indicates that low amplitude hydraulic cycling induces only reversible structural adjustments. Conversely, shifting to the unstable domain above 36 MPa triggers runaway damage accumulation. A critical fatigue life emerges at approximately 8–10 cycles. Beyond this specific threshold, the residual strain and dissipated energy surge nonlinearly and drive the rock toward accelerated fatigue failure.
3) A cumulative damage variable based on residual strain successfully quantifies the transition from stable crack propagation to unstable coalescence. The underlying mechanism of this hydraulic fatigue is inherently driven by the periodic fluctuation of effective stress. This dynamic fluctuation facilitates continuous frictional slippage along grain boundaries. These findings demonstrate that a critical stress threshold representing 70 % to 80 % of the saturated strength exists for reservoir bank slopes. Consequently, engineers evaluating slope stability under seasonal water level fluctuations should ensure the macroscopic factor of safety exceeds 1.4. This conservative design margin guarantees that the rock mass remains safely within the elastic shakedown domain and prevents sudden fatigue induced landslides.

Acknowledgments

This research was funded by the Graduate Innovation Program of Chongqing University of Science and Technology (grant number YKJCX2420617).

References

1. Bagde, M.N., & Petroš, V. (2005). Fatigue properties of intact sandstone samples subjected to dynamic uniaxial cyclical loading. *International Journal of Rock Mechanics and Mining Sciences*, *42*(2), 237–250. https://doi.org/10.1016/j.ijrmms.2004.08.008

2. Chang, X., Xu, E., Guo, Y., Yang, C., Hu, Z., & Guo, W. (2022). Experimental study of hydraulic fracture initiation and propagation in deep shale with different injection methods. *Journal of Petroleum Science and Engineering*, *216*, Article 110834. https://doi.org/10.1016/j.petrol.2022.110834

3. Faradonbeh, R.S., Taheri, A., & Karakus, M. (2022). Fatigue failure characteristics of sandstone under different confining pressures. *Rock Mechanics and Rock Engineering*, *55*(3), 1227–1252. https://doi.org/10.1007/s00603-021-02726-2

4. He, C.-c., Hu, X.-l., Xu, C., Wu, S.-s., Zhang, H., & Liu, C. (2020). Model test of the influence of cyclic water level fluctuations on a landslide. *Journal of Mountain Science*, *17*(1), 191–202. https://doi.org/10.1007/s11629-019-5713-9

5. He, N., Xu, J., & Zhong, W. (2026). Creep behavior and damage modeling of red sandstone under cyclic water pressure. *Advances in Civil Engineering*, *2026*(1), Article 9834337. https://doi.org/10.1155/adce/9834337

6. Hu, M., Xu, W., Wang, H., Ning, Y., Wang, R., Lyu, C., & Zhang, T. (2023). Deformation characteristics of muddy sandstones during cyclic loading and unloading with different stress lower limits under pore pressure. *International Journal of Fatigue*, *172*, Article 107606. https://doi.org/10.1016/j.ijfatigue.2023.107606

7. Huang, W., Li, Y., & Zhu, D. (2025). Mechanical characteristics and progressive failure mechanism of prefabricated defective marble under hydro-mechanical coupling. *Theoretical and Applied Fracture Mechanics*, *139*(Part B), Article 105130. https://doi.org/10.1016/j.tafmec.2025.105130

8. Kachanov, L.M. (1958). Time of the rupture process under creep conditions. *Izvestiya Akademii Nauk SSSR, Otdelenie Tekhnicheskikh Nauk*, *8*, 26–31.

9. Kendrick, J.E., Lamur, A., Mouli-Castillo, J., Lightbody, A., Fraser-Harris, A., Edlmann, K., McDermott, C.I., & Shipton, Z.K. (2024). Validating the application of cyclic hydraulic pressure pulses to reduce breakdown pressure in granite. *iScience*, *27*(10), Article 110881. https://doi.org/10.1016/j.isci.2024.110881

10. Lemaitre, J. (1996). *A course on damage mechanics* (2nd ed.). Springer.

11. Li, F., You, S., Ji, H.-g., Elmo, D., & Wang, H.-t. (2020). Strength and energy exchange of deep sandstone under high hydraulic conditions. *Journal of Central South University*, *27*(10), 3053–3062. https://doi.org/10.1007/s11771-020-4528-2

12. Li, H., Ma, L., Yang, C., Sima, Y., Liu, J., & Li, Y. (2023). Experimental investigation on the damage and deterioration of sandstone subjected to cycling pore water pressure. *Bulletin of Engineering Geology and the Environment*, *82*(4), Article 107. https://doi.org/10.1007/s10064-023-03147-x

13. Li, S., Jiao, B., Deng, B., Huang, J., & Pang, J. (2025). Impact of water–rock interaction on microstructure damage of carbonate rocks and alteration of its micromechanical properties. *Physics of Fluids*, *37*(7), Article 077104. https://doi.org/10.1063/5.0265540

14. Liang, Q., Huang, G., Zheng, J., Geng, W., Huang, J., & Sun, G. (2024). Experimental study on the response of cracked sandstone to the intermediate principal stress coupled with pore pressure. *ACS Omega*, *9*(19), 21528–21537. https://doi.org/10.1021/acsomega.4c02233

15. Liao, K., Miao, F., Wu, Y., & Zheng, H. (2025). Physical model test on a reservoir landslide with double sliding zones subjected to water level fluctuation and rainfall. *Bulletin of Engineering Geology and the Environment*, *84*(6), Article 259. https://doi.org/10.1007/s10064-025-04320-0

16. Sawicki, A., & Mierczyński, J. (2015). Some effects of intrinsic cyclic loading in saturated sands. *Journal of Theoretical and Applied Mechanics*, *53*(2), 285-293. https://doi.org/10.15632/jtam-pl.53.2.285

17. Sun, X., Ding, J., He, L., Shi, F., Zhang, Y., Miao, C., & Zhang, J. (2024). Mechanical properties and energy evolution law of water bearing sandstone under cyclic loading. *Journal of Mountain Science*, *21*(11), 3913–3929. https://doi.org/10.1007/s11629-023-8357-2

18. Tan, D., Cheng, H., Hou, C., Lei, Y., Jiang, C., Zhao, Y., & Zhang, H. (2025). Experimental study on the effects of dynamic high water pressure on the deformation characteristics of limestone. *Applied Sciences*, *15*(1), Article 42. https://doi.org/10.3390/app15010042

19. Taheri, A., Yfantidis, N., Olivares, C.L., Connelly, B.J., & Bastian, T.J. (2016). Experimental study on degradation of mechanical properties of sandstone under different cyclic loadings. *Geotechnical Testing Journal*, *39*(4), 673–687. https://doi.org/10.1520/GTJ20150231

20. Terzaghi, K. (1943). *Theoretical soil mechanics*. John Wiley & Sons.

21. Ulusay, R., & Hudson, J.A. (Eds.). (2007). *The complete ISRM suggested methods for rock characterization, testing and monitoring: 1974–2006*. ISRM Turkish National Group.

22. Wang, J., Dai, F., Yan, Z., Pang, Y., & Wei, M. (2026). Dynamic response of sandstone under hydromechanical coupling: macroscopic behavior and microscopic mechanism. *International Journal of Rock Mechanics and Mining Sciences*, *197*, Article 106342. https://doi.org/10.1016/j.ijrmms.2025.106342

23. Wang, M., Zhang, C., Liu, R., Bai, J., Chen, B., Sui, J., & Sun, X. (2024). Experimental study on permeability evolution of sandstone under cyclic loading. *Physics of Fluids*, *36*(4), Article 047141. https://doi.org/10.1063/5.0205903

24. Wang, W., Duan, X., Jia, Y., Bian, H., Chen, L., Zhu, Q., & Cao, Y. (2023). Damage evolution of sandstone based on acoustic emission under different seepage conditions. *European Journal of Environmental and Civil Engineering*, *27*(4), 1796–1812. https://doi.org/10.1080/19648189.2022.2098178

25. Xu, Q., Tian, A., Luo, X., Liao, X., & Tang, Q. (2022). Chemical damage constitutive model establishment and the energy analysis of rocks under water–rock interaction. *Energies*, *15*(24), Article 9386. https://doi.org/10.3390/en15249386

26. Xuan, Z., Cai, Y., Li, A., Yao, W., & Yu, J. (2025). Stress relaxation and long-term strength evaluation of water-bearing sandstone. *Mechanics of Time-Dependent Materials*, *29*(3), Article 60. https://doi.org/10.1007/s11043-025-09783-y

27. Yang, H., Liu, S., Tang, M., Xiao, X., & Cai, G. (2025). Field test study on rock mass deterioration characteristics of bank slope hydro-fluctuation belt of Three Gorges Reservoir. *Natural Hazards*, *121*(8), 8929–8950. https://doi.org/10.1007/s11069-025-07128-z

28. Zhao, B., Huang, T., Liu, D.Y., Liu, D.S., Liu, Y., & Wang, X. (2020). Experimental study and damage model study of rock salt subjected to cyclic loading and cyclic creep. *Advances in Civil Engineering*, *2020*(1), Article 8049626. https://doi.org/10.1155/2020/8049626

Manuscript received March 5, 2026; accepted for publication June 26, 2026; published online August 22, 2026.

JOURNAL OF THEORETICAL
AND APPLIED MECHANICS
64, 3, pp. 231–244, Warsaw 2026
https://doi.org/10.15632/jtam-pl/226002

DYNAMIC MODELING OF WIND TURBINE BLADES UNDER UNCERTAINTIES: NONLINEAR ANALYSIS AND STOCHASTIC QUANTIFICATION BY ADVANCED FINITE ELEMENTS

Rania MAKTOUF[1*], Nourhaine YOUSFI[1], Ahmed GHORBEL[2], Nabih FEKI[3], Ali AKROUT[1], Mohamed HADDAR[1]

[1] *Mechanical Modeling and Manufacturing Laboratory (LA2MP), National School of Engineers of Sfax, University of Sfax, Sfax, Tunisia*
[2] *Higher Institute of Applied Sciences and Technology of Kairouan, University of Kairouan, Tunisia*
[3] *Higher Institute of Applied Sciences and Technology of Sousse, University of Sousse, Tunisia*
[*]corresponding author, *raniaphymaktouf@gmail.com*

This article presents a modal and nonlinear dynamic analysis of a twisted blade, highlighting the influence of rotational speed on bending and torsional responses. An advanced finite element formulation is developed, based on separating translational and rotational kinetic energies. The blade is modeled using six-degree-of-freedom beam elements with non-uniform cross-sections, enabling the accurate capture of geometric nonlinearities. Furthermore, the study incorporates the effect of uncertainties in material properties on the dynamic response, combining Monte Carlo simulations and a polynomial chaos approach. The results show that these uncertainties significantly influence displacements, particularly at high rotational speeds, underscoring the importance of robust and probabilistic modeling.

Keywords: wind turbine blade; modal analysis; uncertainty; geometric nonlinearity.

1. Introduction

Rotating beams are key structural elements in many engineering applications, particularly in aerospace and energy systems such as aircraft wings, helicopter rotors, and wind turbine blades (Hodges & Rutkowski, 1981; Jureczko *et al.*, 2005; Leissa *et al.*, 1982). Their dynamic behavior is strongly influenced by rotational speed, which significantly affects natural frequencies and mode shapes (Kim *et al.*, 2013; Park *et al.*, 2010). As a result, accurate vibration analysis is essential for reliable structural design.

Various modeling approaches have been proposed to investigate these systems. The finite element method (FEM) remains the most widely used, enabling detailed evaluation of blade dynamics under centrifugal, gravitational, and gyroscopic effects (Chung & Yoo, 2002; Hamdi *et al.*, 2014). Analytical formulations based on energy methods, particularly Hamilton's principle, have also been developed to describe different vibration modes of rotating beams (Kim *et al.*, 2013). In addition, parametric studies have highlighted the influence of key factors such as rotational speed, tip mass, and geometric characteristics on the overall dynamic response (Lee *et al.*, 2004; Sheibani & Akbari, 2015).

Most early investigations rely on linear assumptions with small deflections (Zhang & Huang, 2011). However, such simplifications are no longer valid for modern large-scale wind turbine blades, which exhibit significant geometric nonlinearities due to their flexibility. To overcome this limitation, several nonlinear formulations have been introduced, although they often involve increased computational cost (Palacios & Cesnik, 2009). Advanced approaches have been proposed to capture large deformation effects with good accuracy, including refined beam theories and nonlinear finite element models (Filippi *et al.*, 2018; Moeenfard & Awtar, 2014; Pagani & Carrera, 2018; Yangui *et al.*, 2018). These studies demonstrate the importance of centrifugal stiffening, damping, and gyroscopic coupling in the dynamic response of rotating structures (Hamdi, 2025; Maktouf *et al.*, 2019).

Despite these advances, uncertainties are often neglected in blade modeling. In practice, turbine blades are subject to variability in material properties, manufacturing processes, and operating conditions. Probabilistic methods provide an appropriate framework to address this issue. The Monte Carlo approach is widely used due to its simplicity, but it requires a high computational cost (Ni *et al.*, 2019). Alternatively, spectral methods such as polynomial chaos expansion (PCE) offer an efficient way to represent uncertainty through orthogonal polynomial bases (Askey & Wilson, 1985). These methods have been successfully applied to structural dynamics, sensitivity analysis, and inverse problems, providing accurate results with reduced computational effort (Ni *et al.*, 2019; Schwarz *et al.*, 2024; Serra & Florentin, 2023). More recently, PCE has been integrated into blade design to account for geometric imperfections and manufacturing variability, improving prediction robustness (Gao *et al.*, 2019; Zhao *et al.*, 2025).

In this context, the present study develops a finite element model of a wind turbine blade to analyze its dynamic behavior under rotation while incorporating uncertainties in material parameters. This combined deterministic-stochastic approach aims to enhance the accuracy and reliability of performance predictions.

2. Numerical modeling and uncertainty

2.1. Blade modeling

The structural design of the turbine blade is illustrated in Fig. 1. The blade structure was modeled using beam elements, each providing six-degrees-of-freedom per node.

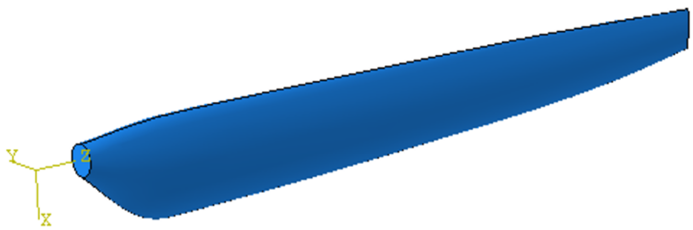

Fig. 1. Wind turbine blade design.

The rotation axis R coincides with the z-axis of the absolute fixed system and Ω_t presents the angular position of the local system with respect to the stationary one.

2.2. Kinetic energy

Let $\{d\}$ denote the motion vector with all blade's degrees of freedom:

$$\{d\} = \{u, v, w, \alpha, \beta, \gamma\}^T. \tag{2.1}$$

The translational displacements along the x-, y-, and z-axes are denoted by u, v, and w, while α, β, and γ represent the corresponding rotations.

The angular velocity vector is defined as

$$\{\Omega\} = \{0 \quad 0 \quad \Omega\}^T. \tag{2.2}$$

The position vector of a point N in the local coordinate system R is

$$\mathbf{r} = \{x, y, z\}^T. \tag{2.3}$$

Using the transformation matrix $[t_m]$, the position in the fixed frame R_1 becomes:

$$\bar{\mathbf{r}}_{R_1} = [t_m]\mathbf{r} = \begin{bmatrix} \cos \Omega t & -\sin \Omega t & 0 \\ \sin \Omega t & \cos \Omega t & 0 \\ 0 & 0 & 1 \end{bmatrix} \begin{Bmatrix} x \\ y \\ z \end{Bmatrix}. \tag{2.4}$$

2.2.1. Translational displacement kinetic energy

The translational motion of a representative point in the local system R, denoted by $\{u_{\text{tran}}\}$ and illustrated in Fig. 2a, is given by

$$\{u_{\text{tran}}\} = \{u \quad v \quad w\}^t. \tag{2.5}$$

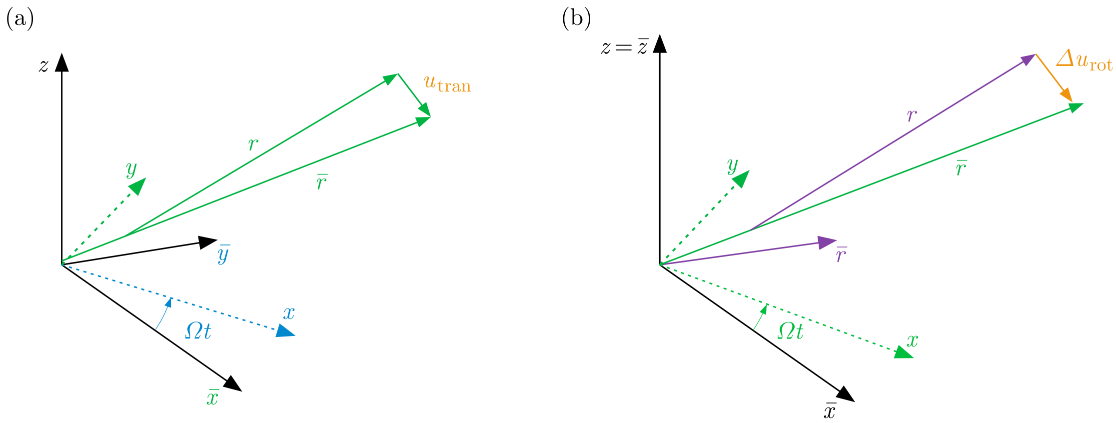

Fig. 2. Blade displacement modes: (a) motion of translational mode; (b) motion of rotational mode.

The kinetic energy in the absolute system R_1 is given by

$$T = \frac{m}{2}\{\dot{\bar{r}}\}^t\{\dot{\bar{r}}\}, \tag{2.6}$$

where the position vector of the locally displaced and globally rotating particle, expressed in the fixed reference frame, is given as follows:

$$\{\bar{r}\} = [t_m](\{r\} + \{u_{\text{tran}}\}). \tag{2.7}$$

The velocity of the vector in Eq. (2.7), expressed in the fixed frame, can be written as follows:

$$\{\dot{\bar{r}}\} = \Omega[\bar{t}_m](\{r\} + \{u_{\text{tran}}\}) + [t_m]\{\dot{u}_{\text{tran}}\}. \tag{2.8}$$

By employing the quantities defined in Eq. (2.8), the kinetic energy takes the following form:

$$T = \frac{m}{2}(\Omega(\{r\}^t + \{u_{\text{tran}}\}^t)[\bar{t}_m]^t + \{\dot{u}_{\text{tran}}\}^t[t_m]^t)(\Omega[\bar{t}_m](\{r\} + \{u_{\text{tran}}\}) + [t_m]\{\dot{u}_{\text{tran}}\}). \tag{2.9}$$

By collecting and arranging the terms, the expression of the kinetic energy of the translational motion was obtained:

$$\begin{aligned} T = {} & \frac{m}{2}(\Omega^2\{r\}^t[J][\{r\}] + 2\Omega^2\{r\}^t[\{J\}]\{u_{\text{tran}}\}) \\ & + \frac{m}{2}(\Omega^2\{u_{\text{tran}}\}^t[\{J\}]\{u_{\text{tran}}\}) + 2\Omega\{\dot{u}_{\text{tran}}\}^t[P]^t[r] \\ & + 2\Omega\{u_{\text{tran}}\}^t[P]\{\dot{u}_{\text{tran}}\} + \{\dot{u}_{\text{tran}}\}^t[I]\{\dot{u}_{\text{tran}}\}), \end{aligned} \tag{2.10}$$

where P denotes the product of the motion and velocity transformation matrix, while J denotes the product of the matrix of velocity transformation and its transpose.

2.2.2. Rotational motion kinetic energy

The vector u_{rot} is defined as the rotational components of the particle along the three nodal axes:

$$\{u_{\text{rot}}\} = \{\alpha \quad \beta \quad \gamma\}^t. \tag{2.11}$$

As a result, the vector Au_{rot} represents the particle's rotational motion induced by the nodal rotation, as illustrated in Fig. 2b.

The moments of inertia can be determined in several ways: by defining a concentrated mass, by distributing the inertia across the finite element mesh among neighboring mass points, or as in our case, by attaching six submasses to the node. This approach corresponds to a lumped-mass approximation, in which the continuous inertia distribution within each element is concentrated at the nodes, neglecting the distributed mass between them. This simplification preserves the translational and rotational nodal inertia associated with the six-degrees-of-freedom and provides a practical compromise between computational efficiency and accuracy for the lower vibration modes considered in this study (Maktouf *et al.*, 2019). In this context, we denote the total mass at the node as $m = 6m'$. The corresponding inertia terms are then expressed as follows:

$$\theta_x = 2m'(y'^2 + z'^2), \qquad \theta_y = 2m'(x'^2 + z'^2), \qquad \theta_z = 2m'(x'^2 + y'^2). \tag{2.12}$$

Here, x', y', z' denote the coordinates of the mass point. Considering a rotation about the z-axis by an angle γ, this induces a transformation of the point's position in the local system, which is described as follows:

$$\{\widetilde{r}\} = \begin{pmatrix} \cos\gamma & -\sin\gamma & 0 \\ \sin\gamma & \cos\gamma & 0 \\ 0 & 0 & 1 \end{pmatrix} \{r\}. \tag{2.13}$$

A rotation about the x-axis by an angle α results in the following transformation:

$$\{\widetilde{r}\} = \begin{pmatrix} 1 & 0 & 0 \\ 0 & \cos\alpha & -\sin\alpha \\ 0 & \sin\alpha & \cos\alpha \end{pmatrix} \{r\}. \tag{2.14}$$

Finally, a rotation about the y-axis by an angle β yields the following transformation:

$$\{\widetilde{r}\} = \begin{pmatrix} \cos\beta & 0 & \sin\beta \\ 0 & 1 & 0 \\ -\sin\beta & 0 & \cos\beta \end{pmatrix} \{r\}. \tag{2.15}$$

The combined transformation is obtained by multiplying the three preceding matrices and can be expressed as follows:

$$\{\widetilde{r}\} = ([I] + [\widetilde{A}])\{r\}, \tag{2.16}$$

where

$$[\widetilde{A}] = \begin{pmatrix} 0 & -\gamma & \beta \\ \gamma & 0 & -\alpha \\ -\beta & \alpha & 0 \end{pmatrix}. \tag{2.17}$$

The nodal rotations can be converted into nodal translations using the following relation:

$$\{Au_{\text{rot}}\} = [A]\{u_{\text{rot}}\} = [A]\{\alpha, \beta, \gamma\}^T, \tag{2.18}$$

where

$$[A] = \begin{pmatrix} 0 & z' & -y' \\ -z' & 0 & x' \\ y' & -x' & 0 \end{pmatrix}. \tag{2.19}$$

By applying Eqs. (2.6) and (2.7) for the rotational displacement, the position vector in the fixed system can be expressed as follows:

$$\overline{\{r\}} = [t_m]\{r\} + [t_m][A]\{u_{\mathrm{rot}}\}. \tag{2.20}$$

By differentiating the preceding equation, the velocity can be expressed as

$$\overline{\{\dot{r}\}} = \Omega[t_m]\{r\} + \Omega\overline{[t_m]}[A]\{u_{\mathrm{rot}}\} + [t_m][A]\{\dot{u}_{\mathrm{rot}}\}. \tag{2.21}$$

Following the same procedure applied to translational displacement, the kinetic energy associated with rotational motion is given by:

$$\begin{aligned} T = {} & \frac{m}{2}(\Omega^2\{r\}^t[J]\{r\} + 2\Omega^2\{r\}^t[J][A]\{u_{\mathrm{rot}}\} + 2\Omega\{r\}^t[P][A]\{u_{\mathrm{rot}}\}) \\ & + \frac{m}{2}(\Omega^2\{u_{\mathrm{rot}}\}^t[A]^t[J][A]\{u_{\mathrm{rot}}\} + 2\Omega\{u_{\mathrm{rot}}\}^t[A]^t[P][A]\{u_{\mathrm{rot}}\}) \\ & + \frac{m}{2}(\{u_{\mathrm{rot}}\}^t[A]^t[I][A]\{u_{\mathrm{rot}}\}). \end{aligned} \tag{2.22}$$

2.3. Equations governing motion

The stiffness matrix is obtained by integrating the deformation matrix $[B]$ with the matrix of elastic stiffness $[\widetilde{E}]$ (Batoz & Dhatt, 1990):

$$[K_e] = \int\limits_V [B]^t[\widetilde{E}][B], \tag{2.23}$$

$$[\widetilde{E}] = \frac{E}{(1+\nu)(1-2\nu)} \begin{pmatrix} \mathbf{D} & \mathbf{0} \\ \mathbf{0} & \dfrac{1-2\nu}{2}\mathbf{I}_3 \end{pmatrix}, \qquad \mathbf{D} = \begin{pmatrix} 1-\nu & \nu & \nu \\ \nu & 1-\nu & \nu \\ \nu & \nu & 1-\nu \end{pmatrix}, \tag{2.24}$$

where $[\widetilde{E}]$ denotes the elasticity matrix, E is the elastic modulus, $[B]$ is the deformation matrix, and ν is Poisson's ratio. Applying Lagrange's equation of motion to the kinetic energy of translational motion yields:

$$\frac{d}{dt}\left(\frac{\partial T}{\partial\{\dot{u}_{\mathrm{tran}}\}}\right) - \frac{\partial T}{\partial\{u_{\mathrm{tran}}\}} = 0. \tag{2.25}$$

Considering that $[P]^t = -[P]$, we obtain:

$$m[I]\{\ddot{u}_{\mathrm{tran}}\} + 2\Omega m[P]\{\dot{u}_{\mathrm{tran}}\} - \Omega^2 m[I]\{u_{\mathrm{tran}}\} = \Omega^2 m[J]\{r\}, \tag{2.26}$$

where $\Omega^2 m[J]\{r\}$ represents the centrifugal force. As shown in Eq. (2.28), this force depends on the particle's radial position and the rotational speed:

$$m\Omega^2[J]\{r\} = \{f_{\mathrm{ctran}}\}. \tag{2.27}$$

We introduce new matrices associated with the translational motion: $[M_{\text{tran}}]$, $[C_{\text{tran}}]$, and $[Z_{\text{tran}}]$, which represent the element mass, gyroscopic, and centrifugal stiffness matrices, respectively,

$$[M_{\text{tran}}] = m[I] = \begin{bmatrix} m & 0 & 0 \\ 0 & m & 0 \\ 0 & 0 & m \end{bmatrix}, \tag{2.28}$$

$$[C_{\text{tran}}] = m[P] = \begin{bmatrix} 0 & -m & 0 \\ m & 0 & 0 \\ 0 & 0 & 0 \end{bmatrix}, \tag{2.29}$$

$$[Z_{\text{tran}}] = m[J] = \begin{bmatrix} m & 0 & 0 \\ 0 & m & 0 \\ 0 & 0 & 0 \end{bmatrix}. \tag{2.30}$$

Considering only the kinetic energy associated with translational displacement, the matrix equation of motion takes the form:

$$[M_{\text{tran}}]\{\ddot{u}_{\text{tran}}\} + 2\Omega[C_{\text{tran}}]\{\dot{u}_{\text{tran}}\} - \Omega^2[Z_{\text{tran}}]\{u_{\text{tran}}\} = \{f_{\text{tran}}\}. \tag{2.31}$$

Applying Lagrange's equation of motion to the vector of rotation u_{rot} yields:

$$\frac{d}{dt}\left(\frac{\partial T}{\partial\{\dot{u}_{\text{rot}}\}}\right) - \frac{\partial T}{\partial\{u_{\text{rot}}\}} = [M_{\text{rot}}]\{\ddot{u}_{\text{rot}}\} + 2\Omega[C_{\text{rot}}]\{\dot{u}_{\text{rot}}\} - \Omega^2[Z_{\text{rot}}]\{u_{\text{rot}}\} = \{f_{crot}\}, \tag{2.32}$$

where $[M_{\text{rot}}]$ is the mass matrix, $[Z_{\text{rot}}]$ is the centrifugal stiffness matrix, $[C_{\text{rot}}]$ is the gyroscopic matrix, and $\{f_{\text{crot}}\}$ is the centrifugal force vector:

$$[M_{\text{rot}}] = \begin{bmatrix} \theta_x & 0 & 0 \\ 0 & \theta_y & 0 \\ 0 & 0 & \theta_z \end{bmatrix}, \tag{2.33}$$

$$[C_{\text{rot}}] = \begin{bmatrix} 0 & -\frac{1}{2}(\theta_x + \theta_y - \theta_z) & 0 \\ \frac{1}{2}(\theta_x + \theta_y - \theta_z) & 0 & 0 \\ 0 & 0 & 0 \end{bmatrix}, \tag{2.34}$$

$$[Z_{\text{rot}}] = \begin{bmatrix} (\theta_y - \theta_z) & 0 & 0 \\ 0 & (\theta_x - \theta_z) & 0 \\ 0 & 0 & 0 \end{bmatrix}, \tag{2.35}$$

$$\{f_{\text{crot}}\} = m\Omega^2\{-z'y' \quad z'x' \quad 0\}^t. \tag{2.36}$$

The blade displacement induces additional strain energy under rotation, resulting in a geometric stiffness matrix as

$$[K_g] = \int\limits_V [G]^t[\sigma][G]dV, \tag{2.37}$$

where $[G]$ is the matrix relating the nodal motions to their derivatives, and $[g]$ is the stress matrix expressed as

$$[g] = \begin{bmatrix} [S] & 0 & 0 \\ 0 & [S] & 0 \\ 0 & 0 & [S] \end{bmatrix}, \tag{2.38}$$

where

$$[S] = \begin{bmatrix} \sigma_x & \tau_{xy} & \tau_{xz} \\ \tau_{xy} & \sigma_y & \tau_{yz} \\ \tau_{xz} & \tau_{yz} & \sigma_z \end{bmatrix}. \tag{2.39}$$

Finally, the nonlinear equation of motion can be expressed as

$$[M]\{\ddot{q}\} + [C]\{\dot{q}\} + ([K_E] + [K_R] + [K_G])\{q\} = \{F\}. \tag{2.40}$$

Here, the global matrices $[M]$, $[C]$, $[K_E]$, $[K_R]$, $[K_G]$, and the force vector $\{F\}$ are assembled from the element matrices.

All were obtained by assembling the element matrices defined as follows:

$$[M_e] = \begin{bmatrix} [M_{\text{tran}}] & 0 \\ 0 & [M_{\text{rot}}] \end{bmatrix}, \tag{2.41}$$

$$[K_r] = -\Omega^2 \begin{bmatrix} [Z_{\text{tran}}] & 0 \\ 0 & [Z_{\text{rot}}] \end{bmatrix}, \tag{2.42}$$

$$[C_e] = 2\Omega \begin{bmatrix} [C_{\text{tran}}] & 0 \\ 0 & [C_{\text{rot}}] \end{bmatrix}, \tag{2.43}$$

$$\{F_e\} = \begin{Bmatrix} f_{\text{ctran}} \\ f_{\text{crot}} \end{Bmatrix}. \tag{2.44}$$

2.4. Uncertainty quantification methods

Uncertainty propagation is performed using both Monte Carlo simulation and generalized polynomial chaos (GPC). Monte Carlo is used as a reference solution, while GPC is adopted for its high computational efficiency.

2.4.1. Monte Carlo method

The Monte Carlo method estimates output statistics through random sampling of uncertain inputs. For a model $y = f(\mathbf{r})$, the expectation is approximated by

$$\mathbb{E}[y] \approx \frac{1}{N}\sum_{i=1}^{N} f(\mathbf{r}_i), \tag{2.45}$$

where $\mathbf{r}_i$ is the independent sample and N denotes the number of realizations. Although accurate, this method requires a large number of simulations, resulting in high computational cost.

2.4.2. Generalized polynomial chaos method

The GPC method represents the model response as a spectral expansion:

$$y(\boldsymbol{\xi}) \approx \sum_{k=0}^{P} c_k \Phi_k(\boldsymbol{\xi}), \tag{2.46}$$

where P is the order of the expansion and Φ_k are orthogonal polynomials satisfying:

$$\mathbb{E}[\Phi_i \Phi_j] = \delta_{ij}\langle \Phi_j^2 \rangle. \tag{2.47}$$

The polynomial basis is selected according to the Askey scheme (Askey & Wilson, 1985), such as Hermite (Gaussian), Legendre (uniform), Laguerre (gamma), and Jacobi (beta). The GPC implementation adopted in this study is non-intrusive, treating the deterministic finite element solver as a black box. The stochastic modes are determined by a regression-based least-squares solution at Gauss–Legendre collocation points. The uncertain parameters E and G_t are modeled as uniform random variables bounded within $\pm 5\,\%$ and $\pm 20\,\%$ of their nominal values, and the Legendre polynomial basis is adopted consistent with the Askey scheme (Askey & Wilson, 1985). A second-order expansion ($p = 2$) is retained, whose accuracy is confirmed by the excellent agreement with the Monte Carlo reference solution across all investigated configurations (Fig. 6 to Fig. 8). Figure 3 illustrates the overall methodology used in this study.

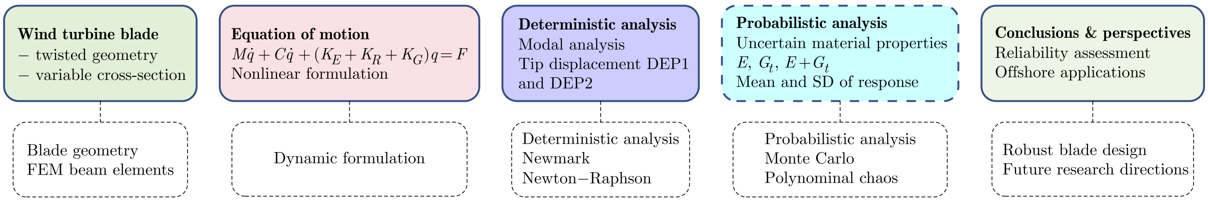

Fig. 3. Flowchart used to study the wind turbine blade under uncertainty.

3. Numerical results

The numerical simulation carried out in MATLAB begins with the determination of the displacement responses. The Monte Carlo and the polynomial chaos methods are then applied to extract the average values of these responses, based on the standard deviations (SDs) of the defined uncertain parameters. The blade material parameters are summarized in Table 1.

Table 1. Material parameters of the turbine blade.

Density ρ [Kg/m^3]	2700
Young modulus E [N/m^2]	6.9×10^{10}
Shear modulus G_t [N/m^2]	2.7×10^{10}
Poisson's ratio ν	0.33

3.1. Dynamic behavior of the deterministic model

The modal analysis is performed for the non-rotating case ($\Omega = 0$), for which all rotation-dependent matrices reduce to zero and the equation of motion reduces to the standard eigenvalue problem $\big([\mathbf{K}_E] - \omega^2[\mathbf{M}]\big)\,\{\varphi\} = \{0\}$. The proposed finite element model was validated by comparing the first five natural frequencies and their associated modal shapes with the results obtained using ABAQUS V6.16. Quantitative validation is presented in Table 2, while Fig. 4 illustrates the corresponding eigenmodes. Good agreement is observed between the two models, with small relative differences, confirming the ability of the developed model to accurately reproduce the dynamic behavior of the blade.

Table 2. Comparison of natural frequencies predicted by the present model and ABAQUS.

Mode	Present model [Hz]	ABAQUS [Hz]	Error [%]
1	6.50	6.30	3.17
2	13.70	12.60	8.1
3	23.00	22.40	2.68
4	53.80	52.15	3.16
5	64.30	65.50	1.8

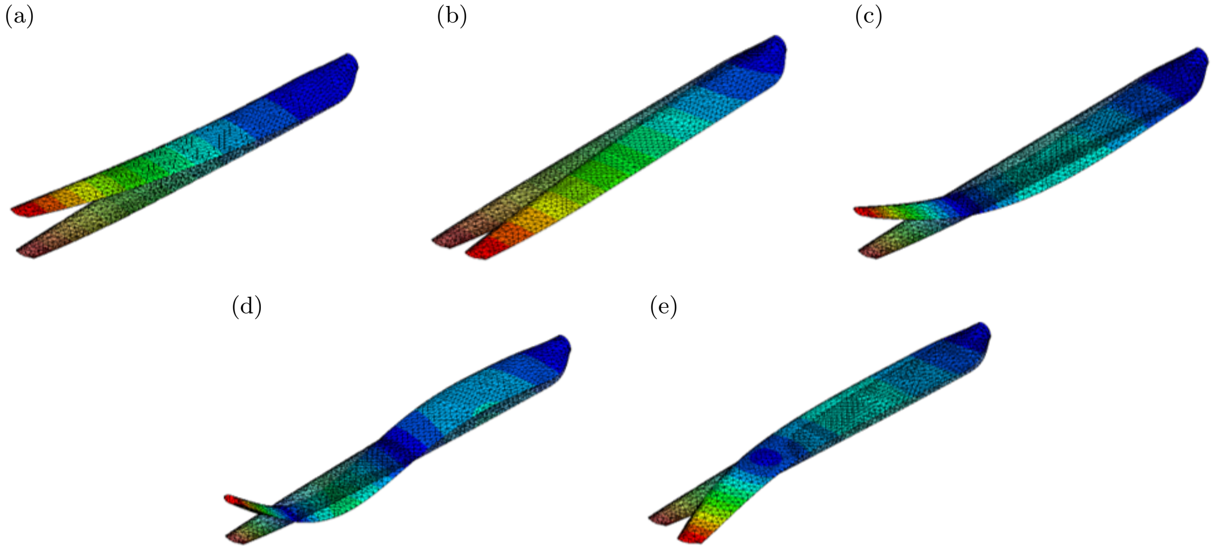

Fig. 4. Initial set of natural frequencies for the blade obtained using Abaqus software: (a) flapwise deflection (6.301 Hz); (b) edgewise deflection (12.601 Hz); (c) flapwise deflection (22.403 Hz); (d) flapwise deflection (52.146 Hz); (e) edgewise deflection (65.547 Hz).

Furthermore, the deterministic displacement responses at the blade tip are presented in Fig. 5 for the flapwise and edgewise directions. These results highlight the expected nonlinear effects on the dynamic response and form the basis of the uncertainty analysis developed in the remainder of the study. Here, the blade tip displacement (DEP1, DEP2) refers to the stabilized tip deflection value reached at equilibrium for a given rotational frequency, obtained from the deterministic model, and constitutes the quantity propagated through the uncertainty quantification framework.

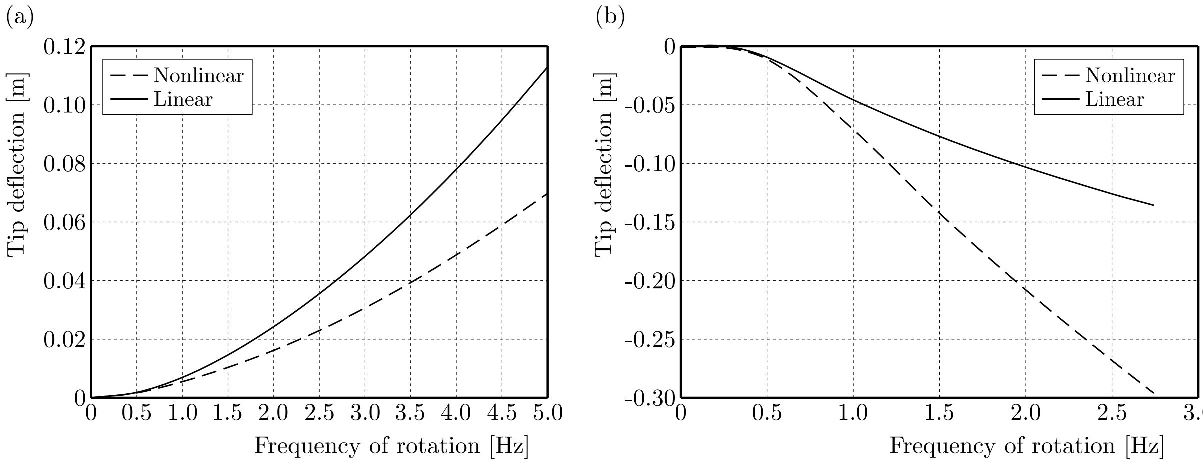

Fig. 5. Tip blade displacement in flapwise (a) and edgwise (b) directions.

3.2. Probabilistic simulations of wind turbine blade

For the upcoming simulations, uncertainty quantification methods will be applied to assess the system's dynamic behavior under variations in the material parameters. During the design process, several material variables may influence the system. In this study, Young's modulus E and the shear modulus G_t are uncertain with SDs equal to 5 % and 20 %, so as to evaluate their impact on the dynamic response of the blade. The simulations follow the framework of the uncertainty study shown in Section 3. In the first stage, uncertainty was introduced through a single uncertainty parameter (uncoupled form) and after that a coupled form was studied in order to show the effect of uncertainty in the blade displacements.

3.2.1. Effect of Young's modulus E

The first simulation focuses on the uncertainty of Young's modulus E with an SD σ_E equal to 5 % and 20 %.

Figure 6 shows the mean value and SD of the displacements in the flapwise (DEP1) and edgewise (DEP2) directions, obtained using the Monte Carlo and GPC approaches for two levels of uncertainty of Young's modulus E: $\sigma_E = 5\,\%$ and 20 %. Figure 6a and Fig. 6b show that the mean values of the flapwise (DEP1) and edgewise (DEP2) displacements increase progressively with the rotational frequency. Increasing σ_E from 5 % to 20 % induces only a slight variation in the mean, indicating that uncertainties in E have a weak influence on the central tendency of the blade's dynamic behavior. The results obtained by the GPC method are in excellent agreement with those from the Monte Carlo simulation, thus confirming the validity and accuracy of the second-order polynomial expansion ($p = 2$) for estimating the mean response of the system.

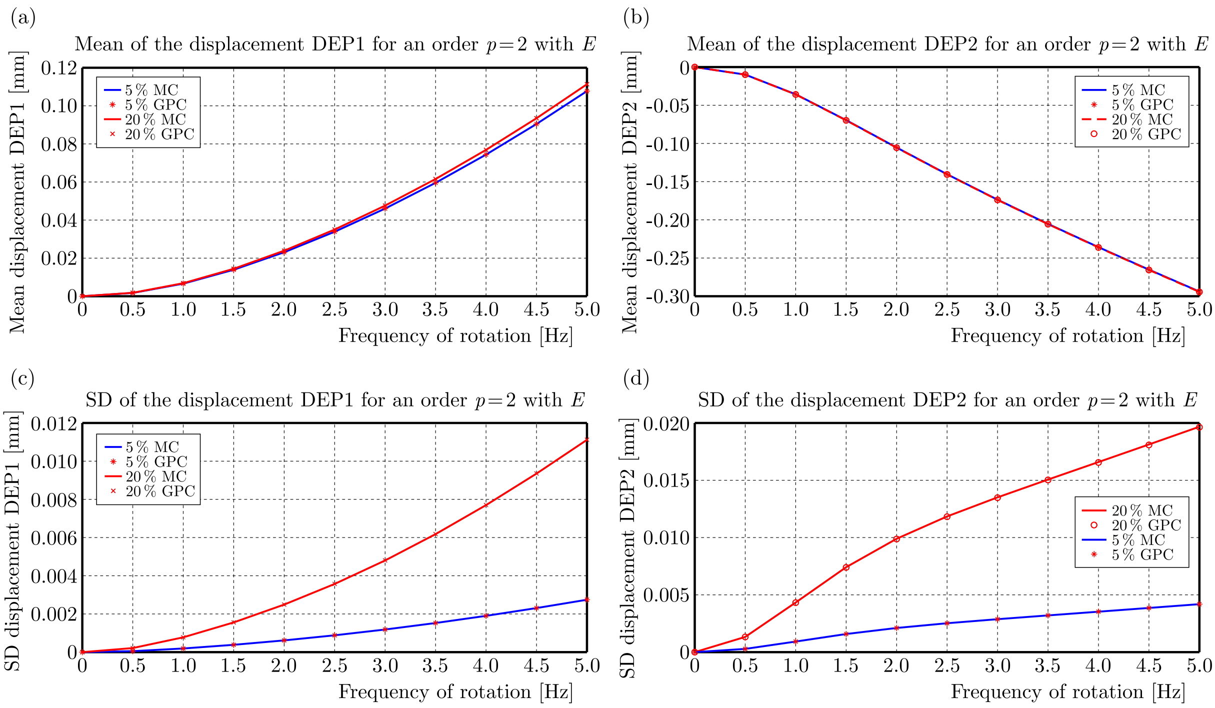

Fig. 6. Mean value and SD of the displacement for DEP1 and DEP2 with $\sigma_E = 5\,\%$ and 20 %.

In the case of the flapwise displacement (DEP1), the response remains positive and increases with the frequency, reflecting increased deflection in the blade's principal plane. Conversely, the edgewise displacement (DEP2) is negative and decreases with frequency, which reflects a bending opposite to the direction of rotation, dominated by inertial and aerodynamic forces.

The results highlight the sensitivity of the responses to uncertainties in Young's modulus. The increase in input variance ($\sigma_E = 20\,\%$) strongly amplifies the SD of the displacements for both deflection directions. This amplification is particularly pronounced at high frequencies, emphasizing that the effects of material uncertainties become more significant in fast dynamic regimes. The GPC curves faithfully reproduce the Monte Carlo results, while considerably reducing the computational cost, confirming the reliability of the polynomial probabilistic framework for quantifying uncertainties in vibration responses DEP1 and DEP2 in the presence of E.

3.2.2. Effect of the shear modulus G_t

The next simulation focuses on the uncertainty in the shear modulus G_t, with the SD σ_{G_t} set to 5 % and 20 %. Figure 7 presents the evolution of the mean value and SD of the flapwise (DEP1)

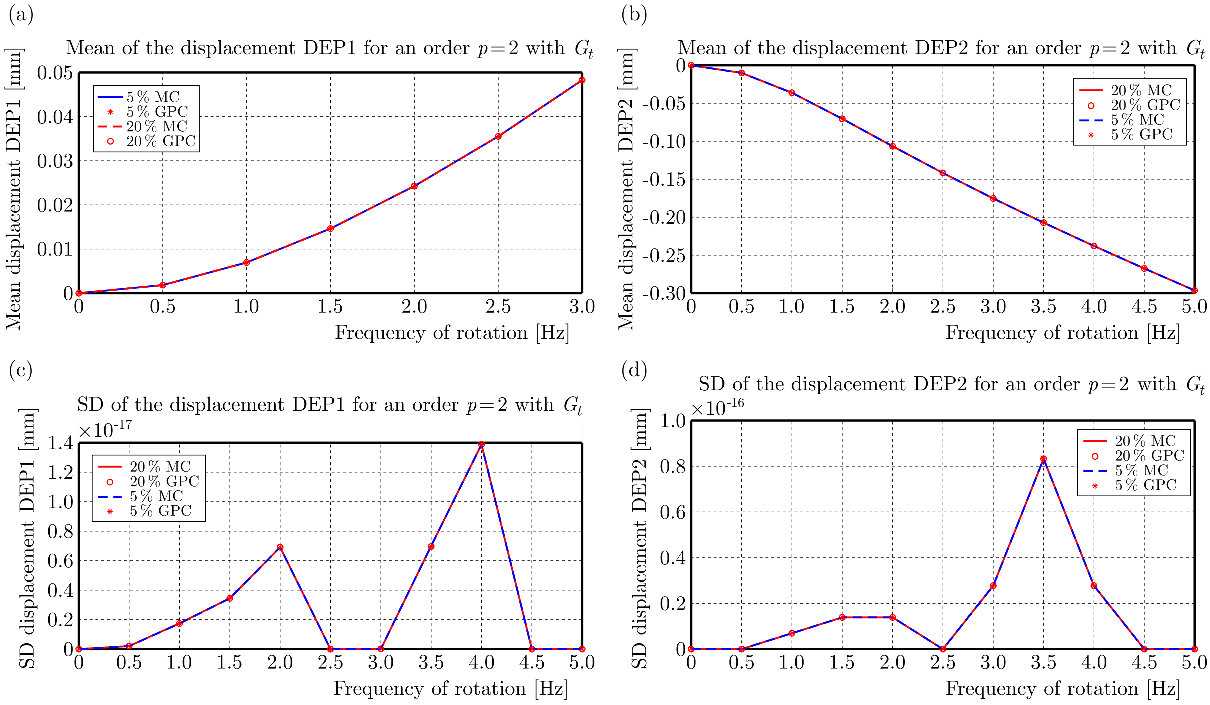

Fig. 7. Mean value and SD of blade tip displacements (DEP1 and DEP2) for $\sigma_{G_t} = 5\,\%$ and $20\,\%$.

and edgewise (DEP2) displacements for the two uncertainty levels. The obtained results indicate that the average displacements DEP1 and DEP2 remain virtually identical for both uncertainty levels of G_t. Also, the GPC results perfectly reproduce those of the Monte Carlo simulation. This superposition of the curves indicates that, unlike E, the variability of the shear modulus G_t has little influence on the average value of the deflections in both directions.

From a physical perspective, this is explained by the fact that G_t primarily governs the torsional stresses and shear deformations of the blade profile. Under the conditions considered here, the flapwise and edgewise bending behavior is dominated by the contributions of Young's modulus E. Therefore, the perturbation of G_t only marginally affects the overall stiffness. Thus, the average response of the blade remains essentially unchanged, whether the dispersion of G_t is moderate ($5\,\%$) or high ($20\,\%$). The observed behavior reflects the weak coupling between torsion and bending under the considered loading conditions. Specifically:

– the flapwise displacement (DEP1) depends primarily on the longitudinal bending stiffness dominated by E;
– the edgewise displacement (DEP2), although influenced by shear effects, remains strongly constrained by axial stiffness and inertial forces, limiting the direct effect of G_t.

3.2.3. Effect of coupled uncertainty

In this part, we study the effect of coupled uncertainty $E + G_t$ in the response of the wind turbine blade. Figure 8 shows the mean value and SD of the flapwise (DEP1) and edgewise (DEP2) displacements for $\sigma_{E+G_t} = 5\,\%$ and $20\,\%$.

The results illustrated in Fig. 8 indicate that increasing the uncertainty level from $5\,\%$ to $20\,\%$ in both E and G_t has a limited effect on the mean displacements in both flapwise (DEP1) and edgewise (DEP2) directions. This behavior highlights the relatively high structural stiffness of the blade, for which moderate variations in material properties do not significantly alter the average response.

Regarding variability, the SD increases proportionally with the uncertainty level, indicating an almost linear propagation of input uncertainties. At low rotational frequencies, the response

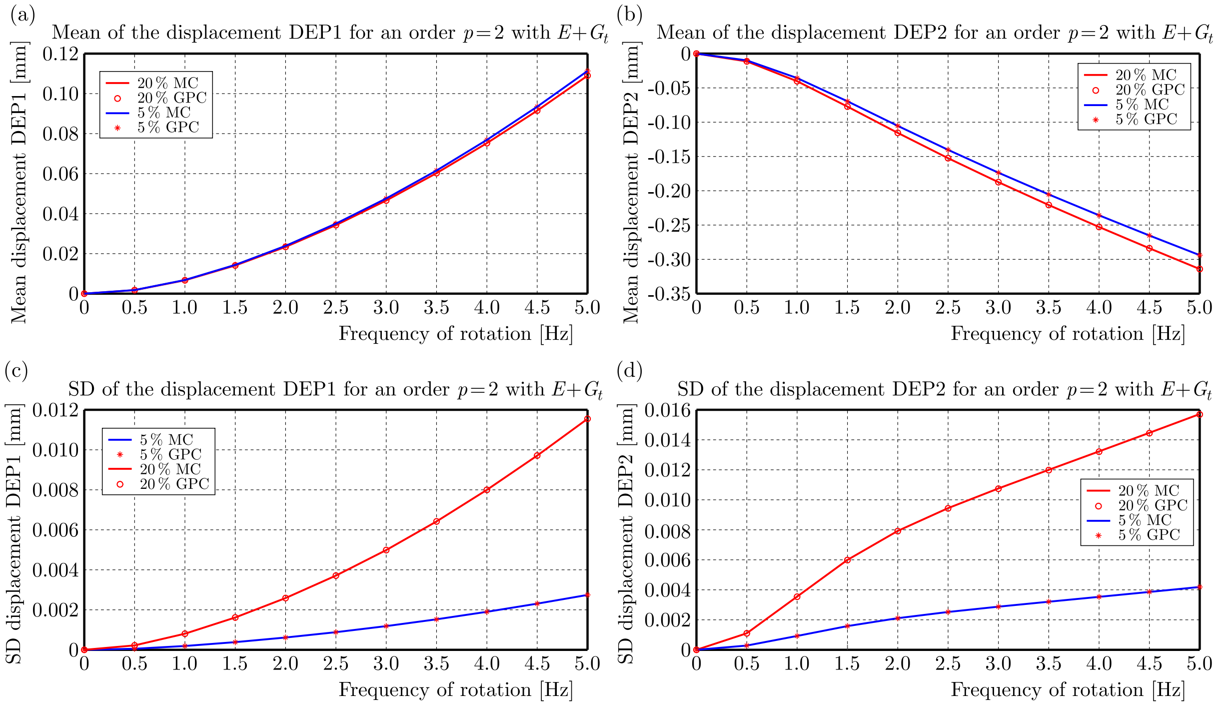

Fig. 8. Mean value and SD of blade tip displacements (DEP1 and DEP2) for combined uncertainties $\sigma_{E+G_t} = 5\,\%$ and $20\,\%$.

remains nearly deterministic, whereas at higher frequencies, the variability is amplified due to inertial effects. This amplification suggests that material uncertainties may play a more significant role under dynamic operating conditions, potentially influencing long-term fatigue behavior.

Overall, the results demonstrate that while the mean response is weakly affected by material variability, the dispersion of the dynamic response becomes more pronounced at higher excitation levels, underlining the importance of uncertainty quantification for reliable blade design.

4. Conclusion

This article introduces a novel finite element model for rotating wind turbine blades, grounded in beam theory and incorporating critical geometric nonlinearities often neglected in conventional approaches. The blade motion equation was resolved by coupling the Newmark time-integration procedure with a Newton–Raphson iterative algorithm to compute the displacement criterion used for stability assessment, which allows the extraction of displacement responses. Moreover, flapwise and edgewise deflections on the tip of the blade have been obtained. A thorough comparison between Monte Carlo simulation and GPC highlights their respective strengths for quantifying material uncertainties: the robustness of Monte Carlo in the face of complex distributions, offset by its slow convergence, versus the computational efficiency of GPC for moderate-dimensional problems. For the adopted numerical settings (Monte Carlo with 1000 samples), the polynomial chaos approach required approximately 90 times less computational time than the Monte Carlo simulation, while providing comparable estimates of the statistical moments. This comparison reflects computational efficiency rather than a formal convergence-rate analysis. In short, this study demonstrates the originality of a holistic integration between nonlinear dynamics and probabilistic uncertainty quantification, essential for boosting the durability and performance of wind turbines. It provides new perspectives for offshore applications, where the incorporation of nonlinearities associated with dynamic loads or extreme conditions could further improve these predictions, motivating future research on AI-based real-time optimization.

References

1. Askey, R., & Wilson, J. (1985). Some basic hypergeometric orthogonal polynomials that generalize Jacobi polynomials. *Memoirs of the American Mathematical Society*, *54*(319). https://doi.org/10.1090/memo/0319

2. Batoz, J.-L., & Dhat, G. (1990). *Finite element modeling of structures. Vol. 1: Elastic solids* (in French). Presses de l'Université Laval.

3. Chung, J., & Yoo, H.H. (2002). Dynamic analysis of a rotating cantilever beam by using the finite element method. *Journal of Sound and Vibration*, *249*(1), 147–164. https://doi.org/10.1006/jsvi.2001.3856.

4. Filippi, M., Pagani, A., & Carrera, E. (2018). Accurate nonlinear dynamics and mode aberration of rotating blades. *Journal of Applied Mechanics*, *85*(11), Article 111004. https://doi.org/10.1115/1.4040693.

5. Gao, L., Ma, C., & Cai, Y. (2019). A robust blade design method based on non-intrusive polynomial chaos considering profile error. *Journal of Thermal Science*, *28*(5), 875–885. https://doi.org/10.1007/s11630-019-1185-6.

6. Hamdi, H. (2025). Three-dimensional linear vibration of a rotating cantilever beam with an adjusted proportional damping model. *Journal of Vibration Engineering and Technologies*, *13*(8), Article 599. https://doi.org/10.1007/s42417-025-02174-0.

7. Hamdi, H., Mrad, C., Hamdi, A., & Nasri, R. (2014). Dynamic response of a horizontal axis wind turbine blade under aerodynamic, gravity and gyroscopic effects. *Applied Acoustics*, *86*, 154–164. https://doi.org/10.1016/j.apacoust.2014.04.017.

8. Hodges, D.H., & Rutkowski, M.J. (1981). Free-vibration analysis of rotating beams by a variable-order finite-element method. *AIAA Journal*, *19*(11), 1459–1466. https://doi.org/10.2514/3.60082.

9. Jureczko, M., Pawlak, M., & Mężyk, A. (2005). Optimisation of wind turbine blades. *Journal of Materials Processing Technology*, *167*(2–3), 463–471. https://doi.org/10.1016/j.jmatprotec.2005.06.055.

10. Kim, H., Yoo, H.H., & Chung, J. (2013). Dynamic model for free vibration and response analysis of rotating beams. *Journal of Sound and Vibration*, *332*(22), 5917–5928. https://doi.org/10.1016/j.jsv.2013.06.004.

11. Lee, S.H., Shin, S.H., & Yoo, H.H. (2004). Flapwise bending vibration analysis of rotating composite cantilever beams. *KSME International Journal*, *18*(2), 240–245. https://doi.org/10.1007/BF03184733.

12. Leissa, A.W., Lee, J.K., & Wang, A.J. (1982). Rotating blade vibration analysis using shells. *Journal of Engineering for Gas Turbines and Power*, *104*(2), 296–302. https://doi.org/10.1115/1.3227279.

13. Maktouf, R., Yangui, M., Fakhfekh, T., Nasri, R., & Haddar, M. (2019). Non-linear dynamic analysis of a wind turbine blade. *Journal of the Chinese Institute of Engineers*, *42*(8), 727–737. https://doi.org/10.1080/02533839.2019.1660229.

14. Moeenfard, H., & Awtar, S. (2014). Modeling geometric nonlinearities in the free vibration of a planar beam flexure with a tip mass. *Journal of Mechanical Design*, *136*(4), Article 044502. https://doi.org/10.1115/1.4026147.

15. Ni, P., Xia, Y., Li, J., & Hao, H. (2019). Using polynomial chaos expansion for uncertainty and sensitivity analysis of bridge structures. *Mechanical Systems and Signal Processing*, *119*, 293–311. https://doi.org/10.1016/j.ymssp.2018.09.029

16. Pagani, A., & Carrera, E. (2018). Unified formulation of geometrically nonlinear refined beam theories. *Mechanics of Advanced Materials and Structures*, *25*(1), 15–31. https://doi.org/10.1080/15376494.2016.1232458.

17. Palacios, R., & Cesnik, S. (2009). Structural models for flight dynamic analysis of very flexible aircraft. In *50th AIAA/ASME/ASCE/AHS/ASC Structures, Structural Dynamics, and Materials Conference (AIAA 2009–2403). American Institute of Aeronautics and Astronautics*. https://doi.org/10.2514/6.2009-2403.

18. Park, J.-H., Park, H.-Y., Jeong, S.-Y., Lee, S.-I., Shin, Y.-H., & Park, J.-P. (2010). Linear vibration analysis of rotating wind-turbine blade. *Current Applied Physics*, *10*(2), S332–S334. https://doi.org/10.1016/j.cap.2009.11.036.

19. Schwarz, S., Carta, D., Monti, A., & Benigni, A. (2024). A direct and analytical method for inverse problems under uncertainty in energy system design: combining inverse simulation and Polynomial Chaos theory. *Energy Informatics*, *7*, Article 55. https://doi.org/10.1186/s42162-024-00360-0.

20. Serra, Q., & Florentin, E. (2023). Verification of polynomial chaos surrogates in the framework of structural vibrations with uncertainties. *Mechanics and Industry*, *24*, Article 42. https://doi.org/10.1051/meca/2023037.

21. Sheibani, M., & Akbari, A.A. (2015). Finite element modeling of a wind turbine blade. *Journal of Vibroengineering*, *17*(7), 3774–3791. https://doi.org/10.21595/jve.2015.16033

22. Yangui, M., Bouaziz, S., Taktak, M., Haddar, M., & El-Sabbagh, A. (2018). Nonlinear analysis of twisted wind turbine blade. *Journal of Mechanics*, *34*(3), 269–278. https://doi.org/10.1017/jmech.2016.120.

23. Zhang, P., & Huang, S. (2011). Review of aeroelasticity for wind turbine: Current status, research focus and future perspectives. *Frontiers in Energy*, *5*(4), 419–434. https://doi.org/10.1007/s11708-011-0166-6.

24. Zhao, Z., Wang, L., Li, X., & Wang, T. (2025). An efficient and high-precision nonlinear co-rotational beam method for wind turbine blades considering tapering effects and anisotropy. *Energies*, *18*(18), Article 4907. https://doi.org/10.3390/en18184907.

Manuscript received April 25, 2026; accepted for publication July 15, 2026;
published online July 22, 2026.

JOURNAL OF THEORETICAL
AND APPLIED MECHANICS
64, 3, pp. 245–256, Warsaw 2026
https://doi.org/10.15632/jtam-pl/226037

ANALYSIS OF VIBRATION CHARACTERISTICS OF POROUS FUNCTIONALLY GRADED CONICAL SHELL IN THERMAL ENVIRONMENTS

Runhao WAN[1*], Wenguang LIU[2]

[1] *School of Advanced Manufacturing, Nanchang University, Nanchang, China*
[2] *School of Aeronautical Manufacturing and Mechanical Engineering, Nanchang Hangkong University, Nanchang, China*
*corresponding author, *wanrunhao@email.ncu.edu.cn*

This study investigates the free vibration modal frequencies of a metal-ceramic functionally graded porous conical shell under thermal loading. Temperature-dependent material properties and two porosity distribution patterns, namely uniform and non-uniform porosity distributions, are considered. Based on the Sanders shell theory and the Rayleigh–Ritz method with Chebyshev polynomials, the model is verified by FEM within 5.04 % error. Parametric analysis shows that temperature dominates at low wave numbers, while porosity governs at high wave numbers. Increasing the S-shaped volume fraction exponent raises frequencies and weakens thermal effects, providing a theoretical basis for high-temperature engineering applications.

Keywords: porosity; thermal loading; Chebyshev polynomials; functionally graded conical shell; modal frequencies.

1. Introduction

Functionally graded materials (FGMs) are advanced composites with continuous spatial variations in composition, microstructure and properties. Owing to their high heat resistance, high strength, and lightweight characteristics, FGMs can effectively alleviate thermal-stress concentrations (Asemi & Jedari Salami, 2015; Kołakowski & Teter, 2016; Kalali *et al.*, 2016; Pillai & Rahaman, 2026; Ding & Li, 2008; Chumanov *et al.*, 2015). Therefore, FGMs have broad application prospects in aerospace and mechanical engineering.

Conical shells are widely used in aircraft fuselages, vessel propulsion systems, and other load-bearing structures that often operate in complex multi-field coupled environments. Consequently, the design and analysis of FGM conical shells have attracted considerable research attention. As advanced composite structures, FGMs may contain internal defects such as pores owing to limitations in manufacturing technologies. The presence of pores not only affects the material's acoustic properties and thermal conductivity but also influences its mechanical behavior. In recent years, a mounting number of scholars have commenced exploring the influence of material porosity on the mechanical behavior of FGM shells. Grounded in the geometrically nonlinear Kirchhoff–Love thin shell constitutive model, Feng and Hu (2026) examined the dynamic behavior of porous ferromagnetic FGM cylindrical shells under armature action. Within the framework of the first-order shear deformation theory, Xue *et al.* (2023) explored the free vibration behavior of porous FGM cylindrical panels and shells. Adopting the sinusoidal shear deformation theory and the Rayleigh–Ritz method, Wang and Wu (2017) examined the free vibration characteristics of FGM shells under different porosity distribution patterns. Applying an innovative semi-analytical method, Li *et al.* (2019) explored the free vibration behavior of porous FGM shells under arbitrary boundary conditions.

FGMs have also received extensive attention in high-temperature engineering applications since their initial proposal by Japanese researchers in the 1980s. Reddy (2000) analyzed the bending and vibration of FGM plates under thermal loads using a higher-order shear deformation theory, considering the temperature-dependent nonlinear variation of material properties. Matsunaga (2009) assessed the thermal buckling of FGM shells via a higher-order theory, emphasizing the coupling effect between boundary conditions and the gradient index. Concerning dynamic feedback, Huang and Shen (2004) examined the impacts of thermal surroundings on the nonlinear vibration characteristics of FGM shells. They discovered that temperature rise generally leads to a decrease in natural frequency, though the gradient distribution can modulate this trend. Mallek *et al.* (2025) considered two distinct porosity distribution patterns and conducted a comprehensive analysis on the porosity effects of porous FGMs.

Limited studies have addressed the free vibration of porous FGM conical shells under thermal loading. Therefore, this study develops a semi-analytical model based on the Sanders shell theory and the Rayleigh–Ritz method. Temperature-dependent material properties and different porosity distributions are incorporated through the Voigt model to examine the effects of thermal gradients, porosity, and material gradation on modal frequencies.

2. Geometry model

As depicted in Fig. 1, it is assumed that the boundary conditions at the endpoints of the FGM conical shell are simulated by artificial springs. The geometric parameters of the conical shell include: length L, thickness h, the radius of the small end is R_1 and the radius of the large end is R_2, the semi-cone angle is a_0. The material properties of the FGM conical shell vary continuously and gradually only through the thickness, an inherent material characteristic unchanged during vibration analysis. The outer surface of the conical shell is pure metal, and the inner surface is pure ceramic. An orthogonal surface coordinate system (x, θ, z) is established at the mid-surface of the conical shell, as shown in Fig. 1. The x, θ, z represent the axial, circumferential and thickness direction, respectively. The displacement components in the x, θ, and z directions of the coordinate system are represented by u, v, and w, respectively.

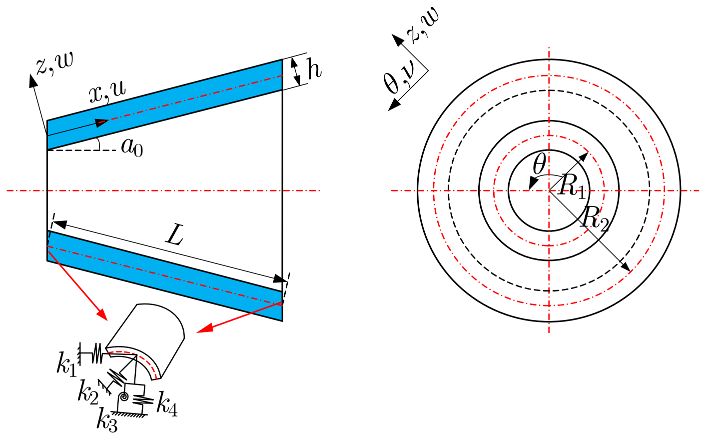

Fig. 1. Geometric model and coordinate system of a porous FGM conical shell: x – axial direction, θ – circumferential direction, z – thickness direction, R_1 – small-end radius, R_2 – large-end radius, L – length, a_0 – semi-cone angle.

The radius at any point on the shell's mid-surface varies along the axial coordinate x (Wan *et al.*, 2025b):

$$R(x) = R_1 + x \sin(\alpha_0), \qquad 0 \le x \le L. \tag{2.1}$$

3. Thermophysical properties of FGMs

Two typical porosity distributions along the thickness are considered: even porosity (model I) and uneven porosity (model II), as illustrated in Fig. 2. Within the framework of the Voigt model, the effective material property of FGMs with different pore distribution patterns is given as follows (Wang *et al.*, 2018):

$$
\begin{aligned}
&P_{\text{eff}}^{\text{I}}(x,z) = (P_m - P_c)V_m + \frac{\gamma}{2}(P_c + P_m),\\
&P_{\text{eff}}^{\text{II}}(x,z) = (P_m - P_c)V_m + P_c - \frac{\lambda}{2}\left(1 - 2\frac{|z|}{h}\right)(P_c + P_m),
\end{aligned}
\tag{3.1}
$$

where $P_{\text{eff}}^{\text{I}}$ and $P_{\text{eff}}^{\text{II}}$ denote the effective material property P of the FGMs for porosity models I and II, respectively. In this study, P represents the effective elastic modulus E_{eff}, Poisson's ratio ν_{eff}, density ρ_{eff}, thermal expansion coefficient α_{eff}, or thermal conductivity coefficient k_{eff}. The parameter γ denotes the porosity volume fraction, V_m denotes the metal volume fraction, and the subscripts c and m refer to ceramic and metal, respectively.

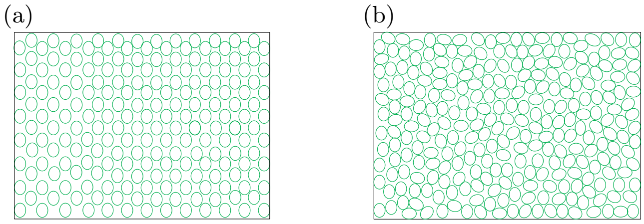

Fig. 2. Pore distribution: (a) even porosity, (b) uneven porosity.

To realize a gradual and continuous evolution of internal stresses within FGMs, Chi and Chung (2006) proposed a Sigmoid-type piecewise volume fraction:

$$
\begin{aligned}
&V_{1m}(z) = 1 - \frac{1}{2}\left(\frac{h/2 - z}{h/2}\right)^N, \qquad 0 \leq z \leq h/2,\\
&V_{2m}(z) = \frac{1}{2}\left(\frac{h/2 + z}{h/2}\right)^N, \qquad 0 \leq z \leq h/2,
\end{aligned}
\tag{3.2}
$$

where N is the volume-fraction exponent controlling the material gradation through the thickness. The functions $V_{1m}(z)$ and $V_{2m}(z)$ denote the metal volume fractions in the upper half-thickness interval ($0 \leq z \leq h/2$) and lower half-thickness interval ($-h/2 \leq z \leq 0$), respectively.

Considering the temperature dependence of the physical properties of FGMs, the material parameters can be expressed as (Shen, 2012):

$$
P_{c,m} = p_0\left(p_{-1}T^{-1} + 1 + p_1T + p_2T^2 + p_3T^3\right),
\tag{3.3}
$$

where $P_{c,m}$ represents the thermal property parameters of the material; p_0, p_{-1}, p_1, p_2, p_3 are the temperature-sensitive characteristic coefficients of the material, with specific values as shown in Table 1.

Under thermal conditions, a nonlinear temperature distribution is assumed through the thickness of an FGM conical shell. The inner surface ($z = -h/2$) is at temperature T_c, and the outer surface ($z = h/2$) is at $T_m = 300\,\text{K}$ (ambient). In the stress-free state, the thickness-dependent temperature rise $T(z)$ is derived from the steady-state heat conduction equation and thermal boundary conditions:

$$
\begin{aligned}
&T(z) = T_c - T_{cm}\xi(z,h),\\
&-\frac{\mathrm{d}}{\mathrm{d}z}\left[k_{\text{eff}}(z)\frac{\mathrm{d}T}{\mathrm{d}z}\right] = 0,
\end{aligned}
\tag{3.4}
$$

Table 1. Temperature-dependent coefficients of ZrO_2-SUS304 (Liu *et al.*, 2017).

Properties	Material	p_{-1}	p_0	p_1	p_2	p_3
ρ [$\mathrm{kg\cdot m^{-3}}$]	SUS304	0	8166	0	0	0
	ZrO_2	0	3657	0	0	0
E [GPa]	SUS304	0	201.04	3.079×10^{-4}	-6.534×10^{-4}	0
	ZrO_2	0	132.20	-3.805×10^{-4}	-6.127×10^{-4}	0
v	SUS304	0	0.3262	-2.002×10^{-4}	3.797×10^{-4}	0
	ZrO_2	0	0.3330	0	0	0
a [$\mathrm{K^{-1}}$]	SUS304	0	12.3×10^{-6}	8.086×10^{-6}	0	0
	ZrO_2	0	13.3×10^{-6}	-1.421×10^{-3}	9.549×10^{-7}	0
k [$\mathrm{W/m\cdot K}$]	SUS304	0	12.04	0	0	0
	ZrO_2	0	1.78	0	0	0

where $T_{cm} = T_c - T_m$ represents the temperature difference across the inner and outer surfaces of the shell. The solution form of the function $\xi(z,h)$ was obtained by Wu (2004) as a polynomial series:

$$\xi(z,h) = \frac{\dfrac{2z+h}{2h} + \displaystyle\sum_{i=1}^{5} \frac{-1}{iN+1}\left(\frac{k_{cm}}{k_m}\right)^i \left(\frac{2z+h}{2h}\right)^{iN+1}}{1 + \displaystyle\sum_{i=1}^{5}\left[\frac{(-1)^i}{iN+1}\left(\frac{k_{cm}}{k_m}\right)^i\right]}, \tag{3.5}$$

where $k_{cm} = k_c - k_m$, and k_c and k_m denote the thermal conductivity coefficients of the ceramic and metal, respectively.

4. Energy equation of an FGM conical shell

The Sanders shell theory is employed to derive the strain-displacement relations for an FGM conical shell, with the following basic assumptions: (1) the straight normal to the shell mid-surface remains straight after deformation but is not necessarily normal to it; (2) the transverse normal stress is negligible; (3) in-plane strains and normal rotations are small; (4) the shell thickness is much smaller than its characteristic dimensions.

Based on the Sanders shell theory, the relations between the in-plane strains and displacement components of a conical shell can be derived as follows (Loy & Lam, 1997):

$$\begin{aligned}
&\varepsilon_x = \varepsilon_1 - z\varepsilon_4, \qquad \varepsilon_\theta = \varepsilon_2 - z\varepsilon_5, \qquad \varepsilon_{x\theta} = \varepsilon_3 - 2z\varepsilon_6,\\
&\{\varepsilon_1,\varepsilon_2,\varepsilon_3\} = \left\{\frac{\partial u}{\partial x},\ \frac{1}{R}\left(\frac{\partial v}{\partial \theta} + w\right),\ \frac{\partial v}{\partial x} + \frac{1}{R}\frac{\partial u}{\partial \theta}\right\},\\
&\{\varepsilon_4,\varepsilon_5\} = \left\{\frac{\partial^2 w}{\partial x^2},\ \frac{1}{R^2}\left(\frac{\partial^2 w}{\partial \theta^2} - \frac{\partial v}{\partial \theta}\right)\right\},\\
&\{2\varepsilon_6\} = \left\{\frac{1}{R}\left(\frac{2\partial^2 w}{\partial x\partial\theta} + \frac{1}{2R}\frac{\partial u}{\partial \theta} - \frac{3}{2}\frac{\partial v}{\partial x}\right)\right\},
\end{aligned} \tag{4.1}$$

where ε_x and ε_θ represent the normal strains in the x and θ directions, respectively; $\varepsilon_{x\theta}$ denotes the shear strain within the $x\theta$ plane; ε_1, ε_2, and ε_3 are the surface strain components of the mid-surface; ε_4, ε_5, and ε_6 represent the curvatures of the mid-surface.

The stress-strain constitutive relation is formulated as

$$\begin{Bmatrix} \sigma_x \\ \sigma_\theta \\ \sigma_{x\theta} \end{Bmatrix} = \begin{pmatrix} Q_{11} & Q_{12} & 0 \\ Q_{12} & Q_{22} & 0 \\ 0 & 0 & Q_{33} \end{pmatrix} \begin{Bmatrix} \varepsilon_x \\ \varepsilon_\theta \\ \varepsilon_{x\theta} \end{Bmatrix}, \tag{4.2}$$

where σ_x and σ_θ denote the normal stresses in the x and θ directions, respectively; $\sigma_{x\theta}$ is the shear stress in the $x\theta$ plane; Q_{jk} $(j,k = 1,2,3)$ represents the reduced stiffness constants, defined as

$$\begin{aligned} &Q_{11}(s) = Q_{22}(s) = \frac{E^1_{\mathrm{eff}}(s)}{1 - v^1_{\mathrm{eff}}(s)}, \qquad Q_{12}(s) = \frac{v^1_{\mathrm{eff}}(s) E^1_{\mathrm{eff}}(s)}{1 - v^1_{\mathrm{eff}}(s)}, \\ &\qquad\qquad\qquad\qquad\qquad\qquad Q_{33}(s) = \frac{E^1_{\mathrm{eff}}(s)}{2(1 + v^1_{\mathrm{eff}}(s))}, \qquad 0 \le z \le h/2, \\ &Q_{11}(s) = Q_{22}(s) = \frac{E^2_{\mathrm{eff}}(s)}{1 - v^2_{\mathrm{eff}}(s)}, \qquad Q_{12}(s) = \frac{v^2_{\mathrm{eff}}(s) E^2_{\mathrm{eff}}(s)}{1 - \left(v^2_{\mathrm{eff}}(s)\right)^2}, \\ &\qquad\qquad\qquad\qquad\qquad\qquad Q_{33}(s) = \frac{E^2_{\mathrm{eff}}(s)}{2\left[1 - \left(v^2_{\mathrm{eff}}(s)\right)^2\right]}, \qquad -h/2 \le z \le 0, \end{aligned} \tag{4.3}$$

where $s = 1$ for $0 \le z \le h/2$ and $s = 2$ for $-h/2 \le z \le 0$.

The resultant force and resultant moment acting on the FGM shell are

$$\{N\,, M\} = \begin{Bmatrix} N_x \\ N_\theta \\ N_{x\theta} \\ M_x \\ M_\theta \\ M_{x\theta} \end{Bmatrix} = \{\varepsilon\}[\mathbf{V}] = \begin{Bmatrix} \varepsilon_1 \\ \varepsilon_2 \\ \varepsilon_3 \\ \varepsilon_4 \\ \varepsilon_5 \\ 2\varepsilon_6 \end{Bmatrix} \begin{bmatrix} A_{11} & A_{12} & 0 & -B_{11} & -B_{12} & 0 \\ A_{12} & A_{22} & 0 & -B_{12} & -B_{22} & 0 \\ 0 & 0 & A_{33} & 0 & 0 & -B_{33} \\ B_{11} & B_{12} & 0 & -D_{11} & -D_{12} & 0 \\ B_{12} & B_{22} & 0 & -D_{12} & -D_{22} & 0 \\ 0 & 0 & B_{33} & 0 & 0 & -D_{33} \end{bmatrix}, \tag{4.4}$$

where N_x, N_θ, $N_{x\theta}$ are the in-plane resultant forces in the x, θ, and $x\theta$ directions, M_x, M_θ, $M_{x\theta}$ are the resultant bending and torsion moments in the corresponding directions; $\{\varepsilon\}$ denotes the strain vector. The coefficients A_{jk}, B_{jk}, D_{jk} $(j,k = 1,2,3)$ are global, through-thickness integrated stiffness coefficients representing extensional stiffness, extension-bending coupling stiffness, and bending stiffness, respectively. These coefficients incorporate the effects of material gradation, porosity distribution, and temperature-dependent material properties, with no simplifications adopted in the derivation.

Based on the Sanders theory, the strain energy U and kinetic energy K of the FGM shell are obtained as follows:

$$\begin{aligned} U &= \frac{1}{2} \int_0^L \int_0^{2\pi} \{\boldsymbol{\varepsilon}\}^{\mathrm{T}} [\mathbf{V}] \{\boldsymbol{\varepsilon}\} R \,\mathrm{d}x \,\mathrm{d}\theta, \\ K &= \frac{1}{2} \int_0^l \int_0^{2\pi} \rho_{\mathrm{T}} \left[\left(\frac{\partial u}{\partial t}\right)^2 + \left(\frac{\partial v}{\partial t}\right)^2 + \left(\frac{\partial w}{\partial t}\right)^2 \right] R \,\mathrm{d}x \,\mathrm{d}\theta, \end{aligned} \tag{4.5}$$

where ρ_{T} denotes the mass density per unit length, which is expressed as

$$\rho_{\mathrm{T}} = \int_0^{h/2} \rho^1_{\mathrm{eff}}(z) \,\mathrm{d}z + \int_{-h/2}^{0} \rho^2_{\mathrm{eff}}(z) \,\mathrm{d}z. \tag{4.6}$$

The elastic strain energy stored in the boundary spring of an FGM shell is given by

$$\begin{aligned} V = {} & \frac{1}{2}\int\limits_0^{2\pi}\left[k_1u^2+k_2v^2+k_3w^2+k_4\left(\frac{\partial w}{\partial x}\right)^2\right]_{x=0} R_1(0)\,\mathrm{d}\theta \\ & + \frac{1}{2}\int\limits_0^{2\pi}\left[k_1u^2+k_2v^2+k_3w^2+k_4\left(\frac{\partial w}{\partial x}\right)^2\right]_{x=L} R_2(L)\,\mathrm{d}\theta, \end{aligned} \tag{4.7}$$

where k_1, k_2, k_3, and k_4 represent the axial spring stiffness, circumferential spring stiffness, radial spring stiffness, and rotational spring stiffness, respectively.

5. Characteristic equation of an FGM conical shell

The axial, circumferential, and radial displacements of the FGM conical shell are periodic functions of the circumferential angle θ with a period of 2π, requiring simultaneous solution. Consequently, the displacement fields are expressed in the form of trigonometric functions associated with the circumferential modal number and the circumferential wave number

$$\begin{aligned} u(x,\theta,t) &= U_n(x)\cos(n\theta+\omega t), \\ v(x,\theta,t) &= V_n(x)\sin(n\theta+\omega t), \\ w(x,\theta,t) &= W_n(x)\cos(n\theta+\omega t), \end{aligned} \tag{5.1}$$

where $U_n(x)$, $V_n(x)$, and $W_n(x)$ denote the mode functions at azimuthal wave number n, and ω represents the modal frequencies. As documented in (Xu *et al.*, 2024), Chebyshev polynomials exhibit favorable convergence properties, thus permitting their expansion into different-order modes

$$\begin{aligned} U_n(x) &= \sum_{m=0}^{M} A_m T_m(x), \\ V_n(x) &= \sum_{m=0}^{M} B_m T_m(x), \\ W_n(x) &= \sum_{m=0}^{M} C_m T_m(x), \end{aligned} \tag{5.2}$$

where m denotes the axial wave number and n denotes the circumferential wave number; A, B, and C are undetermined coefficients, and M is the truncation order. $T(\cdot)$ stands for the Chebyshev polynomial, whose specific expression is

$$\begin{aligned} & T_0(x) = 1, \qquad T_1(x) = x, \\ & T_{a+1}(x) = 2x\cdot T_a(x) - T_{a-1}(x), \qquad a \geq 1, \qquad a \in \mathrm{N}^+. \end{aligned} \tag{5.3}$$

On the basis of the above energy expression, the energy model can be established as

$$\mathit{\Pi} = U_{\max} + V_{\max} - K_{\max}, \tag{5.4}$$

where subscript "max" denotes the maximum value of each energy term during one period of harmonic vibration, which is a standard treatment in the Rayleigh–Ritz method for free vibration analysis.

By virtue of the Rayleigh–Ritz method, partial differentiation with respect to the undetermined coefficients is performed to establish the vibration control equations

$$[\omega^2\mathbf{M}_1 + 2\mathbf{M}_2 - \mathbf{K}]\begin{Bmatrix} U \\ V \\ W \end{Bmatrix} = 0, \tag{5.5}$$

where $\mathbf{K}$, $\mathbf{M}_1$ and $\mathbf{M}_2$, denote the stiffness, inertial mass matrix and coupled mass matrix, respectively. U, V, and W denote the undetermined coefficient vectors, with the specific expressions given by

$$\begin{aligned} U &= \{U_0, U_1, U_2, ..., U_M\}^{\mathrm{T}}, \\ V &= \{V_0, V_1, V_2, ..., V_M\}^{\mathrm{T}}, \\ W &= \{W_0, W_1, W_2, ..., W_M\}^{\mathrm{T}}. \end{aligned} \tag{5.6}$$

6. Boundary conditions for an FGM conical shell

The boundary conditions at both ends of the conical shell are modeled by artificial springs with stiffness coefficients k_1 (axial), k_2 (circumferential), k_3 (radial), and k_4 (rotational). Conventional boundary conditions comprise free (F), clamped (C), and simply supported (S) ones. The spring stiffness values are assigned in accordance with the settings given in Table 2 (Chen *et al.*, 2023).

Table 2. Artificial spring stiffness value.

Boundary conditions	Free	Clamped	Simply supported
Spring stiffness value	$k_1 = 0$	$k_1 = 10^{14}$	$k_1 = 0$
	$k_2 = 0$	$k_2 = 10^{14}$	$k_2 = 10^{14}$
	$k_3 = 0$	$k_3 = 10^{14}$	$k_3 = 10^{14}$
	$k_4 = 0$	$k_4 = 10^{14}$	$k_4 = 0$

7. Results and discussion

To facilitate subsequent analysis, the frequency is rendered dimensionless as given in Eq. (7.1) (Wan *et al.*, 2025a):

$$\omega_1 = \omega R_2\sqrt{\rho_m(1-\nu_m^2)/E_m}, \tag{7.1}$$

where E_m, ν_m, and ρ_m are all material properties of the metal.

Unless otherwise stated, the geometric parameters of the conical shell adopted in the numerical analysis are defined as follows: $h = 0.001\,\mathrm{m}$, $R_1 = 0.2\,\mathrm{m}$, $R_2 = 1.195\,\mathrm{m}$, $L = 2\,\mathrm{m}$, $a_0 = 30°$. The volume fraction exponent $N = 1$, temperature difference $T_{cm} = 700\,\mathrm{K}$, and the axial wave number m and circumferential wave number n are both 1.

Table 3 presents the variation in modal frequencies with circumferential and axial wave numbers for a pore-free FGM shell under clamped-free boundary conditions. The results demonstrate that the modal frequencies computed from Eq. (5.5) are in close agreement with those obtained from finite element analysis (FEM), with all discrepancies lying within an acceptable range. This confirms the validity of the modal frequency equation for an FGM shell. FEM model validation is conducted using ABAQUS 2022. A converged mesh of 0.02 m is used, containing 12 000 elements and 15 600 nodes. Temperature-dependent ZrO_2-SUS304 properties are applied, and two

Table 3. Dimensionless modal frequencies of a conical shell with a C-F boundary.

(n, m)	(1,2)	(1,3)	(1,4)	(1,5)
Present	0.088	0.113	0.254	0.331
FEM	0.091	0.119	0.257	0.335
Error [%]	3.29	5.04	1.16	1.19
Modal shape	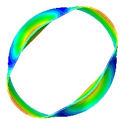	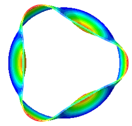	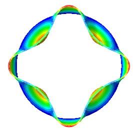	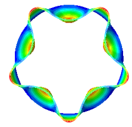
(n, m)	(1,6)	(1,7)	(1,8)	(1,9)
Present	0.453	0.512	0.622	0.735
FEM	0.460	0.524	0.635	0.741
Error [%]	1.52	2.29	2.04	0.81
Modal shape	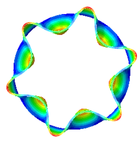	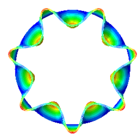	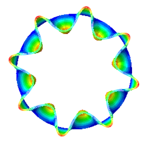	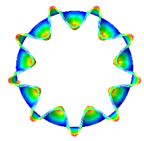

porosity distributions are simulated via the Voigt model. Clamped-clamped boundary conditions are imposed on both ends of the conical shell, matching the theoretical model.

Figure 3 shows the effect of temperature difference on the modal frequencies of an FGM shell at different porosity volume fractions. For low-order modes with $(m, n) < 3$, global bending and stretching dominate. Temperature reduces the FGM effective elastic modulus, decreasing structural stiffness and modal frequencies. For higher-order modes at $(m, n) = 3$, local deformation prevails. Geometric constraints offset temperature effects, making its influence on modal frequencies negligible. However, the influence of γ on modal frequencies increases as the vibration wave numbers (m, n) grow. When T_{cm} is constant, the modal frequencies of FGMs increase with increasing γ; when γ equals zero, the modal frequency of the pore model I conical shell equals that of the pore model II conical shell; when γ is non-zero, the modal frequency of pore model I is always greater than that of pore model II, whilst the rate of increase for pore model I modal frequencies is also higher than that for pore model II modal frequencies, mainly due to its lower effective mass density. As vibration theory indicates, frequency is inversely proportional to the square root of mass. Although model II has a slightly higher elastic modulus, the effect of mass reduction dominates, leading to higher frequencies for model I. The contribution of pore model I voids to the modal frequencies increase due to mass reduction is greater than the contribution of pore model II voids to the modal frequencies increase due to stiffness enhancement. The mass reduction does not directly increase stiffness. Model I shows a remarkable decrease in mass with a slight drop in stiffness. Model II presents a slight increase in stiffness with a minor decrease in mass.

Figure 4 illustrates the effect of temperature difference on the modal frequencies of a porous FGM shell for different volume fraction indices. The two porosity models show similar trends, although the numerical values differ. When T_{cm} is small, the influence of N on the modal frequencies is weak. As T_{cm} increases, the effect of N on modal frequencies becomes more pronounced, especially for smaller values of N. The relationship between N and modal frequencies is not strictly monotonic over the entire range examined. Among the values considered in this study, the modal frequency decreases from $N = 0$ to $N = 0.5$ and then increases as N increases from 0.5 to 10; therefore, $N = 0.5$ gives the minimum modal frequency in the present parametric study. At $N = 0$, each plane perpendicular to the thickness direction contains 50 %

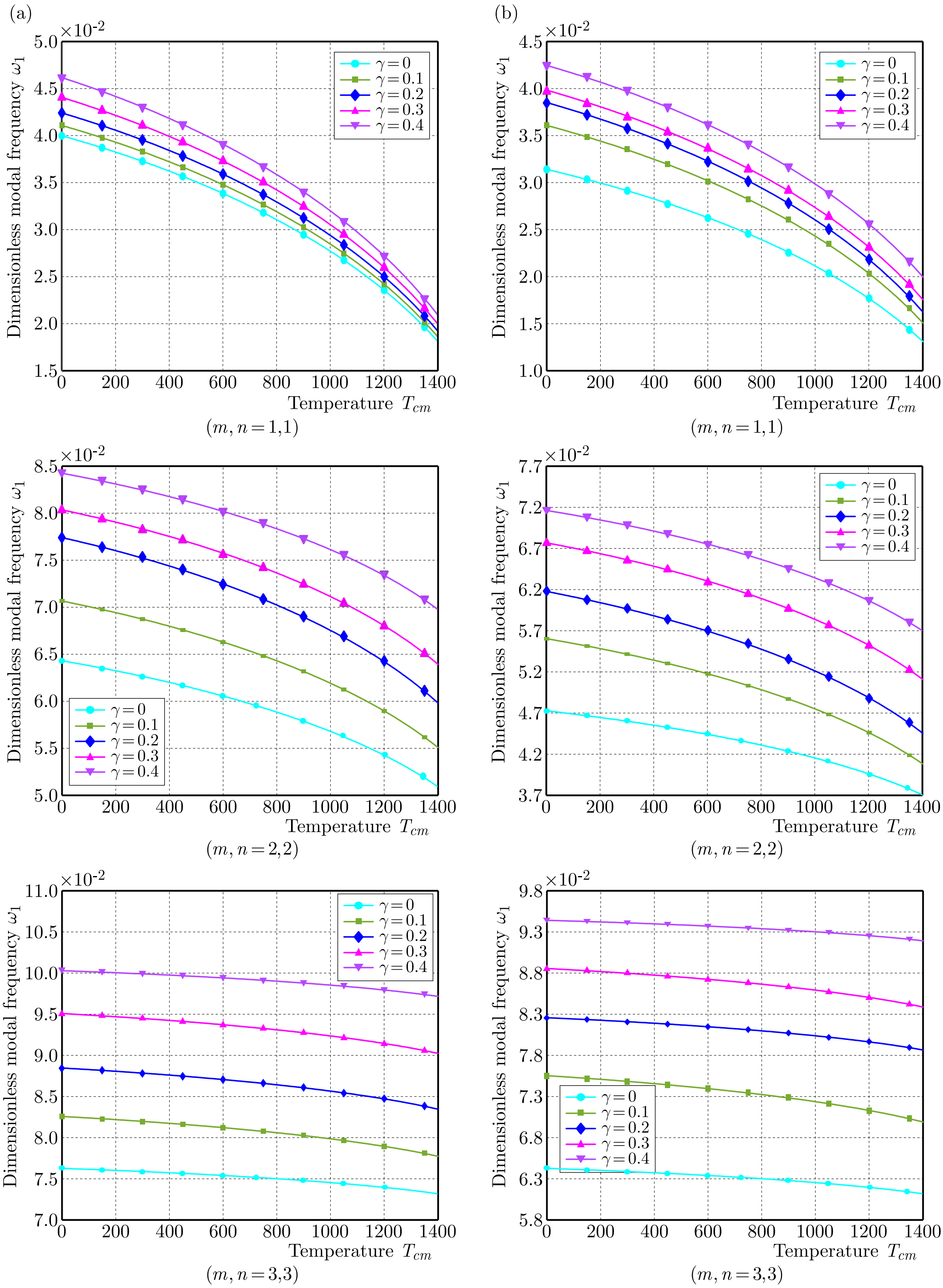

Fig. 3. Effect of temperature difference on dimensionless modal frequencies of an FGM shell at different pore volume fractions (the dimensionless definition of ω_1 is given in Eq. (7.1)): (a) even porosity; (b) uneven porosity.

metal and 50 % ceramic. As N increases beyond 0.5, the ceramic content near the inner high-temperature surface increases while the metallic content near the outer surface also increases. Because the ceramic phase has better thermal resistance than the metallic phase, increasing N

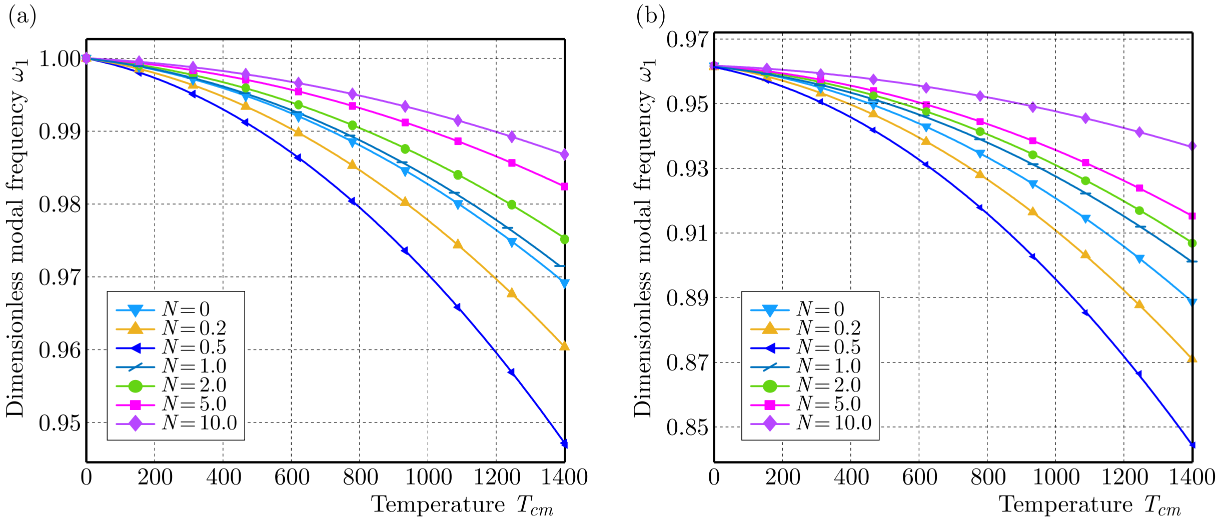

Fig. 4. Effect of temperature difference on dimensionless modal frequencies of an FGM shell at different volume fraction indexes: (a) even porosity; (b) uneven porosity.

beyond the minimum-frequencies point reduces the sensitivity of the conical shell stiffness to the temperature difference. Accordingly, an S-shaped piecewise volume-fraction distribution with an appropriately selected exponent can help reduce thermal sensitivity while retaining sufficient metallic content for structural strength.

8. Conclusion

In this paper, the free vibration equations of a porous metal-ceramic functionally graded conical shell were derived based on the Sanders thin-shell theory and the Rayleigh–Ritz method. The variation trends of modal frequencies under thermal loading were then examined. The main conclusions are summarized as follows:

1) At the same porosity volume fraction, pore model I yields a larger increase in modal frequencies than pore model II within the considered parameter range, mainly because model I produces a more significant reduction in effective mass density. Therefore, when the primary design objective is to increase modal frequencies through mass reduction, pore model I may be advantageous for the cases investigated in this study. However, in engineering practice, the selection between the two porosity distributions should also consider strength, stability, manufacturing feasibility, and other service requirements.
2) At low vibration wave numbers, the temperature difference has a more pronounced influence on the modal frequencies of an FGM shell than the porosity volume fraction, whereas at high vibration wave numbers, porosity becomes the dominant factor. For the S-shaped piecewise volume-fraction distribution considered in this study, the modal frequencies reach their minimum at $N = 0.5$ among the examined volume-fraction exponents and then increase as N increases from 0.5 to 10. Increasing the exponent beyond this minimum-frequencies point can mitigate the influence of the temperature difference on shell stiffness while maintaining metallic components that contribute to structural strength. This feature is beneficial for long-term service in variable high-temperature thermal environments with an arbitrary inner-surface temperature.
3) The present theoretical model does not include thermal stress and its coupling effect on modal frequencies. Future work will establish a thermo-mechanical coupling dynamic model to evaluate the effect of thermal stress and thereby improve prediction accuracy and applicability.

Acknowledgments

The authors are very grateful to the anonymous reviewers for their constructive comments, and gratefully acknowledge the financial support from the National Natural Science Foundation of China (grant no. 52365012) and the Natural Science Foundation of Jiangxi Province (grant no. 20224ACB204015).

References

1. Asemi, K., & Jedari Salami, S. (2015). A study on low velocity impact response of FGM rectangular plates with 3D elasticity based graded finite element modeling. *Journal of Theoretical and Applied Mechanics*, *53*(4), 859–872. https://doi.org/10.15632/jtam-pl.53.4.859
2. Chen, Y.G., Wang, Q.S., Zhong, R., Shi, X.J., & Qin, B. (2023). Fiber orientation and boundary stiffness optimization of laminated cylindrical shells with elastic boundary for maximum the fundamental frequency by an improved sparrow search algorithm. *Thin-Walled Structures*, *193*, Article 111299. https://doi.org/10.1016/j.tws.2023.111299
3. Chi, S.-H., & Chung, Y.-L. (2006). Mechanical behavior of functionally graded material plates under transverse load–Part I: Analysis. *International Journal of Solids and Structures*, *43*(13), 3657–3674. https://doi.org/10.1016/j.ijsolstr.2005.04.011
4. Chumanov, I.V., Anikeev, A.N., & Chumanov, V.I. (2015). Fabrication of functionally graded materials by introducing wolframium carbide dispersed particles during centrifugal casting and examination of FGM's structure. *Procedia Engineering*, *129*, 816–820. https://doi.org/10.1016/j.proeng.2015.12.111
5. Ding, S.H., & Li, X. (2008). An anti-plane shear crack in bonded functionally graded piezoelectric materials under electromechanical loading. *Computational Materials Science*, *43*(2), 337–344. https://doi.org/10.1016/j.commatsci.2007.11.009
6. Feng, J.B., & Hu, Y.D. (2026). Three-dimensional magneto-thermoelastic coupling resonance of spinning functionally graded cylindrical shells with porosity. *Thin-Walled Structures*, *219*(Part A), Article 114175. https://doi.org/10.1016/j.tws.2025.114175
7. Huang, X.-L., & Shen, H.-S. (2004). Nonlinear vibration and dynamic response of functionally graded plates in thermal environments. *International Journal of Solids and Structures*, *41*(9–10), 2403–2427. https://doi.org/10.1016/j.ijsolstr.2003.11.012
8. Kalali, A.T., Hassani, B., & Hadidi-Moud, S. (2016). Elastic-plastic analysis of pressure vessels and rotating disks made of functionally graded materials using the isogeometric approach. *Journal of Theoretical and Applied Mechanics*, *54*(1), 113–125. https://doi.org/10.15632/jtam-pl.54.1.113
9. Kołakowski, Z., & Teter, A. (2016). Some aspects of dynamic coupled response of functionally graded thin-walled columns with square cross-sections under in-plane pulse compression. *Journal of Theoretical and Applied Mechanics*, *54*(2), 449–462. https://doi.org/10.15632/jtam-pl.54.2.449
10. Li, H.C., Pang, F.Z., Ren, Y., Miao, X.H., & Ye, K.F. (2019). Free vibration characteristics of functionally graded porous spherical shell with general boundary conditions by using first-order shear deformation theory. *Thin-Walled Structures*, *144*, Article 106331. https://doi.org/10.1016/j.tws.2019.106331
11. Liu, W.G., Shu, B., Guo, L.Q., & He, H.L. (2017). Impacts of thermal environment on modal frequency of FGM shells (in Chinese). *Journal of Vibration and Shock*, *36*(4), 127–131. https://doi.org/10.13465/j.cnki.jvs.2017.04.020
12. Loy, C.T., & Lam, K.Y. (1997). Vibration of cylindrical shells with ring support. *International Journal of Mechanical Sciences*, *39*(4), 455–471. https://doi.org/10.1016/S0020-7403(96)00035-5
13. Mallek, H., Mellouli, H., Ben Said, L., Wali, M., Dammak, F., & Alhadri, M. (2025). Porosity effects on nonlinear static performances of functionally graded shells considering thickness stretching. *Facta Universitatis*, *Series: Mechanical Engineering*, *23*(4), 827–860. https://doi.org/10.22190/FUME240920015M

14. Matsunaga, H. (2009). Free vibration and stability of functionally graded circular cylindrical shells according to a 2D higher-order deformation theory. *Composite Structures*, *88*(4), 519–531. https://doi.org/10.1016/j.compstruct.2008.05.019

15. Pillai, A.U., & Rahaman, M.M. (2026). A novel phase-field model for fatigue failure in functionally graded materials under thermo-mechanical loading. *Composite Structures*, *379*, Article 120003. https://doi.org/10.1016/j.compstruct.2025.120003

16. Reddy, J.N. (2000). Analysis of functionally graded plates. *International Journal for Numerical Methods in Engineering*, *47*(1–3), 663–684. https://doi.org/10.1002/(SICI)1097-0207(20000110/30)47:1/3<663::AID-NME787>3.0.CO;2-8

17. Shen, H.-S. (2012). Nonlinear vibration of shear deformable FGM cylindrical shells surrounded by an elastic medium. *Composite Structures*, *94*(3), 1144–1154. https://doi.org/10.1016/j.compstruct.2011.11.012

18. Wan, R.H., Liu, W.G., Chen, L., & Pang, L. (2025a). Analysis of traveling wave vibration of GNPs-reinforced bi-directional functionally graded rotating joined cylindrical-conical-cylindrical shells. *Acta Mechanica*, *236*(5), 3035–3053. https://doi.org/10.1007/s00707-025-04309-6

19. Wan, R.H., Liu, W.G., Cheng, L., & Pang, L. (2025b). Traveling wave vibration analysis of rotating reinforced functionally graded conical shells. *Journal of Mechanical Science and Technology*, *39*(5), 2417–2429. https://doi.org/10.1007/s12206-025-0402-3

20. Wang, Y.Q., Ye, C., & Zu, J.W. (2018). Identifying the temperature effect on the vibrations of functionally graded cylindrical shells with porosities. *Applied Mathematics and Mechanics*, *39*(11), 1587–1604. https://doi.org/10.1007/s10483-018-2388-6

21. Wang, Y.W., & Wu, D.F. (2017). Free vibration of functionally graded porous cylindrical shell using a sinusoidal shear deformation theory. *Aerospace Science and Technology*, *66*, 83–91. https://doi.org/10.1016/j.ast.2017.03.003

22. Wu, L. (2004). Thermal buckling of a simply supported moderately thick rectangular FGM plate. *Composite Structures*, *64*(2), 211–218. https://doi.org/10.1016/j.compstruct.2003.08.004

23. Xu, H.D., Wang, Y., Xu, Z.Q., & Yu, X.G. (2024). Gegenbauer-Ritz method for free vibration analysis of rotating functionally graded graphene reinforced porous composite stepped cylindrical shells with arbitrary boundary conditions. *Engineering Structures*, *303*, Article 117555. https://doi.org/10.1016/j.engstruct.2024.117555

24. Xue, Y.Q., Jin, G.Y., Zhang, C.Y., Han, X.H., & Chen, J. (2023). Free vibration analysis of functionally graded porous cylindrical panels and shells with porosity distributions along the thickness and length directions. *Thin-Walled Structures*, *184*, Article 110448. https://doi.org/10.1016/j.tws.2022.110448

Manuscript received December 29, 2025; accepted for publication July 16, 2026; published online August 17, 2026.

JOURNAL OF THEORETICAL
AND APPLIED MECHANICS
64, 3, pp. 257–273, Warsaw 2026
https://doi.org/10.15632/jtam-pl/226326

FATIGUE DAMAGE PROCESS INVESTIGATION OF 18NI300 STEEL SPECIMENS MANUFACTURED BY LPBF METHOD

Roland PAWLICZEK, Cyprian SKÓRA*

Opole University of Technology, Faculty of Mechanical Engineering, Opole, Poland
*corresponding author, *c.skora@student.po.edu.pl*

The fatigue response of additively manufactured maraging steel MS1 produced by laser powder bed fusion (LPBF) was experimentally investigated. Uniaxial tension-compression fatigue tests were conducted at cycle asymmetry ratios $R = -1$, -0.5, and 0 to assess the influence of mean stress on fatigue life. The results demonstrated a pronounced effect of the stress ratio on fatigue performance. Two-step loading sequences – low-high (Lo-Hi) and high-low (Hi-Lo) – were applied to examine damage accumulation under non-constant loading conditions. A load asymmetry sensitivity factor was determined and the applicability of classical fatigue damage models was evaluated.

Keywords: maraging steel 18Ni300; additive manufacturing; fatigue life; stress ratio R.

1. Introduction

The additive manufacturing (AM) is a process based on the successive joining layer-by-layer of the material without the need for additional tooling or machining operations. Among AM techniques, selective laser melting (SLM) is one of the most widely used methods for metallic materials. In SLM, metal powder is selectively melted by a high-power laser according to CAD-generated cross sections, enabling the production of complex geometries with applications in aerospace, automotive, medical and defense industries (Croccolo *et al.*, 2018). Compared with conventional subtractive manufacturing, AM shortens supply chains, reduces material waste and allows greater design flexibility. However, the process is also associated with high energy consumption and challenges in controlling material properties and dimensional tolerances (Frazier, 2014; Afkhami *et al.*, 2019). Current literature on AM materials mainly focuses on the influence of process parameters, build orientation and post-processing treatments on mechanical properties (Croccolo *et al.*, 2018).

In industrial applications, maraging steel 300 (18Ni300, MS1) has attracted considerable attention due to its high strength, good ductility, weldability, and excellent fatigue resistance. MS1 is a low-carbon Fe-Ni martensitic steel strengthened by precipitation hardening. Owing to its very low carbon content, the alloy exhibits good machinability and weldability making it suitable for AM technologies and tooling, aerospace, marine, military, and automotive engineering applications. Despite its promising properties, the fatigue behaviour of additively manufactured MS1 steel still requires further investigation (Raju & Rosen, 2021; Cyr *et al.*, 2018; Solberg *et al.*, 2021).

A number of studies on 18Ni300 have demonstrated that the fatigue performance of AM maraging steel strongly depends on post-processing and manufacturing conditions. Cyr *et al.* (2018) showed significant anisotropy of mechanical properties caused by build orientation, while Rigon *et al.* (2018) reported that specimens built at 0° exhibited fatigue strengths that were 45 % to 60 % higher than those oriented at 90°. Similar anisotropic behaviour and lower fatigue strength compared with conventionally manufactured materials were observed by Damon *et al.* (2019). In contrast, Meneghetti *et al.* (2017) found no significant influence of orientation on tensile properties or fatigue behaviour in both as-built and aged conditions. Solberg *et al.* (2021) demonstrated that specimens fabricated closer to vertical orientation achieved longer fatigue life than horizontally oriented built samples. Similar work by Cerezo *et al.* (2024) showed that build orientation and defect morphology significantly affected crack propagation behaviour, with larger pores promoting faster crack growth.

Other studies also emphasized the importance of post-processing operations. Croccolo *et al.* (2018) reported that machining combined with heat treatment significantly improved fatigue strength, whereas heat treatment alone had little effect. Raju and Rosen (2021) similarly observed that aging treatment improved fatigue life, although machining produced the greatest enhancements. Yang *et al.* (2026) reported that solution-aging treatment improved mechanical properties through precipitation strengthening and microstructural refinement, while dos Santos Silva *et al.* (2026) demonstrated a substantial increase in tensile strength after heat treatment, accompanied by reduced ductility. Zhao *et al.* (2024) compared additively manufactured and cast material of 18Ni300 maraging steel and observed superior strength and plasticity of AM specimens due to their refined microstructure. The influence of processing parameters was also highlighted by Jose and Mishra (2026), who observed improved fatigue life for specimens produced using a stripe scanning strategy and further enhancements after heat treatment.

Investigations by Branco *et al.* (2021) and Karolczuk *et al.* (2024) indicated that surface and subsurface defects, particularly unmelted regions generated during the AM process, play a dominant role in crack initiation and fatigue damage. Under variable-amplitude loading, Marciniak *et al.* (2024) observed cyclic softening and identified surface and near-surface defects as the primary crack initiation sites. Investigation by Macek *et al.* (2024) linked fatigue life to fracture-surface topography and demonstrated that incorporating roughness parameters improved fatigue-life predictions. Karolczuk and Kurek (2025) reported that mean stress and surface topography play a significant role in fatigue damage accumulation and life prediction.

Just as research into the influence of the structure of additively manufactured materials on their strength is important, understanding the material response under various loading conditions is equally important. It is crucial for industries utilizing these modern manufacturing techniques to obtain information on the validation of the methods and algorithms used to design structural components with regard to additively manufactured materials. Do damage accumulation processes in such materials follow the mechanisms known from conventionally manufactured materials?

Although numerous investigations have addressed the effects of build orientation, heat treatment, manufacturing parameters and defect characteristics on the fatigue behaviour of LPBF-manufactured 18Ni300 maraging steel, the available literature remains focused primarily on constant-amplitude fatigue under a single stress ratio ($R = -1$). To the best of the authors' knowledge, systematic S-N characteristics covering different cycle asymmetry ratios for the as-built state of specimens are not available. Moreover, studies investigating the combined influence of the mean stress, cycle asymmetry and variable-amplitude block loading on the fatigue behaviour of LPBF-manufactured 18Ni300 are scarce. In particular, experimental verification of fatigue damage accumulation under low-high (Lo-Hi) and high-low (Hi-Lo) loading sequences, together with the evaluation of mean stress sensitivity and the applicability of commonly used mean stress correction models, has not yet been comprehensively reported for the examined material.

Therefore, the present study provides a comprehensive experimental investigation of the fatigue behaviour of LPBF-manufactured 18Ni300 maraging steel under different cycle asymmetry ratios ($R = -1$, -0.5, and 0). Firstly, preliminary constant-amplitude fatigue tests were performed to establish complete S-N characteristics for each loading condition. Based on these results, the material sensitivity factor to cycle asymmetry was determined and the applicability of the Smith–Watson–Topper (SWT) mean stress correction model was evaluated. Furthermore, two-stage Lo-Hi and Hi-Lo block-loading experiments were carried out to investigate fatigue damage accumulation under variable-amplitude loading. The analysis was complemented by tensile tests and hysteresis loop measurements, providing additional insight into the cycle deformation behaviour of the material. The obtained results provide an experimental dataset that is currently unavailable or insufficient in the literature for the fatigue behaviour of LPBF-manufactured 18Ni300 maraging steel in the as-built condition under different cycle asymmetry ratios and block-loading sequences. The study contributes to a better understanding of mean stress effects and fatigue damage accumulation.

2. Mean stress and calculation models

Programmed fatigue tests enable the reproduction of service loading conditions of structures and devices under laboratory conditions by applying selected cyclic loads. Loading histories may include variable amplitudes and mean stress values defined by the cycle asymmetry ratio R. Mean stress is an important factor affecting fatigue behaviour. It influences the maximum permissible stress amplitude. In engineering structures, mean stress often results from self-weight or operational tasks such as material transport and therefore should be considered in fatigue analyses (Pawliczek, 2005; Chiou & Yip, 2003). To evaluate fatigue life of 18Ni300 under different stress ratios, Solberg *et al.* (2021) investigated the influence of build orientation on the fatigue performance on LPBF-manufactured 18Ni300 maraging steel, fabricated in ten different orientations (from 0° to 135° in 15° increments). Specimens were aged at 500 °C for 5 h before removal from the build platform. All specimen surfaces were machined except for one surface that remained in the as-built condition. The authors performed fatigue tests under a stress ratio of $R = 0$ at a loading frequency of 30 Hz using a constant stress level of approximately 500 MPa, corresponding to a fatigue life of approximately $1 \cdot 10^5$ cycles. To enable comparison with fatigue data reported in the literature under fully reversed loading ($R = -1$), the authors applied the SWT mean stress correction model, which is as follows:

$$\sigma_{ar} = \sigma_{\max}\sqrt{\frac{1-R}{2}}, \tag{2.1}$$

where σ_{ar} is the stress amplitude at $R = -1$, and $\sigma_{\max}$ is the maximum stress during the load cycle at the given value of R.

The corrected fatigue data showed good agreement with the available results obtained under $R = -1$, thus confirming the applicability of the SWT approach for comparing fatigue performance under different stress ratios.

An important aspect of fatigue analysis is the assessment of the influence of the load sequence and stress level on damage accumulation. A commonly used approach is block-loading, usually divided into two stages with significantly different stress amplitudes. In two-step loading tests, referred to as Lo-Hi and Hi-Lo sequences, the material is first subjected to either low or high stress amplitudes and then loaded at the opposite level in the second stage. The first block is typically specified by the number of cycles n_1 at stress amplitude σ_1, while the second block is applied at stress amplitude σ_2 until failure. The presence of mean stress during such tests strongly affects damage accumulation and may lead to significant differences in fatigue life between applied sequences. Among available cumulative damage models, the Palmgren–Miner linear damage rule (LDR) was adopted due to its extensive use in fatigue engineering and its role as a reference model for evaluating sequence effects under variable loading conditions. Its application enables direct comparison between the experimentally observed damage accumulation and the predictions based on linear summation of fatigue damage. The linear damage rule is expressed as

$$D = \sum_{i=1}^{n} \frac{n_i}{N_i}, \tag{2.2}$$

where D is the degree of damage, n_i is the number of applied cycles at a given stress amplitude, N_i is the number of cycles to failure at the same stress amplitude.

According to this model, the total damage under ideal conditions should equal 1. However, under two-step loading, Lo-Hi sequences generally produce damage values greater than 1, whereas the Hi-Lo loading path results in damage values below 1 (Pawliczek, 2014; 2018).

In the present study, the classical, historically oldest model is used to generate the basic S-N curves (Murakami *et al.*, 2021). This model was employed by the same research group to describe MS1 material in studies (Croccolo *et al.*, 2018). Fatigue curves can be expressed using logarithmic or power functions, as in Eq. (2.3) or Eq. (2.4). The stress amplitude is determined as follows:

$$\log(N) = b + a \cdot \log(\sigma), \tag{2.3}$$

$$\sigma = 10^{b/a} \cdot N^{1/a}, \tag{2.4}$$

where N denotes the number of cycles, a and b are the equation parameters, and σ is the stress amplitude.

3. Material

Specimens for fatigue tests were manufactured using EOS MS1 maraging steel powder (European 1.2709), in accordance with the geometry shown in Fig. 1 and in compliance with the recommendations of the standard ASTM International (2021). The specimens were produced by the laser powder bed fusion (LPBF) process using the EOS M280 system in a nitrogen atmosphere. The specimens were built along the Z-axis on a platform preheated to 40 °C. Default process parameters for LPBF, supplied by EOS, were applied: laser beam power 285 W, scan speed 960 mm/s, layer thickness 40 µm and scan rotation 67°. The manufactured specimens were cleaned by micro-blasting using glass beads with a diameter of 90 µm to 150 µm at a low flow pressure of 300 kPa (Blast 2 Softline K1 device, FerroECOBlast) without any further machining. Figure 2 presents the tensile test curves obtained for two specimens. The force–elongation (F–ΔL) curve is linear, and after reaching the maximum value of load, there is a large increase in deformation with decreasing load. This indicates that the material has high elasticity. Mechanical parameters of 18Ni300 maraging steel are contained in Table 1. For the maximum force, the registered elongation was 0.588 mm. The axial stiffness of specimen is $k \approx 206$ kN/mm. Vickers hardness measurements yielded a mean value of 371 ±5 HV5. The measured hardness of the specimens is consistent with the range reported for additively manufactured 18Ni300 maraging steel in the as-built condition. The scatter of the results confirms good material homogeneity.

(a) (b)

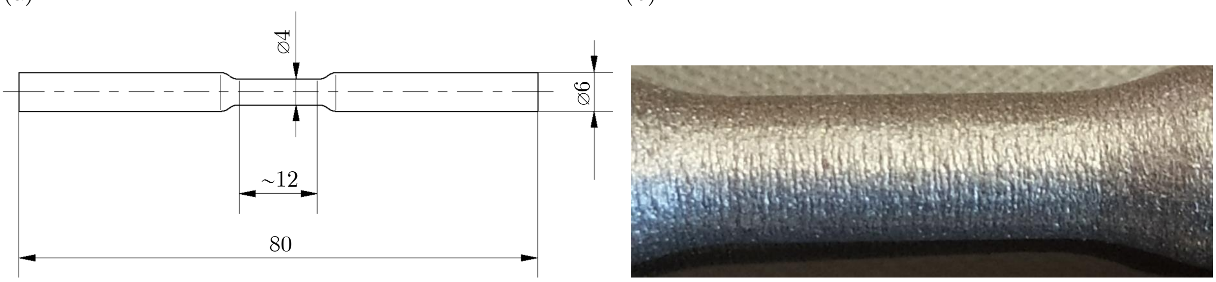

Fig. 1. (a) Specimen geometry; (b) view of the fusion line of successive layers.

In (Karolczuk *et al.*, 2024), fatigue tests were carried out using specimens produced from the same powder and manufactured using the same LPBF process. To determine the actual

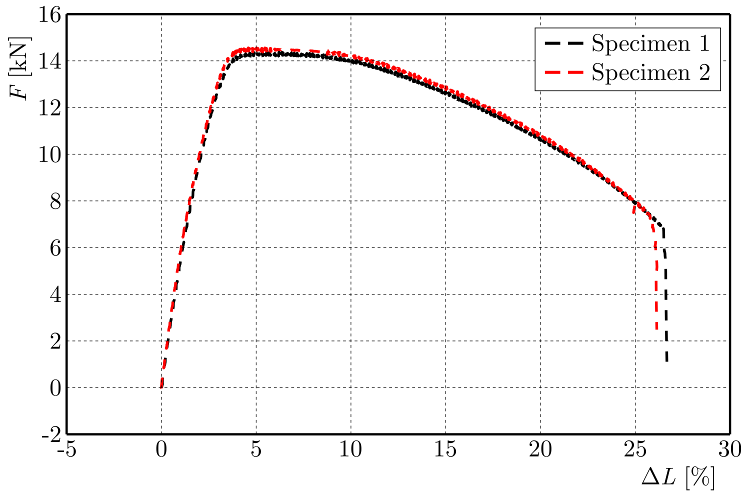

Fig. 2. Tensile test chart of MS1 material.

Table 1. Mechanical parameters of MS1.

Maximum force F_m [kN]	Young's modulus E [GPa]	Yield strength R_{p02} [MPa]	Ultimate strength R_m [MPa]	Elongation at fracture [%]
14.403	168	656.55	1205.70	26.67

chemical composition of the investigated material, the elemental contents were measured using an optical emission spectrometer (S3 MiniLab 300) on specimens aged at 490 °C. The reported values represent the mean of six measurements together with the corresponding 95 % confidence intervals and are presented in Table 2 alongside the nominal chemical composition provided by the powder supplier. The same study also includes images of the powder morphology and particle size distribution.

Table 2. Chemical composition of MS1 (wt.%) based on data reported by Karolczuk *et al.* (2024), according to information provided by supplier and from the measurements using an optical emission spectrometer.

	Ni	Mo	Co	Ti	Al	Cr	Si	Mn	C	Fe
Supplier	17–19	4.5–5.2	8.5–9.5	0.6–0.8	0.05–0.15	0–0.5	0–0.1	0–0.1	0–0.03	Balance
Spectrometer	17.6 ±0.2	5.4 ±0.0	8.7 ±0.2	0.6 ±0.0	0.07 ±0.01	0.05 ±0.02	0.09 ±0.01	0.2 ±0.0	0.01 ±0.0	Balance

The surface topography of the as-built specimens was characterized using a surface profilometer Alicona InfiniteFocus G4. After scanning the sample surface, the software generated a graph of the sample's topography and a roughness profile over a 4.5 mm measurement section. The program then divided the profile into 5 segments, each 0.8 µm long, where for each segment the distance between the maximum peak and the deepest valley was determined, and finally the arithmetic mean of these five segment measurements was calculated as the R_z parameter and arithmetic mean roughness R_a parameter, defined as the arithmetic mean deviation of the roughness profile from the mean value of the measurement section. The measured parameters were 19.21 µm and 3.40 µm, respectively. Representative surface topography and the corresponding roughness profile are presented in Fig. 3 and Fig. 4. The results confirm the relatively rough surface typical of LPBF-manufactured specimens in the as-built condition, which may promote stress concentration and facilitate fatigue crack initiation.

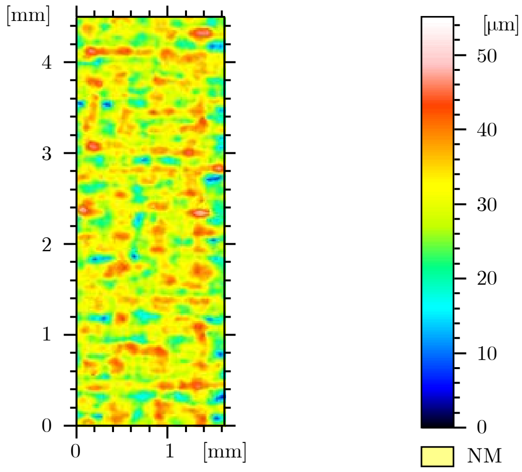

Fig. 3. Surface topography of the as-built specimen.

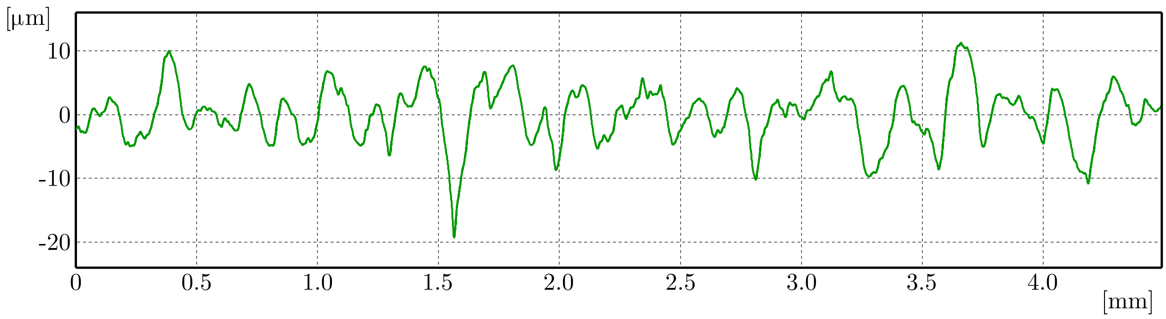

Fig. 4. Roughness profile (S-L) of as-built specimen of 18Ni300 maraging steel.

4. Methodology

For fatigue tests on specimens shown in Fig. 1, an Instron Electropuls E10000 testing system with a maximum load capacity of 10 kN was used, equipped with dedicated control software. Uniaxial tension-compression tests controlled by force/load at a frequency of ∼5 Hz were performed under sinusoidal loading with constant amplitude for the cycle asymmetry ratio $R = -1$, and under sinusoidal loading with constant amplitude including mean load values for $R = -0.5$ and $R = 0$. The load (force) during the test was applied as parallel to the build direction of samples. With changes in the R ratio according to Eqs. (4.1) and (4.2), the contribution of mean stress is as follows: $\sigma_m = 0$ for $R = -1$; $\sigma_m = 1/3\sigma_a$ for $R = -0.5$; $\sigma_m = \sigma_a$ for $R = 0$:

$$R = \frac{\sigma_{\min}}{\sigma_{\max}}, \tag{4.1}$$

$$\sigma_a = \frac{\sigma_{\max} - \sigma_{\min}}{2}, \qquad \sigma_m = \frac{\sigma_{\max} + \sigma_{\min}}{2}, \tag{4.2}$$

where $\sigma_{\max}$ is the maximum stress amplitude and $\sigma_{\min}$ is the minimal stress amplitude.

For low-cycle fatigue (LCF) tests, the selected ranges of stress amplitude σ_a for $R = -1$ were between 600 MPa and 1000 MPa. With an increase in the cycle asymmetry ratio to $R = -0.5$, the maximum stress range $\sigma_{\max}$ was 588 MPa to 718 MPa. For $R = 0$, $\sigma_{\max}$ was 538 MPa to 718 MPa. It should be noted that the maximum stresses described in this paper are defined as nominal values and are used solely to describe the loads. Results of the preliminary fatigue tests on LPBF-manufactured samples of 18Ni300 maraging steel, designed to determine S-N curves, are presented in Table 3.

Table 3. Results of the preliminary fatigue tests for different cycle asymmetry ratios.

Cycle asymmetry ratio	σ_a [MPa]	σ_m [MPa]	$\sigma_{\max}$ [MPa]	$N_{\exp}$ [cycle]
$R = -1$	600	–	600	18235
	650	–	650	10424
	675	–	675	9134
	700	–	700	5499
	800	–	800	4367
	900	–	900	2156
	1000	–	1000	376
$R = -0.5$	539	180	718	13324
	441	147	588	22041
	490	163	653	15271
	539	180	718	11291
	441	147	588	39187
	490	163	653	21139
$R = 0$	326	326	654	48592
	302	302	604	49197
	359	359	718	29060
	269	269	538	68442
	359	359	718	28012

Two-step block fatigue tests were also carried out using the Instron Electropuls E10000 testing system. The block loading tension-compression tests were force/load controlled at a frequency of ~5 Hz. The load ranges were selected based on the results of fatigue tests and the S-N curve equations shown in Fig. 7. Using the obtained equations, theoretical numbers of cycles to failure N were determined for specific stress amplitude values σ_a. Tests consisted of selecting appropriate loads for Hi-Lo and Lo-Hi experiments so that, in the first block (Hi- or Lo-), the specimen was subjected to tension-compression for a specified number of cycles, ranging from 20 % to 60 % of the theoretical fatigue life N_1 for the given stress amplitude σ_{a1}, with corresponding mean stress σ_{m1}. After completing the required number of cycles under the first block load, the stress amplitude and mean stress values were changed to those of the second block (σ_{a2}, σ_{m2}) corresponding to -Hi or -Lo. The tests were concluded when the specimen fractured or when the stiffness of the system was lost. Figure 5 presents the loading paths used in the experiments for different cycle asymmetry ratios. The approach for sequence tests is schematically presented in Fig. 6.

$R = -1$
Low block
$\sigma_a = 600$ [MPa]
$N = 14122$ [cycle]
High block
$\sigma_a = 675$ [MPa]
$N = 7640$ [cycle]

$R = -0.5$
Low block
$\sigma_a = 490$ [MPa]
$\sigma_m = 163$ [MPa]
$N = 18362$ [cycle]
High block
$\sigma_a = 539$ [MPa]
$\sigma_m = 179$ [MPa]
$N = 12118$ [cycle]

$R = 0$
Low block
$\sigma_a = 359$ [MPa]
$\sigma_m = 359$ [MPa]
$N = 30199$ [cycle]
High block
$\sigma_a = 384$ [MPa]
$\sigma_m = 384$ [MPa]
$N = 24785$ [cycle]

Fig. 5. Loading path for two-stage block sequences.

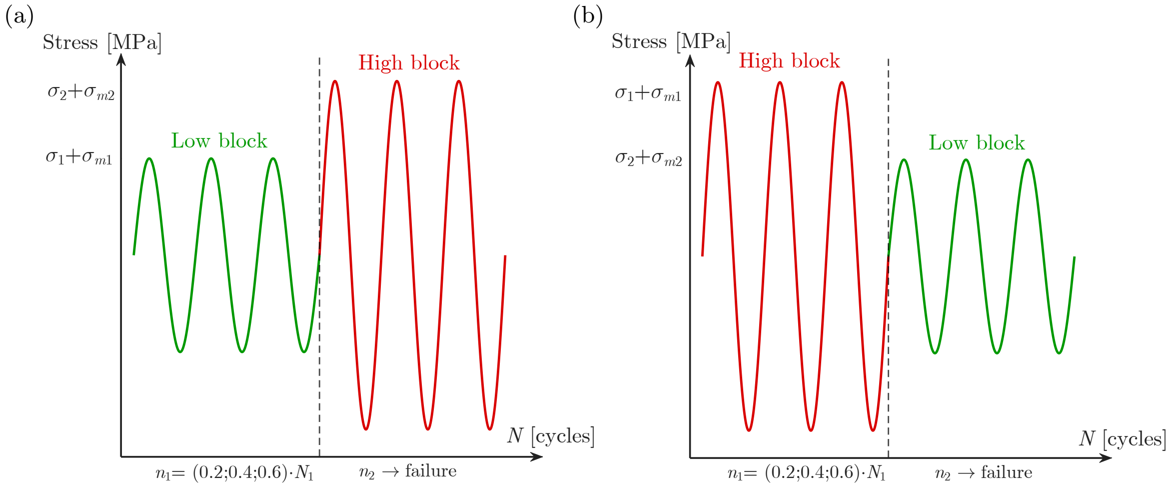

Fig. 6. Experimental campaign: (a) Lo-Hi sequence; (b) Hi-Lo sequence.

5. Fatigue characteristics

From the uniaxial tensile fatigue tests conducted in the LCF regime, the fatigue lives obtained for loads without mean stress are generally consistent with the experimental results reported in (Raju & Rosen, 2021; Rigon *et al.*, 2018; Branco *et al.*, 2021; Meneghetti *et al.*, 2019). For fatigue tests carried out under mean stress conditions, the results reported in the literature typically concern specimens tested at a cycle asymmetry ratio of $R = 0$. Additionally, the specimens used in these studies were subjected to further treatments, such as heat treatment in the form of aging at 490 °C (Solberg *et al.*, 2021; Frazier, 2014). On the other hand, fatigue tests for $R = -0.5$ are uncommon. Therefore, in both cases $R = 0$ and $R = -0.5$, for untreated material, there is no direct point of reference.

S-N curves and equations for different cycle asymmetry ratios in LCF are shown in Fig. 7. As can be observed, at higher stress amplitudes, the fatigue lives for $R = -1$ and $R = -0.5$ are similar, while for $R = 0$, the values are only slightly higher. As the stress amplitude decreases for $R = -1$, the number of cycles to failure also decreases, achieving the longest fatigue lives at the lowest amplitudes compared to the other curves. For $R = -0.5$, the number of cycles increases as the amplitude decreases, but to a lesser extent than for $R = -1$. The greatest differences occur

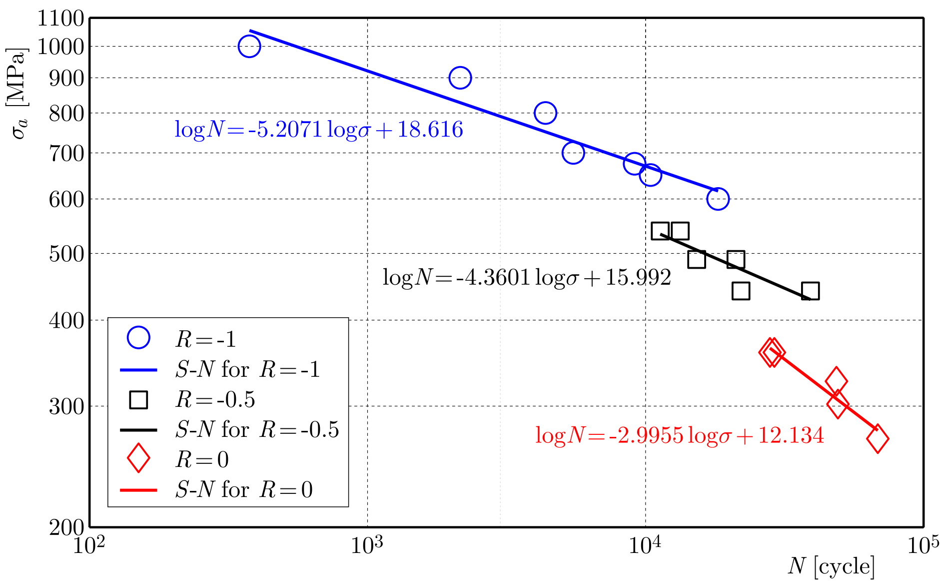

Fig. 7. S-N curves for additively manufactured MS1 maraging steel.

at $R = 0$. Up to about 800 Mpa to 900 MPa amplitude, the fatigue lives obtained at $R = 0$ are higher than those for $R = -0.5$ and $R = -1$. When the amplitude drops below this range, fatigue lives for $R = -1$ become higher than for $R = 0$, while those for $R = -0.5$ remain lower. Only at a stress amplitude of ∼600 MPa, the fatigue lives for $R = 0$ become lower than for $R = -0.5$. At the lowest stress amplitude, the fatigue lives for $R = 0$ are the smallest compared to the other two. In general, fatigue life increased with decreasing maximum stress amplitude. Among all tested conditions the lowest fatigue lives were recorded for fully reversed loading ($R = -1$). Introducing a positive mean stress component for $R = -0.5$, where $\sigma_m = \frac{1}{3}\sigma_a$, resulted in longer fatigue lives despite comparable stress amplitudes. The highest fatigue resistance was obtained for $R = 0$, indicating a strong influence of the stress ratio and mean stress on the fatigue performance of the material.

The hysteresis loops were determined on the actuator displacement recorded by the Instron Electropuls 10000 testing machine. From the hysteresis loops (Fig. 8) in the stress–displacement system, it should be noted that they are narrow, suggesting minor plastic deformations in the tested material or even an elastic state of deformations. It is also worth noting that at a large number of cycles (towards the end of fatigue life), a slight shift of the loop towards strain is observed, which may suggest the occurrence of creep phenomena. This effect is most evident in tests conducted at $R = 0$, and is caused by the presence of significant mean stress. In contrast, for tests without mean stress, the hysteresis loops for the three selected measurement points exhibited almost identical shapes, with only slight differences in the initial portions.

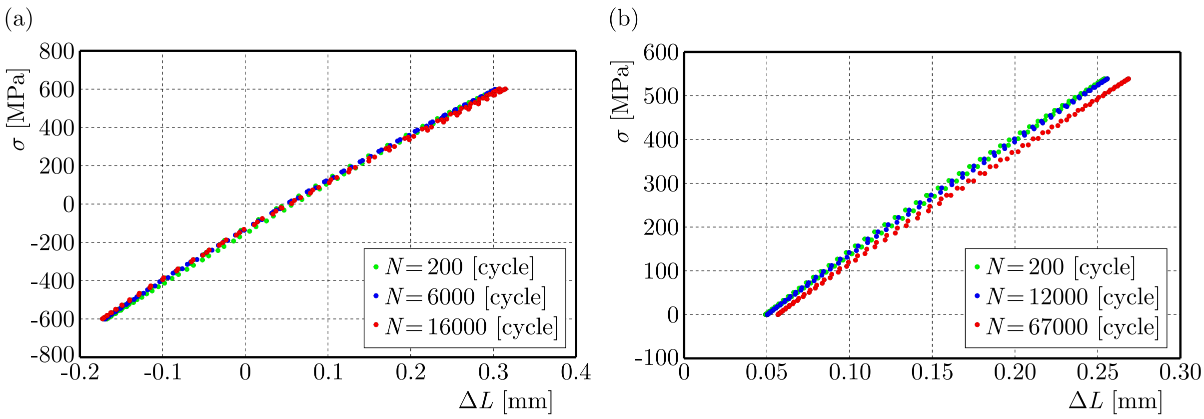

Fig. 8. Hysteresis loops: (a) $R = -1$, $\sigma_a = 600$ MPa; (b) $R = 0$, $\sigma_a = 269$ MPa.

6. Stress ratio factor approach

Gasiak and Pawliczek (2003) proposed a model for determining the material sensitivity factor to cycle asymmetry ψ, as a function of the number of cycles to failure, based on experimental fatigue test results. The proposed model is based on the Haigh diagram and on a simplified linear relationship between the stress amplitude σ_a and the mean stress σ_m. For the limiting amplitudes of stresses, the following expression is adopted:

$$\Delta\sigma = \Delta\sigma_{-1} - 2\psi_\sigma\sigma_m, \tag{6.1}$$

$$\psi_\sigma(N) = \frac{2\Delta\sigma_{-1}(N) - \sigma_0(N)}{\sigma_0(N)}, \tag{6.2}$$

where $\psi_\sigma(N)$ is the material sensitivity factor to cycle asymmetry for a given number of cycles to failure, $\Delta\sigma_{-1}(N)$ is the stress amplitude under cyclic bending/tension at the number of cycles to failure, $\sigma_0(N)$ is the maximum stress under pulsating cycles in bending/tension for a given number of cycles to failure.

To evaluate the effect of cycle asymmetry on changes in the S-N characteristics for different cycle asymmetry ratios (as presented in Fig. 7), three fatigue life ranges of $2 \cdot 10^4$, $4 \cdot 10^4$, $6 \cdot 10^4$ cycles to failure were selected. Using equations of S-N curves determined from experimental results, stress amplitude values were determined for these fatigue ranges. Figure 9 presents the results, together with equations of the curves for the given stress ratios. The calculated theoretical fatigue points largely overlap with the linear regression curves, and the equations of the curves shown in Fig. 9 are nearly identical to those presented in Fig. 7.

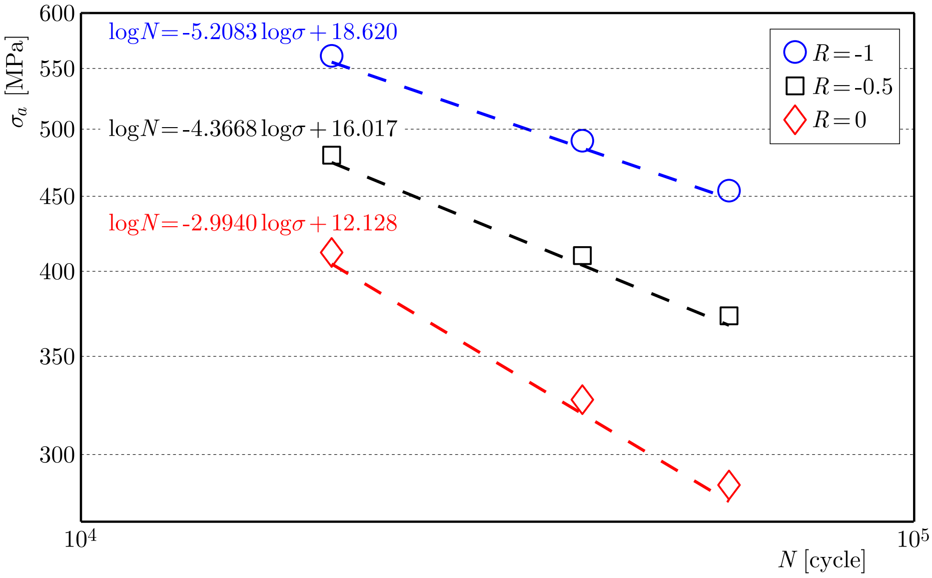

Fig. 9. Fatigue life N versus estimated stress amplitude for the assumed fatigue lives.

Figure 10 shows the relationship between the normalized mean stress (σ_m/R_m) and the normalized stress amplitude (σ_a/σ_{AT}), where σ_{AT} is a substitute amplitude value calculated based on the applied model, using previously determined points presented in Fig. 9. A comparison of the points corresponding to different values of the cycle asymmetry ratio R indicates that the SWT parameter (Eq. (2.1)) predicts slightly lower values of amplitudes compared to the

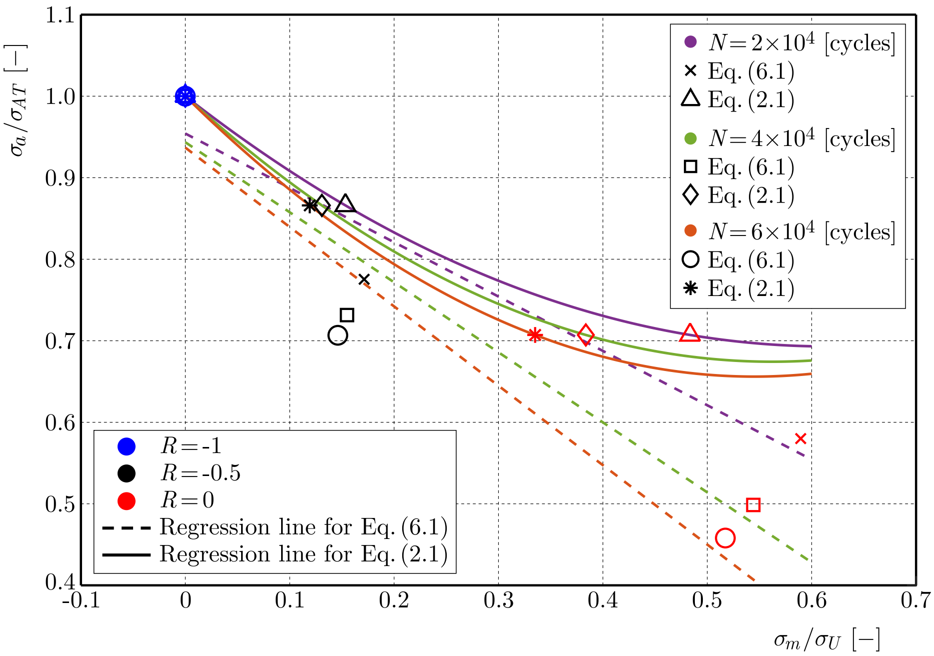

Fig. 10. Normalized Haigh diagram.

material sensitivity factor to cycle asymmetry ψ approach (Eq. (6.1)). The SWT parameter shows good correlation with the regression curves. Equation (6.1) is a linear model, and for cycle asymmetry ratios $R = -0.5$ and $R = -1$ shows weak correlation with the regression line. The best correlation is observed for the highest values of maximal stress amplitudes for $R = 0$. The differences between the SWT parameter (Eq. (2.1)) and the material sensitivity factor ψ (Eq. (6.1)) decrease with the contribution of mean stress amplitude.

Table 4 summarizes the comparison between the experimental values of the sensitivity factor to cycle asymmetry and those calculated using Eq. (6.2). As can be seen, the obtained values are very similar, especially for fatigue lives of $4 \cdot 10^4$ and $6 \cdot 10^4$. The most noticeable difference occurs at the smallest adopted number of cycles to failure, where the difference is about 3.5 %. However, this is still negligible, and therefore the formula used to determine the sensitivity factor to cycle asymmetry can be considered suitable for the investigated material.

Table 4. Comparison of experimental and calculated values of the material sensitivity factor.

N [cycles]	ψ_{exp}	ψ_{cal} (Eq. (6.2))	Relative error [%]
$2 \cdot 10^4$	0.350	0.362	3.43
$4 \cdot 10^4$	0.500	0.503	0.60
$6 \cdot 10^4$	0.590	0.592	0.34

7. Fatigue test results analysis

The fatigue test results of two-stage loading tests are presented in Fig. 11 to Fig. 13, where the lower part of the bar is equivalent to the first sequence with the given number of cycles and the upper bar is the second sequence of the test, which lasted until failure occurred. For the cycle asymmetry ratio $R = -1$, the predicted fatigue lives according to the S-N curve are $1.4 \cdot 10^4$ cycles for 600 MPa and $7.6 \cdot 10^3$ cycles for 675 MPa. In Lo-Hi tests, the second block n_2 for $n_1/N_1 = 20\,\%$ and $60\,\%$ were similar, reaching about 1.1 to $1.2 \cdot 10^4$ cycles. The greatest

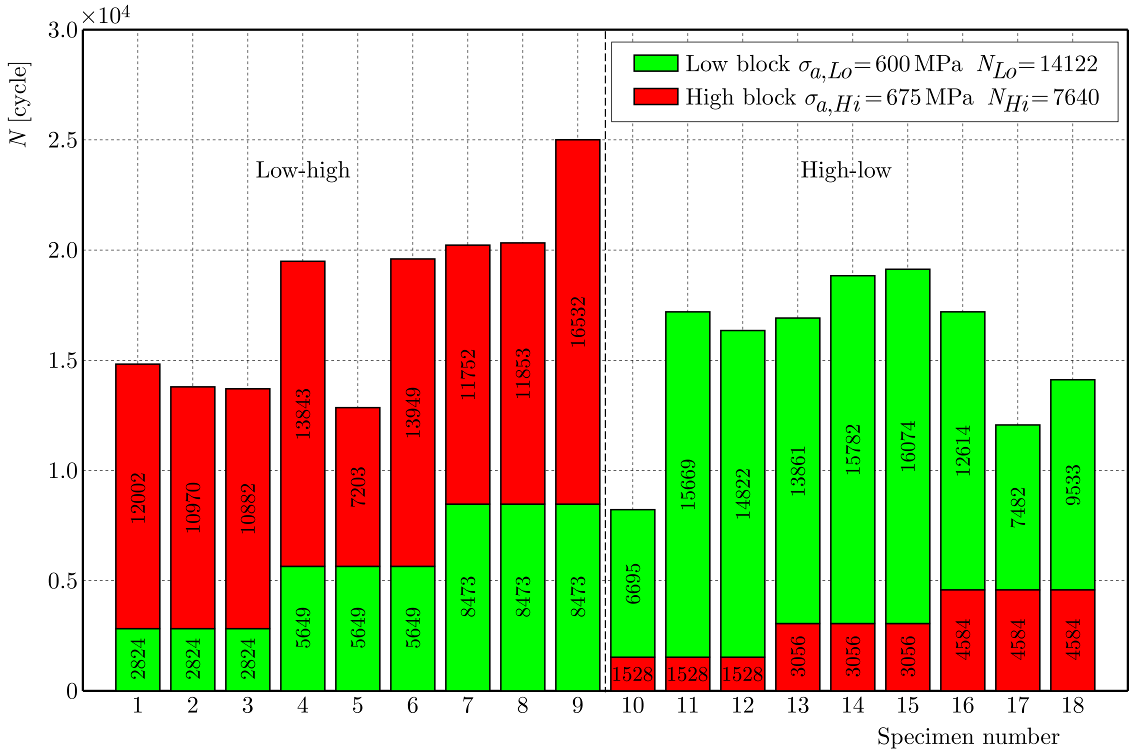

Fig. 11. Results of two-step fatigue tests for $R = -1$.

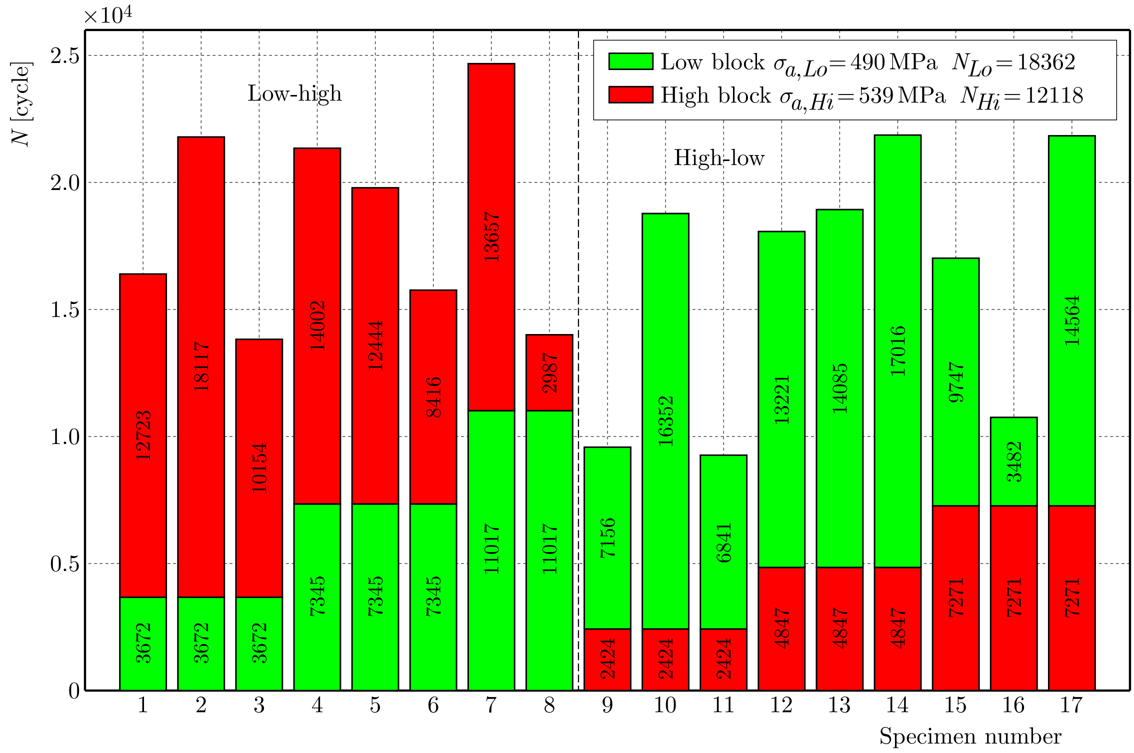

Fig. 12. Results of two-step fatigue tests for $R = -0.5$.

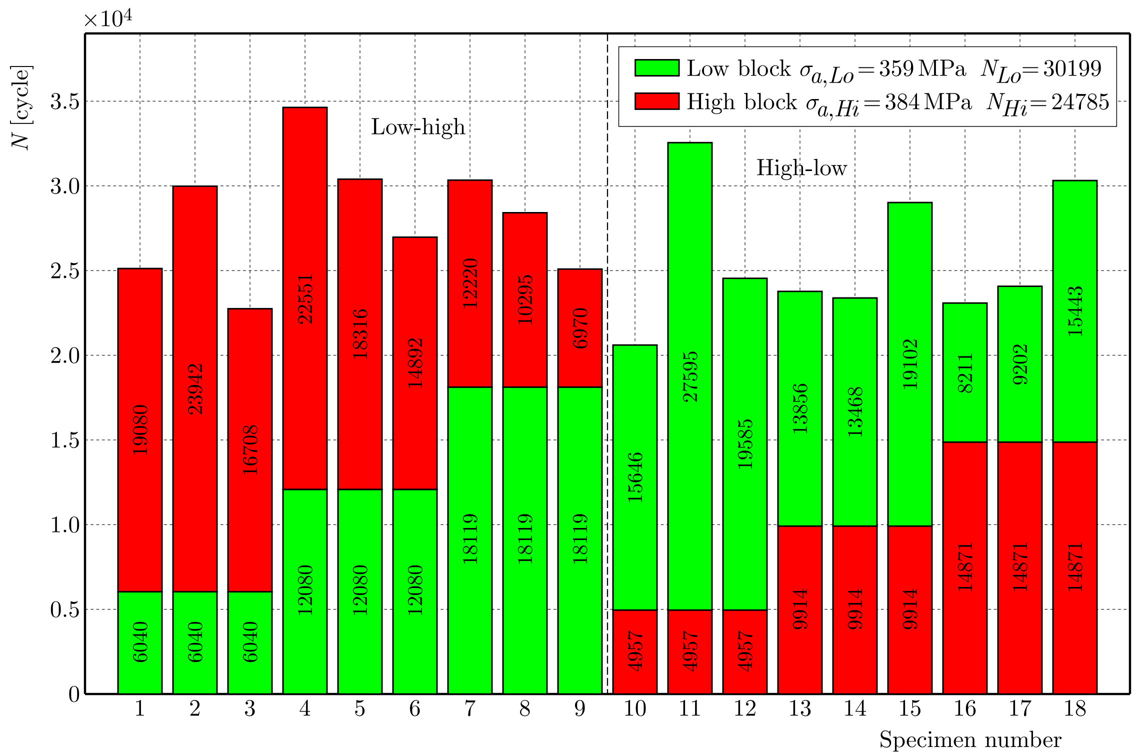

Fig. 13. Results of two-step fatigue tests for $R = 0$.

scatter of results occurred for $n_1/N_1 = 40\,\%$, where the lowest fatigue lives were recorded in this series. All specimens failed during tests. Therefore, the presented number of cycles corresponds to fatigue life at fracture. The figures directly represent the distribution of fracture lives for Lo-Hi and Hi-Lo loading sequences.

For the Hi-Lo loading path at $R = -1$, the highest fatigue lives were observed for $n_1/N_1 = 40\,\%$ while the lowest occurred for $60\,\%$. Considerable scatter between specimens was noted especially for the lowest and highest first-block shares. Mean results indicated a gradual decrease in fatigue life with increasing participation of the high-stress first block.

At the cycle asymmetry ratio $R = -0.5$ the applied maximum stresses were 653 MPa for the low sequence and 718 MPa for the high sequence with the contribution of mean stress of $\sigma_m = \frac{1}{3}\sigma_a$. Estimated fatigue lives from the corresponding equation from Fig. 7 are $1.8 \cdot 10^4$ cycles and $1.2 \cdot 10^4$ cycles. In this series of tests, substantial scatter was observed, particularly for every share of the first block. In some cases, the contribution of the second block differed by up to 4 times. The most consistent behaviour was observed for the 40 % share of the first block for Hi-Lo series, while the remaining loading paths exhibited larger variations in fatigue life.

The highest values of maximum stress amplitudes were applied during the final series for the cycle asymmetry ratio $R = 0$. Based on the S–N curve, the predicted maximum stress amplitude was 718 MPa for the low-sequence loading block and 767 MPa for the high-sequence loading block, corresponding to fatigue lives of 30 199 and 24 785 cycles, respectively. In the Lo-Hi tests, the highest fatigue life was obtained for the $n_1/N_1 = 40\,\%$, reaching approximately $3.46 \cdot 10^4$ cycles. The lowest scatter was observed for the intermediate loading ratio. In the Lo-Hi tests, the greatest durability of all experiments was observed when the first loading sequence accounted for $n_1/N_1 = 40\,\%$, with fatigue lives reaching up to $3.5 \cdot 10^4$ cycles. However, increasing the share of the first loading block resulted in lower repeatability and greater scatter. Overall, the results indicate that both the cycle asymmetry ratio R and the sequence of loading blocks significantly influence the fatigue response of additively manufactured samples of MS1 maraging steel. Considerable scatter in fatigue life, particularly under variable-amplitude loading, also confirms the strong sensitivity of the material to loading history and internal defects characteristic of the AM process.

Representative fracture surfaces obtained after the two-step block loading tests are presented in Fig. 14 and Fig. 15. Regardless of the loading sequence and the share of the first block, fatigue crack initiation was most frequently associated with manufacturing-related defects of the LPBF process. The dominant initiation sites were located either at the specimen surface or in the near-surface region, where stress concentration effects are the highest. The fractographic observations revealed several characteristic features: crack initiation region (1), rapid fracture regions (2), spherical gas pores (3), fatigue crack propagation zones with visible striations (4), lack-of-fusion (LoF) defects (5), and surface irregularities associated with the specimen contour (6). The presence of pores and LoF defects confirms that internal discontinuities remain

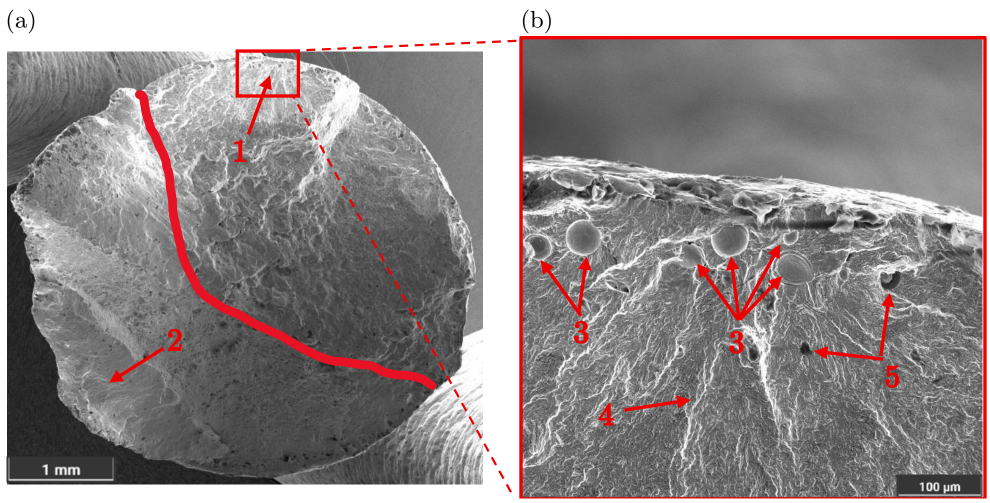

Fig. 14. Surface of the fracture in the specimen for Lo-Hi block tests, $R = -0.5$; $n_1/N_1 = 0.2$, at magnifications: (a) 100×; (b) 1000×.

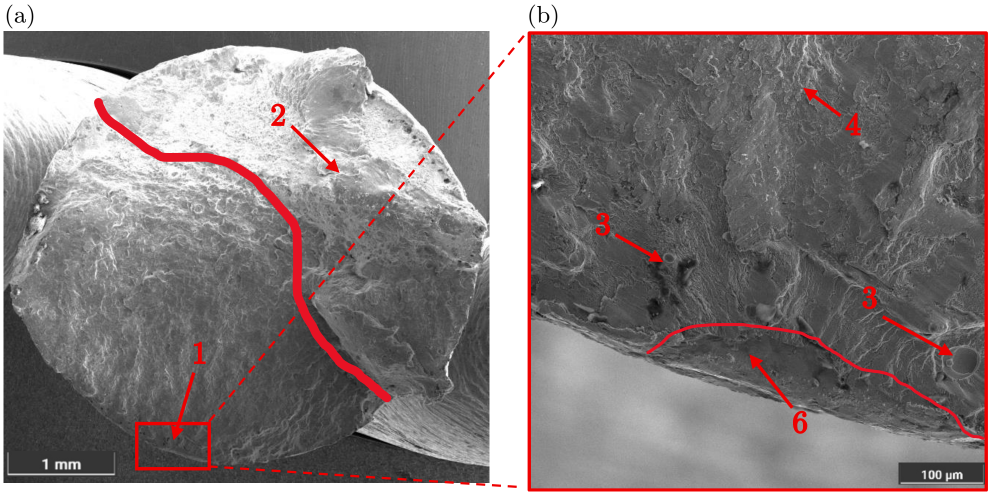

Fig. 15. Surface of the fracture in the specimen for Hi-Lo block tests, $R = -1$; $n_1/N_1 = 0.4$, at magnifications: (a) 100×; (b) 1000×.

the primary fatigue-critical features controlling crack nucleation in additively manufactured specimens.

8. Damage accumulation

Table 5 shows the mean damage accumulation results for the conducted fatigue tests. From the experimental results for the stress ratio $R = -1$, it can be observed that with an increasing

Table 5. Mean damage accumulation results for $R = -1$, $R = -0.5$, and $R = 0$.

Test	n_1/N_1	n_2/N_2	$D = n_1/N_1 + n_2/N_2$
$R = -1$			
Lo-Hi-20 %	0.20	1.107	1.307
Lo-Hi-40 %	0.40	0.787	1.187
Lo-Hi-60 %	0.60	0.642	1.242
Hi-Lo-20 %	0.20	0.770	0.970
Hi-Lo-40 %	0.40	0.863	1.263
Hi-Lo-60 %	0.60	0.375	0.975
$R = -0.5$			
Lo-Hi-20 %	0.20	1.128	1.328
Lo-Hi-40 %	0.40	0.959	1.359
Lo-Hi-60 %	0.60	0.687	1.287
Hi-Lo-20 %	0.20	0.551	0.751
Hi-Lo-40 %	0.40	0.805	1.205
Hi-Lo-60 %	0.60	0.505	1.105
$R = 0$			
Lo-Hi-20 %	0.20	0.803	1.003
Lo-Hi-40 %	0.40	0.750	1.150
Lo-Hi-60 %	0.60	0.397	0.997
Hi-Lo-20 %	0.20	0.693	0.893
Hi-Lo-40 %	0.40	0.512	0.912
Hi-Lo-60 %	0.60	0.363	0.963

share of the first block, the contribution of the second block to total damage decreases. An exception occurred in the Hi-Lo test with the first block at the 40 % of the predicted cycles to failure.

For the stress ratio $R = -0.5$, differences were also observed for both Lo-Hi and Hi-Lo sequences. In both cases, the contribution of the second block to total damage generally decreased with an increasing share of the first block. In the Lo-Hi test with a 60 % share of the first block, the smallest second-block contribution was observed in the series. Compared to the 20 % share, the damage value at 60 % was almost 65 % smaller, and compared to 40 %, it was 39 % smaller. Conversely, for the Hi-Lo sequence at the 40 % first-block share, the second-block damage contribution was the highest in the series: 32 % higher than at 20 %, and 37 % more than at 60 %.

For the stress ratio R = 0, the Lo-Hi tests showed similar second-block contributions for the 20 % and 40 % shares (difference <7 %). In contrast, the 60 % share was twice as small as second-block damage compared to the other two. For the Hi-Lo sequence, the contribution of the second block at the 20 % share was almost twice as high as observed for the 60 % share and 26 % higher compared with the 40 % share.

9. Conclusions

Fatigue testing is a crucial element in assessing performance potential of materials. The use of varied test methods, such as block loading, makes it possible to study material behaviour under variable loading conditions. Applying different stress ratios further expands the knowledge of possible applications of such materials under service conditions involving fluctuating loads and additional influencing factors. From the uniaxial tension-compression fatigue tests with different stress ratios and block sequences (Lo-Hi and Hi-Lo) on additively manufactured MS1 material, the following conclusions can be drawn:

– with a varying stress ratio and comparable stress amplitudes, the highest fatigue lives were observed for specimens tested with the mean stress present ($R = 0$), while the lowest fatigue lives were recorded for $R = -1$;
– with an increasing stress ratio, the stress amplitude values for $R = -0.5$ and $R = 0$ were lower than for $R = -1$; however, the maximum stress, which also includes mean stress, resulted in overall higher loading for $R = -0.5$ and $R = 0$ than for $R = -1$;
– S-N curves obtained for different stress ratios showed interesting behaviour, especially for $R = 0$, at lower amplitudes, fatigue life was higher than for the other ratios, while at maximum amplitudes the opposite was true, with the shortest lives observed;
– the material sensitivity factor to the stress ratio changed linearly with cycles to failure. The model effectively captured this behaviour;
– the second-block damage ratio n_2/N_2 generally decreased with increasing the first-block share n_1/N_1, with some exceptions;
– the Palmgren–Miner model fit best to sequential tests at $R = -1$. For Lo-Hi, the damage accumulation results matched the model assumptions, while for Hi-Lo at some test results the accumulation matched the Lo-Hi case. For the other Hi-Lo tests, the results aligned with the LDR model. At $R = -0.5$, deviations were observed at $n_1/N_1 = 0.4$, Hi-Lo showed higher accumulation compared to unity and at $R = 0$, Lo-Hi showed lower damage accumulation in comparison with other cycle asymmetry ratios;
– the greatest differences in damage accumulation were observed in the mean results: at $R = 0$ for Lo-Hi tests with $n_1/N_1 = 20\,\%$ and 60 %, less damage was generated, while for $R = -0.5$ in Hi-Lo tests with $n_1/N_1 = 40\,\%$ and 60 %, more damage was accumulated, in contradiction to the Palmgren–Miner model assumptions.

References

1. Afkhami, S., Dabiri, M., Alavi, S.H., Björk, T., & Salminen, A. (2019). Fatigue characteristics of steels manufactured by selective laser melting. *International Journal of Fatigue*, *122*, 72–83. https://doi.org/10.1016/j.ijfatigue.2018.12.029
2. ASTM International. (2021). *E466-21, Standard Practice for Conducting Force Controlled Constant Amplitude Axial Fatigue Tests of Metallic Materials*. ASTM International. https://doi.org/10.1520/E0466-21
3. Branco, R., Costa, J.D., Martins Ferreira, J.A., Capela, C., Antunes, F.V., & Macek, W. (2021). Multiaxial fatigue behaviour of maraging steel produced by selective laser melting. *Materials & Design, 201*, Article 109469. https://doi.org/10.1016/j.matdes.2021.109469
4. Cerezo, P.M., Cruces, A.S., Moore, S., Wheatley, G., & Lopez-Crespo, P. (2024). Characterisation of 18Ni300 steel CT specimens in a fatigue test manufactured by selective laser melting at 0°, 45° and 90°. *Theoretical and Applied Fracture Mechanics*, *134*(Part B), Article 104730. https://doi.org/10.1016/j.tafmec.2024.104730
5. Croccolo, D., De Agostinis, M., Fini, S., Olmi, G., Robusto, F., Ćirić Kostić, S., Vranić, A., & Bogojević, N. (2018). Fatigue response of as-built DMLS maraging steel and effects of aging, machining, and peening treatments. *Metals*, *8*(7), Article 505. https://doi.org/10.3390/met8070505
6. Cyr, E., Lloyd, A., & Mohammadi, M. (2018). Tension-compression asymmetry of additively manufactured maraging steel. *Journal of Manufacturing Processes*, *35*, 289–294. https://doi.org/10.1016/j.jmapro.2018.08.015
7. Damon, J., Hanemann, T., Dietrich, S., Graf, G., Lang, K.-H., & Schulze, V. (2019). Orientation dependent fatigue performance and mechanisms of selective laser melted maraging steel X3NiCoMoTi18-9-5. *International Journal of Fatigue*, *127*, 395–402. https://doi.org/10.1016/j.ijfatigue.2019.06.025
8. dos Santos Silva, B.C., Seixas, L.F., Callegari, B., Batalha, R.L., Reis, L., dos Santos Paula, A., Godefroid, L.B., Batalha, G.F., & Coelho, R.S. (2026). Influence of build orientation and thermal treatment on the fracture toughness of LPBF-manufactured 18Ni300 maraging steel. *Journal of Materials Research and Technology*, *40*, 577–592. https://doi.org/10.1016/j.jmrt.2025.12.134
9. Frazier, W.E. (2014). Metal additive manufacturing: A review. *Journal of Materials Engineering and Performance*, *23*(6), 1917–1928. https://doi.org/10.1007/s11665-014-0958-z
10. Gasiak, G., & Pawliczek, R. (2003). Application of an energy model for fatigue life prediction of construction steels under bending, torsion and synchronous bending and torsion. *International Journal of Fatigue*, *25*(12), 1339–1346. https://doi.org/10.1016/S0142-1123(03)00055-0
11. Jose, S.S.S., & Mishra, S.K. (2026). Effect of scanning strategies on low cycle fatigue and corrosion behaviour of LPBF 18Ni300 steel. *Materials Chemistry and Physics*, *362*, Article 132761. https://doi.org/10.1016/j.matchemphys.2026.132761
12. Karolczuk, A., & Kurek, A. (2025). Machine learning insight into the mean stress impact on fatigue life of additively manufactured 18Ni300 maraging steel under various multiaxial stress paths. *International Journal of Fatigue*, *198*, Article 109023. https://doi.org/10.1016/j.ijfatigue.2025.109023
13. Karolczuk, A., Kurek, A., Böhm, M., Derda, S., Prażmowski, M., Kluger, K., Żak, K., Pejkowski, Ł., & Seyda, J. (2024). Heterogeneous effect of aging temperature on the fatigue life of additively manufactured thin-walled 18Ni300 maraging steel tubular specimen. *Materials & Design*, *237*, Article 112561. https://doi.org/10.1016/j.matdes.2023.112561
14. Macek, W., Marciniak, Z., Lesiuk, G., Podulka, P., & Jiang, C.-P. (2024). The Smith–Watson–Topper parameter and fracture surface topography relationship for additively manufactured 18Ni300 steel subjected to uniaxial variable-amplitude loading. *Theoretical and Applied Fracture Mechanics*, *133*(Part B), Article 104607. https://doi.org/10.1016/j.tafmec.2024.104607
15. Marciniak, Z., Branco, R., Macek, W., Dobrzyński, M., & Malça, C. (2024). Cyclic deformation and fracture behaviour of additive manufactured maraging steel under variable-amplitude loading. *Theoretical and Applied Fracture Mechanics*, *129*, Article 104207. https://doi.org/10.1016/j.tafmec.2023.104207

16. Meneghetti, G., Rigon, D., Cozzi, D., Waldhauser, W., & Dabalà, M. (2017). Influence of build orientation on static and axial fatigue properties of maraging steel specimens produced by additive manufacturing. *Procedia Structural Integrity*, *7*, 149–157. https://doi.org/10.1016/j.prostr.2017.11.072

17. Meneghetti, G., Rigon, D., & Gennari, C. (2019). An analysis of defects influence on axial fatigue strength of maraging steel specimens produced by additive manufacturing. *International Journal of Fatigue*, *118*, 54–64. https://doi.org/10.1016/j.ijfatigue.2018.08.034

18. Murakami, Y., Takagi, T., Wada, K., & Matsunaga, H. (2021). Essential structure of *S-N* curve: Prediction of fatigue life and fatigue limit of defective materials and nature of scatter. *International Journal of Fatigue*, *146*, Article 106138. https://doi.org/10.1016/j.ijfatigue.2020.106138

19. Pawliczek, R. (2005). Fatigue life of specimens made of 18G2A steel under bending block loading for given values of mean load (in Polish). *Zeszyty Naukowe / Politechnika Opolska*, *83*, 167-174.

20. Pawliczek, R. (2014). Influence of the mean load value in fatigue block loading on strains. *Key Engineering Materials*, *598*, 195–200. https://doi.org/10.4028/www.scientific.net/KEM.598.195

21. Pawliczek, R. (2018). Evaluation of fatigue damage degree for specimens made of S355J0 steel subjected to bending block loads with mean load value. In D. Skibicki (Ed.), *Fatigue Failure and Fracture Mechanics XXVII: Proceedings of the XXVII Polish National Conference on Fatigue Failure and Fracture Mechanics*, *2028*(1), Article 020015. https://doi.org/10.1063/1.5066405

22. Raju, N., & Rosen, D.W. (2021). Fatigue properties of 3D printed maraging steel. In *Proceedings of the 32nd Annual International Solid Freeform Fabrication Symposium – An Additive Manufacturing Conference*, 831–841.

23. Rigon, D., Meneghetti, G., Görtler, M., Cozzi, D., Waldhauser, W., & Dabalà, M. (2018). Influence of defects on axial fatigue strength of maraging steel specimens produced by additive manufacturing. *MATEC Web of Conferences*, *165*, Article 02005. https://doi.org/10.1051/matecconf/201816502005

24. Solberg, K., Hovig, E.W., Sørby, K., & Berto, F. (2021). Directional fatigue behaviour of maraging steel grade 300 produced by laser powder bed fusion. *International Journal of Fatigue*, *149*, Article 106229. https://doi.org/10.1016/j.ijfatigue.2021.106229

25. Yang, T., Zeng, H., Liu, Z., Chen, P., Yang, C., Qiu, C., & Chu, P.K. (2026). Synergistic improvement of strength and elongation in laser-melting-deposited 18Ni300/316 heterostructured dual-phase steel by heat treatment. *Smart Materials in Manufacturing*, *4*, Article 100124. https://doi.org/10.1016/j.smmf.2026.100124

26. Zhao, M., Shen, S., Wang, H., Niu, L., Shi, J., Chen, Z., Wang, X., & Lu, B. (2024). Effect of heat treatment on microstructure and hydrogen embrittlement of additively manufactured and cast 18Ni300 maraging steel. *Journal of Materials Research and Technology*, *33*, 9566–9579. https://doi.org/10.1016/j.jmrt.2024.12.002

Manuscript received May 20, 2026; accepted for publication July 23, 2026; published online September 7, 2026.

Contents